

**SEARCH FOR HEAVY PHOTONS WITH DETACHED
VERTICES IN THE 2015 ENGINEERING RUN OF THE
HEAVY PHOTON SEARCH EXPERIMENT**

by

Holly Szumila-Vance
B.S. May 2008, Embry-Riddle Aeronautical University
B.S. May 2009, Embry-Riddle Aeronautical University
M.S. May 2014, Old Dominion University

A Dissertation Submitted to the Faculty of
Old Dominion University in Partial Fulfillment of the
Requirements for the Degree of

DOCTOR OF PHILOSOPHY

PHYSICS

OLD DOMINION UNIVERSITY
June 2017

Approved by:

Lawrence Weinstein (Director)

John Adam (Member)

Wally Van Orden (Member)

Stepan Stepanyan (Member)

Lepsha Vuskovic (Member)

ABSTRACT

SEARCH FOR HEAVY PHOTONS WITH DETACHED VERTICES IN THE 2015 ENGINEERING RUN OF THE HEAVY PHOTON SEARCH EXPERIMENT

Holly Szumila-Vance
Old Dominion University, 2017
Director: Dr. Lawrence Weinstein

text of abstract goes here

Copyright, 2017, by Holly Szumila-Vance, All Rights Reserved.

ACKNOWLEDGMENTS

TABLE OF CONTENTS

	Page
LIST OF TABLES	viii
LIST OF FIGURES	ix
Chapter	
1. INTRODUCTION	1
2. MOTIVATION	3
2.1 THEORY OF HEAVY PHOTONS	3
2.2 SIGNATURE	3
2.3 HEAVY PHOTONS AND DARK MATTER	3
2.4 EXISTING LIMITS ON HEAVY PHOTONS	3
3. HOW TO SEARCH FOR A HEAVY PHOTON	4
3.1 BUMP HUNT	4
3.2 DETACHED VERTEX SIGNAL	4
3.3 TRIDENT BACKGROUND	4
3.3.1 BEITHE-HEITLER	4
3.3.2 RADIATIVE	4
3.4 WIDE ANGLE BREMSSTRAHLUNG	4
3.5 BEAM HALO	4
3.6 HIGH Z BACKGROUND??	4
4. HEAVY PHOTON SEARCH EXPERIMENT	5
4.1 CEBAF	5
4.2 BEAMLINE	6
4.2.1 TARGET	13
4.2.2 COLLIMATOR	14
4.3 SILICON VERTEX TRACKER	14
4.4 ELECTROMAGNETIC CALORIMETER	16
4.4.1 LIGHT MONITORING SYSTEM	18
4.4.2 AVALANCHE PHOTODIODES	21
4.5 TRIGGER	24
5. DETECTOR CALIBRATION AND PERFORMANCE	28
5.1 SILICON VERTEX TRACKER PERFORMANCE	28
5.1.1 MØLLER MASS	28
5.2 ELECTROMAGNETIC CALORIMETER CALIBRATION	28
5.2.1 SIMULATIONS	28
Energy reconstruction	29

Energy resolution	33
Position reconstruction	34
Position resolution	37
5.2.2 ECAL CALIBRATION USING COSMIC RAY ENERGY	39
5.2.3 ECAL HIT PULSE FITTING	45
5.2.4 CALIBRATION USING ELASTICALLY-SCATTERED ELECTRONS	46
5.2.5 WIDE ANGLE BREMSSTRAHLUNG FOR STUDIES OF EDGE EFFECTS	48
5.2.6 ENERGY RESOLUTION IN DATA	49
5.2.7 TIMING CALIBRATION AND PERFORMANCE	51
 6. SEARCHING FOR DISPLACED VERTICES	60
6.1 MONTE CARLO SIMULATION	60
6.1.1 RADIATIVE FRACTION	60
6.2 VERTEX RECONSTRUCTION EFFICIENCIES	61
6.3 SVT AT 0.5 MM FROM THE BEAM	62
6.3.1 L1L1	62
Cuts	62
Vertex reconstruction efficiency, ϵ_{vtx}	78
Mass resolution	83
Accidentals	87
Projected reach	89
6.3.2 L1L2	90
Cuts	91
Vertex reconstruction efficiency, ϵ_{vtx}	95
Mass resolution	97
Accidentals	99
Projected reach	100
6.3.3 L2L2	103
Cuts	103
Vertex reconstruction efficiency, ϵ_{vtx}	104
Mass resolution	106
Accidentals	107
Projected reach	107
6.4 SVT AT 1.5 MM FROM THE BEAM	108
6.4.1 L1L1	108
Cuts	109
Vertex reconstruction efficiency, ϵ_{vtx}	109
Accidentals	113
Projected reach	113
6.4.2 L1L2	115
Cuts	115
Vertex reconstruction efficiency, ϵ_{vtx}	116
Accidentals	118

Projected reach	118
6.4.3 L2L2	119
Cuts	119
Vertex reconstruction efficiency, ϵ_{vtx}	120
Accidentals	121
Projected reach	121
6.5 COMBINED REACH PROJECTIONS	123
7. VERTEX SEARCH RESULTS	127
8. CONCLUSION	128
 BIBLIOGRAPHY	129
 APPENDICES	
A	130
 VITA	131

LIST OF TABLES

Table	Page
1. Pair-1 trigger cuts	25
2. Pair-1 trigger cut values for 2015 running	27
3. Horizontal position corrections.....	36
4. Position resolution.	39
5. Cuts applied to the L1L1 datasets.....	63
6. Cuts applied to the L1L2 datasets.....	91
7. Cuts applied to the kinks in layers 1-3.	92
8. Cuts applied to the L2L2 datasets.....	104
9. Cuts applied to the L1L1 datasets with the SVT at 1.5mm.	109
10. Cuts applied to the L1L2 datasets with the SVT at 1.5 mm.....	116
11. Cuts applied to the L2L2 datasets with the SVT at 1.5 mm.....	120

LIST OF FIGURES

Figure	Page
4.1.1.CEBAF accelerator	6
4.2.1.HPS location in Hall B	7
4.2.2.HPS beamline.....	8
4.2.3.HPS magnetic fields	9
4.2.4.Charged particle trajectory in HPS beamline	10
4.2.5.HPS beamline simulation in GEMC	11
4.2.6.Harp scan showing the beam profile during May 2015 running. This particular harp scan is in the Hall B logbook, entry 3341231. The beamline profile in this scan is $122\mu\text{m}$ wide in x by $23\mu\text{m}$ in y	13
4.3.1.Rendering of the HPS SVT	15
4.4.1.Drawing of the Ecal assembly face	16
4.4.2.Single Ecal module	17
4.4.3.Photograph of Ecal crystals during assembly	18
4.4.4.LED signal in Ecal FADC	20
4.4.5.Results of a single LED run	21
4.4.6.Hamamatsu S8664-3189 large area APDs	22
4.4.7.Testing assembly for large area APDs	22
4.4.8.APD current draw versus voltage with LED on and off	23
4.4.9.APD measured dark current as a function of gain	23
4.4.10APD fixed gain in terms of voltage and temperature	24
5.2.1.Ecal energy shower correction functions from simulation	30
5.2.2.Ecal energy shower parameters for electrons relative to the inside beam gap edge .	31
5.2.3.Ecal energy shower parameters for positrons relative to the inside beam gap edge	32

5.2.4.Ecal energy shower parameters for photons relative to the inside beam gap edge	33
5.2.5.Ecal energy resolution fitted from simulation	33
5.2.6.Horizontal position correction for 1 GeV electrons	35
5.2.7.Horizontal position correction dependence for electrons	36
5.2.8.Position resolution for 1 GeV electrons.	37
5.2.9.Energy-dependent position resolution for electrons.	38
5.2.10Setup for Ecal cosmic ray calibration	40
5.2.11Simulation of energy deposited per Ecal module from cosmic rays	41
5.2.12Real cosmic ray signal in raw FADC waveform passing vertically through Ecal . . .	42
5.2.13Integrated cosmic signal in Ecal fitted for calibration	43
5.2.14Resulting 2015 gain calibration in the Ecal using cosmic ray muons shown by Ecal module position	44
5.2.15Distribution of the resulting 2015 gains in the Ecal using cosmic ray muons	44
5.2.16Pulse-fitting to Mode-1 Ecal data	46
5.2.17Reconstructed elastic peak in the Ecal for 2015 and 2016 running	47
5.2.18Energy resolution of the Ecal found in data	50
5.2.19Fitted, raw waveform of the RF signal in HPS	52
5.2.20FADC intrinsic time resolution	53
5.2.21Time difference between Ecal hits and RF time	54
5.2.22Time difference between two clusters after fine offset time correction	55
5.2.23Hit times in a cluster versus the hit energy	56
5.2.24Time walk correction for the 2016 Ecal data.	57
5.2.25Time resolution of the Ecal for the 2016 run	58
5.2.26Time resolution for the time difference between two clusters	59
6.1.1.Radiative fraction using MadGraph5 Monte Carlo and spinfix WAB.	61

6.3.1.Cut effects on the z vertex distribution for all masses in the L1L1 0.5 mm dataset.	64
6.3.2.The ratio of the z vertex distribution in the final event selection to those events in the initial event selection in the L1L1 0.5 mm dataset.	65
6.3.3.Cut effects on the two cluster time difference distribution for the L1L1 0.5 mm dataset.	66
6.3.4.The ratio of the two cluster time difference distribution in the final event selection (without the ± 2 ns cut) to those events in the initial event selection for the L1L1 0.5 mm dataset.	67
6.3.5.Cut effects on the mass distribution for the L1L1 0.5 mm dataset.	68
6.3.6.The electron and positron track χ^2 are shown with the cut indicated by the red line. This cut is an initial track selection quality cut and uses no vertex or timing information.	69
6.3.7.The maximum momentum of the electron track as shown in data (prior to cutting) and Monte Carlo. Events with higher electron energies are attributable to other types of backgrounds in the data such as elastics and wide angle bremsstrahlung and not the trident background.	70
6.3.8.The distance between the closest hit away from the beam in Layer 1 is compared to its projection at the target the track impact parameter, z_0 at the target.	71
6.3.9.The effect of a cut on the beamspot constrained χ^2 on the vertex distribution for all masses. While this plot is shown for all masses, the effects of the cut on the tails of the distribution can still be seen. The cut removes events where tracks did not pass close to eachother in space to generate a vertex and/or the vertex does not point back to the beam position at the target.	72
6.3.10The effect of a cut on the difference between the beamspot and unconstrained constrained χ^2 on the vertex distribution for all masses. The effects of the cut on the downstream tails of the distribution tells us how well a vertexed pair of tracks points back to the beamspot position at the target.	73
6.3.11The matching parameter for both electrons and positrons is shown. The maxi- mum is set to 30σ , and the cut is set to 10σ for each particle.	74
6.3.12The two cluster timing difference is shown with a fit to the Gaussian central part of the distribution. Additional smaller peaks can be seen in intervals of 2 ns in the tails of the distribution. The timing cut can remove these events where overlapping beam buckets generate out of time vertices.	75

6.3.13	The effect of the momentum asymmetry cut on the tails of the vertex distribution can be seen in the red and green curves.	76
6.3.14	Positrons that are produced from the photon in wide-angle bremsstrahlung events will have a distance of closest approach that will curve widely at the target location, yielding a largely positive value.	77
6.3.15	This plot shows that many of the tracks sharing 4 and 5 hits with the initial track selected in the event have nearly the same momentum.	78
6.3.16	35 MeV A' reconstruction efficiency versus the vertex position.	79
6.3.17	Fit that describes the L1L1 efficiency for a 30 MeV heavy photon.	80
6.3.18	The colored value is the value of the full integral from Equation (??) for the L1L1 dataset using the zCut value on the x-axis. The red line indicates the zCut value derived in data for 0.5 background events. This zCut shown is for the 10% unblinded data.	82
6.3.19	For a fixed ϵ^2 coupling, the full integral value from zCut to the first layer of the SVT is shown as a function of mass.	83
6.3.20	Fits to the residual of the A' mass peak as reconstructed in Monte Carlo.	84
6.3.21	The mass resolution from A' MC can be parameterized linearly as $p0m + p1$ with the fit values shown on the plot. The moller mass is one of the only real benchmarks to compare with the data and indicates a possible offset with the mass resolution measured in data.	85
6.3.22	The fit to the moller mass peak as found in Monte Carlo is shown. The fit uses a crystal ball function to describe the signal and a Gaussian to fit the low background under the peak.	86
6.3.23	The fit to the Moller mass peak as found in data is shown. The fit uses a crystal ball function to describe the signal and a Gaussian to fit the low mass background side to the peak.	87
6.3.24	After selecting events where the cluster time difference is greater than 3 ns and less than 9 ns, the vertex distribution for the six beam buckets is shown.	88
6.3.25	Reconstructed z vertex as a function of mass for the L1L1 dataset with the first layer of the SVT at 0.5 mm from the beam. The solid red line indicates the zCut found for 10% of the data (unblinded), and the dashed red line indicates the limit at which events have a quantile greater than 0.5 with respect to the predicted background model. The purple line shows where the projected zCut will be for the full dataset after unblinding.	89

6.3.26The expected signal yield for the full 0.5 mm 100% dataset. This uses the zCut projection shown in Figure 6.1.25.	90
6.3.27The kink distributions for tracks passing through Layer 1. The cut is shown at the red dashed line.	92
6.3.28The kink distributions for tracks passing through Layer 2. The cut is shown at the red dashed line.	93
6.3.29The kink distributions for tracks passing through Layer 3. The cut is shown at the red dashed line.	93
6.3.30The effects of the cuts on the L1L2 dataset on the unconstrained z vertex.	94
6.3.31The effects of the cuts on the L1L2 dataset on the mass distribution.	95
6.3.32The colored value is the value of the full integral from Equation (??) for the L1L2 dataset using the zCut value on the x-axis. The red line indicates the zCut value derived in data for 0.5 background events. This zCut is drawn from the zCut for the 10 % unblinded data.	97
6.3.33The fitted mass residual, or mass resolution, plotted as a function of the measured mass.	98
6.3.34The fit to the L1L2 Moller mass distribution in 10% of the data.	99
6.3.35The vertices that are produced when the time difference between the two clusters is greater than 3 ns and less than 6 ns. There are 3 approximately high z background events.	100
6.3.36The final z vertex distribution as a function of mass for the L1L2 datasets where the electron has a Layer 1 hit (shown on the left) and the positron has a Layer 1 hit (shown on the right) separately.	101
6.3.37Reconstructed z vertex as a function of mass for the L1L2 dataset with the first layer of the SVT at 0.5 mm from the beam. The solid red line indicates the zCut found for 10% of the data (unblinded), and the dashed red line indicates the limit at which events have a quantile greater than 0.5 with respect to the predicted background model. The purple line shows where the projected zCut will be for the full dataset after unblinding.	102
6.3.38The expected signal yield for the full 0.5 mm 100% dataset with L1L2 type events. This uses the zCut projection shown in Figure 6.1.37.	103

6.3.39This is the proposed zCut for the L2L2 dataset based on the efficiency curves. The three lines represent the turn on efficiency for the L2L2 dataset for the efficiency values corresponding to 2%, 5%, and 10%.	105
6.3.40The reconstructed heavy photon masses from Monte Carlo for the L2L2 dataset. Not only do the masses appear to reconstruct the wrong place, but the width of distributions indicates that we may not have the resolution to see a signal at all.	106
6.3.41Reconstructed z vertex as a function of mass for the L2L2 dataset with the first layer of the SVT at 0.5 mm from the beam.	107
6.3.42The expected signal yield for the L2L2 0.5 mm 100% dataset. This is an upper limit estimate that assumes we can remove the background in the L2L2 dataset.	108
6.4.1.35 MeV reconstruction efficiency versus the vertex position.	110
6.4.2.The colored value is the value of the full integral from Equation ?? for the L1L1 1.5 mm dataset using the zCut value on the x-axis. The red line indicates the zCut value derived in data for 0.5 background events. The zCut shown is for the 10% unblinded data.	112
6.4.3.For the measured zCut value in the 10% of the data, the corresponding integral value for various couplings across a range of masses is shown.	113
6.4.4.Reconstructed z vertex as a function of mass for the L1L1 dataset with the first layer of the SVT at 1.5 mm from the beam. The solid red line indicates the zCut found for 10% of the data (unblinded), and the dashed red line indicates the limit at which events have a quantile greater than 0.5 with respect to the predicted background model. The purple line shows where the projected zCut will be for the full dataset after unblinding.	114
6.4.5.The expected signal yield for the full 100% dataset with L1L1 1.5 mm data.	115
6.4.6.This plot, for fixed coupling ϵ^2 , shows the fraction of signal events that will be measured as a function of the integral using the vertex position along the x-axis as the <i>zCut</i> . The red line indicates the position of the <i>zCut</i> as found for the 10% sample.	117
6.4.7.Reconstructed z vertex as a function of mass for the L1L2 dataset with the first layer of the SVT at 1.5 mm from the beam. The solid red line indicates the zCut found for 10% of the data (unblinded), and the dashed red line indicates the limit at which events have a quantile greater than 0.5 with respect to the predicted background model. The purple line shows where the projected zCut will be for the full dataset after unblinding.	118
6.4.8.The expected signal yield for the full 100% dataset with the L1L2 1.5 mm data.	119

6.4.9..	121
6.4.10Reconstructed z vertex as a function of mass for the L1L1 dataset with the first layer of the SVT at 1.5 mm from the beam. The solid red line indicates the zCut found for 10% of the data (unblinded), and the dashed red line indicates the limit at which events have a quantile greater than 0.5 with respect to the predicted background model. The purple line shows where the projected zCut will be for the full dataset after unblinding.	122
6.4.11The expected signal yield for the full 100% dataset with the L2L2 1.5 mm data.	123
6.5.1.The expected signal yield for the full 100% dataset with all 0.5 mm data.	124
6.5.2.The expected signal yield for the full 100% dataset with all 1.5 mm data.	125
6.5.3.The expected signal yield for the full 100% dataset with 0.5 mm and 1.5 mm data combined.	126

CHAPTER 1

INTRODUCTION

The heavy photon, also known as the A' , is a theoretically motivated massive gauge boson that is associated with a predicted U(1) hidden symmetry, favorable to Beyond Standard Model theories. According to theory, a heavy photon kinetically mixes with the Standard Model photon through a loop-level effect generating an effective coupling to electric charge. This coupling to electric charge, ϵ , can range from 10^{-12} to 10^{-2} depending on loop order of the mixing interaction and describes the coupling of the heavy photon to electric charge to be at a scale significantly smaller than that in standard electrodynamic theory. While the coupling strength of the interaction can be naturally generated from the loop interactions, the mass is somewhat less constrained. Theories of the heavy photon as way to explain cosmological phenomena make them the simplest and possible leading interaction between the Standard Model and the Dark Sector. The Dark Sector encompasses both dark matter and dark energy particles that we cannot interact with other than the observed gravitational effects. If the heavy photon should obtain its mass through the Higgs mechanism, the mass is favored to be in the range of MeV to GeV which is compatible with dark matter theories. In such a scenario, electrons could radiate heavy photons as they do ordinary photons but at a suppressed rate. These heavy photons will have measurable lifetimes before decaying to charged particle pairs. It is natural to describe the heavy photon parameter space in terms of its coupling, ϵ^2 , and mass, $m_{A'}$.

The Heavy Photon Search (HPS) experiment searches for heavy photons in the mass range of 20-70 MeV with prompt or displaced vertices. HPS is sensitive to heavy photons radiated from an electron beam incident on a heavy target by measuring the momentum and vertex position of $e + e^-$ pairs produced from decay. By reconstructing the invariant mass and the vertex position of the pairs, HPS can look for a small bump on a large QED background using a bump hunt for prompt decays. Uniquely, HPS is also able to look for heavy photons with smaller couplings (and longer lifetimes) characterized by displaced vertices by searching for a small signal on low background downstream of the target. A Silicon Vertex Tracker (SVT) composed of six layers of silicon strips housed in a magnetic field measures particle tracks and reconstructs the vertex position of the particle pair. An electromagnetic calorimeter (Ecal) triggers event readout in addition to measuring particle energy and pair coincidence

timing. The Ecal was commissioned during a short commissioning run in December 2014. The full experiment ran in the Spring of 2015 Engineering Run and took 2.3 days of good data at approximately 50 nA with a beam energy of 1.056 GeV. HPS obtained a total of 1529 nb^{-1} of good data. Due to the commissioning of the SVT during the Engineering Run, the SVT was not moved into its nominal position with layer 1 at ± 0.5 mm from the beam until later in the running, and data was taken with the SVT slightly open at ± 1.5 mm from the beam. Additional running took place during the Spring 2016 Physics Run with a 200 nA electron beam at 2.3 GeV collecting 5.7 days of data. Future running at higher electron beam energy is planned for 2018 and beyond.

The focus of this dissertation is on the displaced vertex search for heavy photons using data with the SVT at ± 0.5 mm and ± 1.5 mm from the beam during the Engineering Run. I will give an overview of the experiment as a whole with extra detail to the areas of which I was most involved with. Significant effort was made to study the vertex analysis in the context of a blinded analysis by using 10% of the data. In order to better understand and analyze the backgrounds in the vertex search, I conducted a detailed study of the backgrounds using the statistics of the fully unblinded dataset. In addition to the full vertex analysis, I contributed significantly to the assembly, characterization and commissioning of the Ecal for all experimental running. I wrote the clustering algorithm based on that used by the CLAS experiment Inner Calorimeter (IC) and improved simulations of the Ecal detector.

CHAPTER 2

MOTIVATION

2.1 THEORY OF HEAVY PHOTONS

2.2 SIGNATURE

2.3 HEAVY PHOTONS AND DARK MATTER

2.4 EXISTING LIMITS ON HEAVY PHOTONS

CHAPTER 3

HOW TO SEARCH FOR A HEAVY PHOTON

3.1 BUMP HUNT

3.2 DETACHED VERTEX SIGNAL

3.3 TRIDENT BACKGROUND

3.3.1 BEITHE-HEITLER

3.3.2 RADIATIVE

3.4 WIDE ANGLE BREMSSTRAHLUNG

3.5 BEAM HALO

3.6 HIGH Z BACKGROUND??

CHAPTER 4

HEAVY PHOTON SEARCH EXPERIMENT

The Heavy Photon Search (HPS) experiment detector setup consists of a Silicon Vertex Tracker (SVT) and an electromagnetic calorimeter (Ecal). The SVT, located inside of a dipole magnet, measures particle momentum and vertexes $e + e -$ pairs. The Ecal triggers the readout of physics events and measures particle energy and time.

The HPS experimental setup is located in the downstream alcove of Hall B at Jefferson National Accelerator Facility. The Continuous Electron Beam Accelerator Facility (CEBAF) produces an electron beam which passes through Hall B to the alcove where the beam interacts with the HPS target housed inside the pair spectrometer magnet with the SVT. This interaction yields particle pairs and beam scattered electrons which pass through the six layers of the SVT before depositing their energy in the Ecal for event readout.

4.1 CEBAF

CEBAF (Fig. 4.1.1), an accelerator characterized by its nearly continuous duty cycle and ability to provide electron beams to multiple experimental halls simultaneously, generates the electron beam used in the HPS experiment. The CEBAF accelerator is a recirculating linac in the shape of a racetrack through which electron beam bunches can pass multiple times, boosted in energy with each pass, before being delivered to a specific hall.

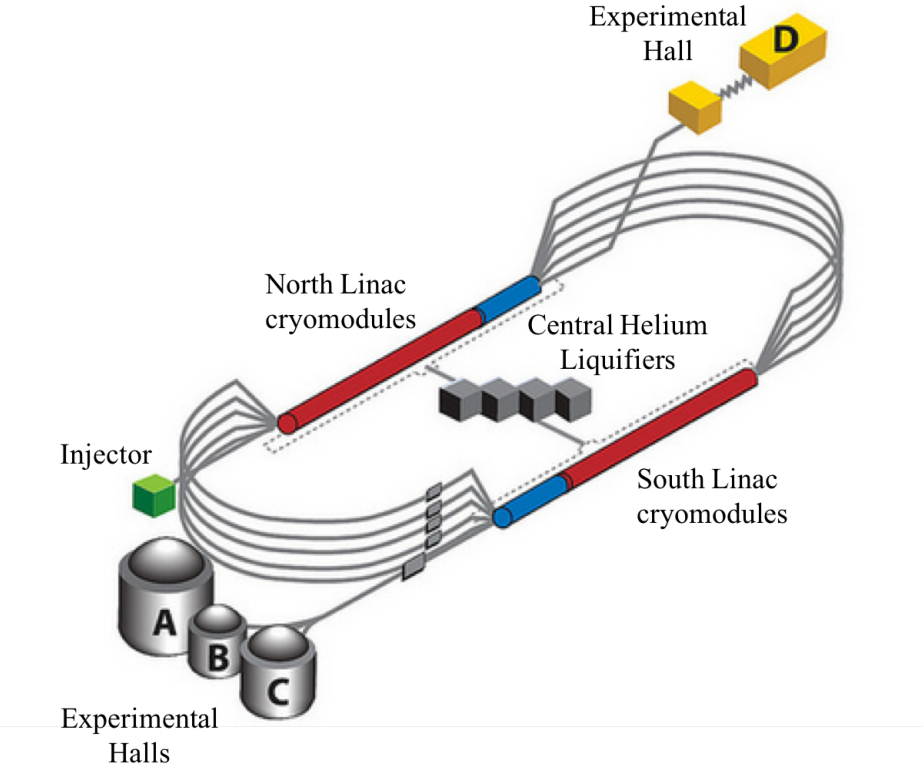


FIG. 4.1.1: The CEBAF accelerator was upgraded prior to HPS running to include additional cryomodules and central helium liquifier (CHL) for higher energy, a fifth pass, and a fourth experimental hall.

The injector energy is 100 MeV and the energy per pass was recently upgraded from 1.1 GeV to 2.2 GeV in addition to allowing a maximum of five passes (increased from the previous four pass design). These upgrades double the maximum energy output of the accelerator. While the accelerator frequency operates at 1500 MHz, a new 750 MHz RF separator had to be installed in order to provide beam to all four halls simultaneously. With these upgrades, the halls can receive beam at 250 or 500 MHz and operate at different energies [3].

HPS is the first experiment to run in Hall B after the accelerator was upgraded. After a problem occurred in one Central Helium Liquifier (CHL) during the Engineering Run in the spring of 2015, HPS obtained dedicated beam time as one of the few experiments that could continue to take physics data with the accelerator operating at a single pass using the remaining CHL. The resulting energy for the Engineering Run, 1.05 GeV, would have been impossible to obtain with the simultaneous running of other experiments requiring 2.2 GeV per pass.

4.2 BEAMLINE

The HPS experiment is installed in the downstream alcove of experimental Hall B at Jefferson Lab as shown in Fig. 4.2.1. Due to the planned construction of the CLAS12 detector in Hall B as part of the 12 GeV upgrade, HPS running was planned for nights and weekends when running beam through the hall would not interfere with CLAS12 construction. After the failure of the second CHL, HPS received dedicated, continuous running during May of 2015 in support of the Engineering Run.

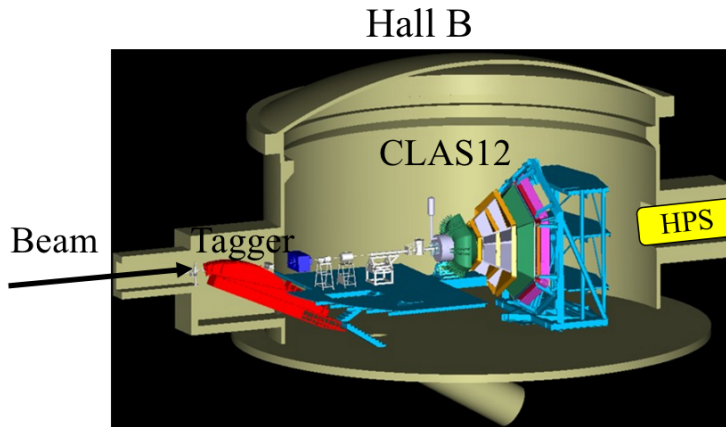


FIG. 4.2.1: The HPS experiment is in the downstream alcove of Hall B and ran while not interfering with CLAS12 construction.

The tagger magnet as depicted in Fig. 4.2.1 was used for initial beam tuning from the accelerator before sending the beam through to the HPS detectors. By energizing the tagger magnet, the electron beam was visible at the tagger dump viewer and could be aligned at the center of the viewer. Harp scans were performed to measure the position and width of the beam spot after the beam appeared to be in reasonable alignment. Once the harp scans showed the beam to be of an acceptable size and position upstream of HPS, the tagger magnet was de-gaussed for HPS running. Without the tagger magnet on, the electron beam enters the hall in vacuum and passes through the hall to the HPS setup as shown in Fig. 4.2.2.

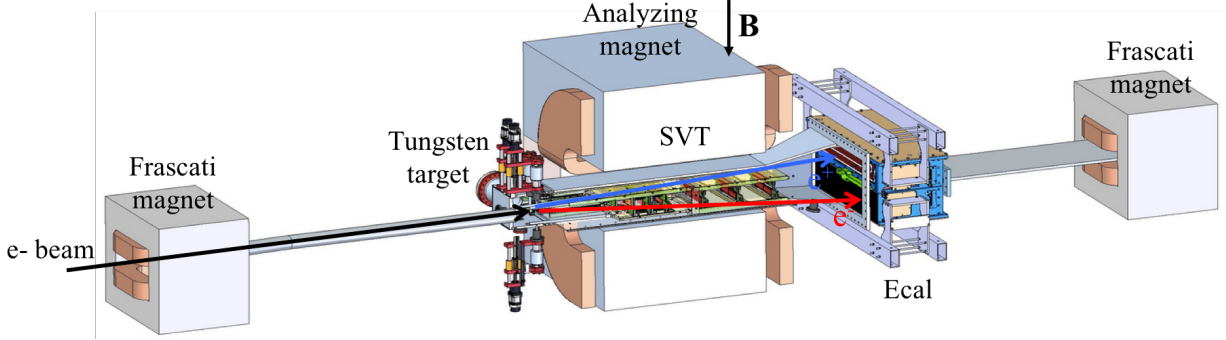


FIG. 4.2.2: The SVT and target are contained within the analyzing magnet. Particles created from the interaction of the beam at the target pass through the SVT before depositing their energy into the Ecal.

The HPS setup consists of a three-dipole chicane with fields in the vertical direction, perpendicular to the Hall B floor. The target and the SVT are housed in the central magnet known as the pair spectrometer, or analyzing magnet. The pair spectrometer has a pole length of 91.44 cm and width of 45.72 cm. For 2.2 GeV electrons, the central magnetic field of the pair spectrometer magnet is 0.5 T. For other beam energies, the analyzing magnet magnetic field is scaled accordingly. In the Engineering Run in May 2015, with a beam energy of 1.056 GeV, the pair spectrometer had a central field value of 0.24 T. The Frascati magnets, one on each side of the analyzing magnet, have magnetic fields opposite to that of the analyzing magnet such that the $\int B dl$ value of each Frascati is half of that of the analyzing magnet. This ensures that the beam will end at the same location whether the chicane is used or not and that the trajectory of beam energy electrons in the magnetic field is the same at different beam energies. The magnetic field of the HPS beam line in the chicane is shown in Fig. 4.2.3.

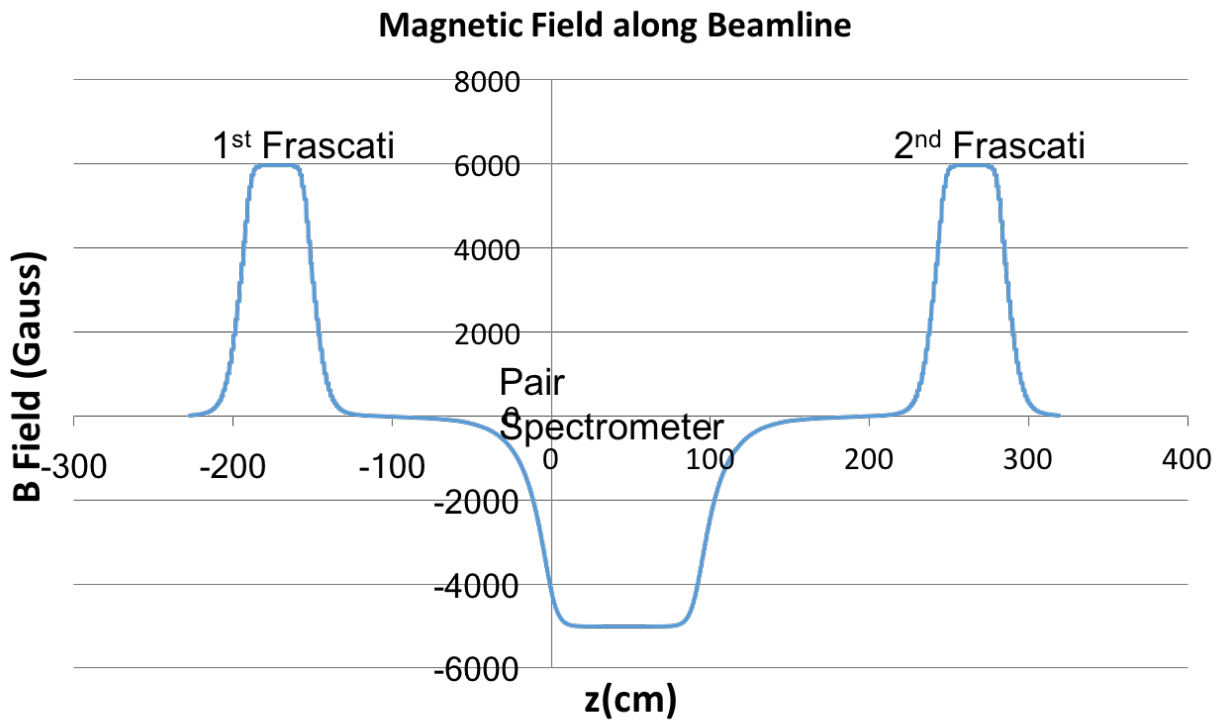


FIG. 4.2.3: The dipole field values for 2.2 GeV running.

The trajectory and position of particles inside the magnetic field, including fringe field effects, was studied using magnetic field mappings from measurements and calculation to optimize the position of the pair spectrometer magnet and vacuum chamber. The horizontal trajectory of a beam energy electron as affected by the magnetic field is shown in Fig. 4.2.4.

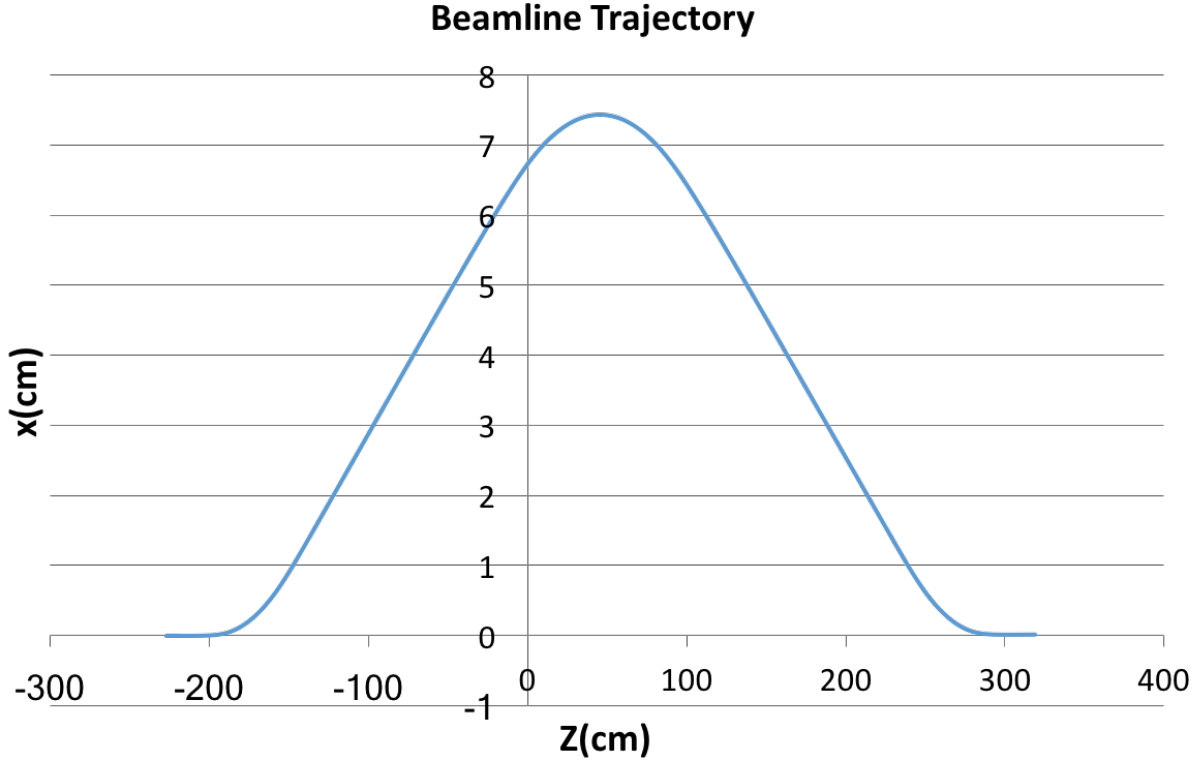


FIG. 4.2.4: The horizontal trajectory of a 2.2 GeV electron through the three dipole chicane where the target position is at $Z=0$.

In Fig. 4.2.4, the target position is where the z position is zero. The entry angle at the target was also studied and determined to be approximately 30.5 mrad. At 70 cm from the target, the pair spectrometer magnet and vacuum chamber are centered on the position of the photon trajectory from the target so that the photons pass through all subsequent vacuum chambers. The pair spectrometer magnet was placed 8.87 cm beam left, thus placing the HPS target position 2.14 cm to the right of the magnet center line. By modeling the vacuum chambers and magnetic fields in GEMC, the particle trajectories through the HPS beam line can be observed as in Fig. 4.2.5.

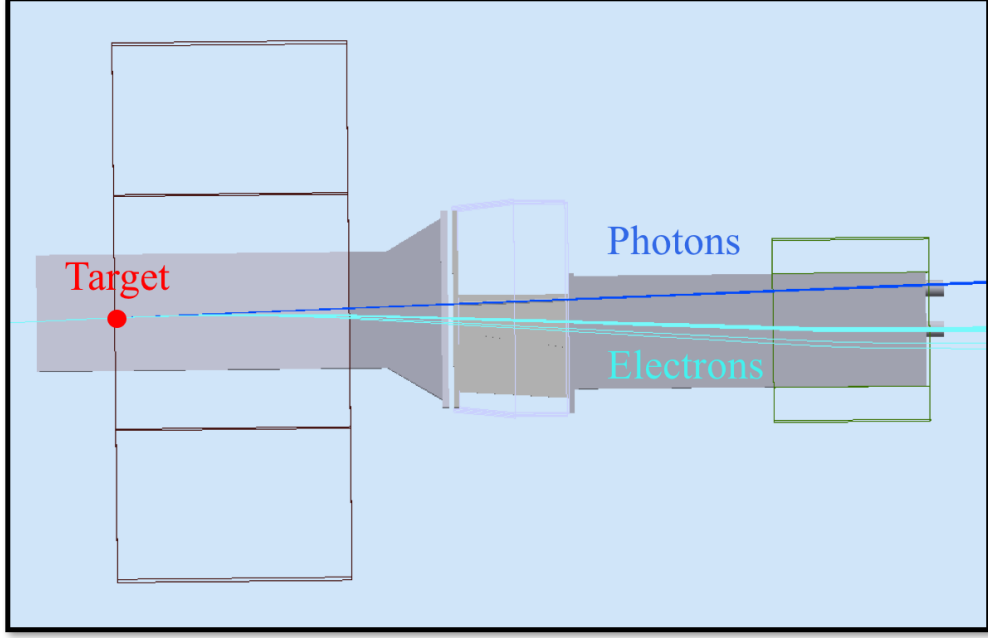


FIG. 4.2.5: A bird's eye view of the HPS beam line shows the straight line trajectory of the photons from the HPS target through the SVT, Ecal, and last vacuum chamber. The trajectory of the electrons in the magnetic field can be seen as clearly passing through the relevant cut outs in the vacuum chambers.

As shown in 4.2.5, the beam energy electrons clearly pass through the exit hole of the last vacuum chamber (contained in the second Frascati dipole) and continue traveling to the Faraday cup where the beam charge can be measured. The beam line was well-modeled in GEMC and, in real running, utilized a multitude of monitors to ensure clear passage of the beam.

The passage of the beam through the HPS beam line was monitored using beam position monitors (BPMs), wire scans with halo counters, beam viewers, and the Faraday cup. The three upstream nA BPMs give continuous beam current and position readings. These BPMs indicate if the beam is scraping the beam pipe when the current readings are different from one another. The current readings from the BPMs were compared to the current reading at the Faraday Cup (located downstream of the HPS beam line at the dump). When the beam current is at 50 nA or below, the reading at Faraday Cup current is roughly the same as the current read out by the upstream BPMs and indicates no beam scraping in the beam pipe. When operating at currents above 50 nA, it was standard to insert a beam blocker in front of the Faraday Cup in order to protect it. The beam stopper would then create an offset in the Faraday Cup current readout and the actual beam current. Additionally, a viewer screen

at the Faraday Cup was used to show the beam position. HPS used a florescent screen that showed the position of the beam by emitting light at the particular point where the beam passed on the screen. A video camera streaming a view of the screen was used for remotely observing the relative beam position on the screen.

Harp scans measure the current and position of the beam through interaction with the beam (as compared to the passive, continuous readout employed through the BPMs). A harp scan moves wires through the beam vertically, horizontally, and diagonally while downstream halo counters measure the scattered beam electron spray. The halo counters are photomultiplier tubes (PMT) strapped around the beam pipe line. The intensity of the electron spray detected by the PMTs is proportional to the beam charge that the wire interacts with. A typical harp scan from the Engineering Run is shown in Fig. 4.2.6.

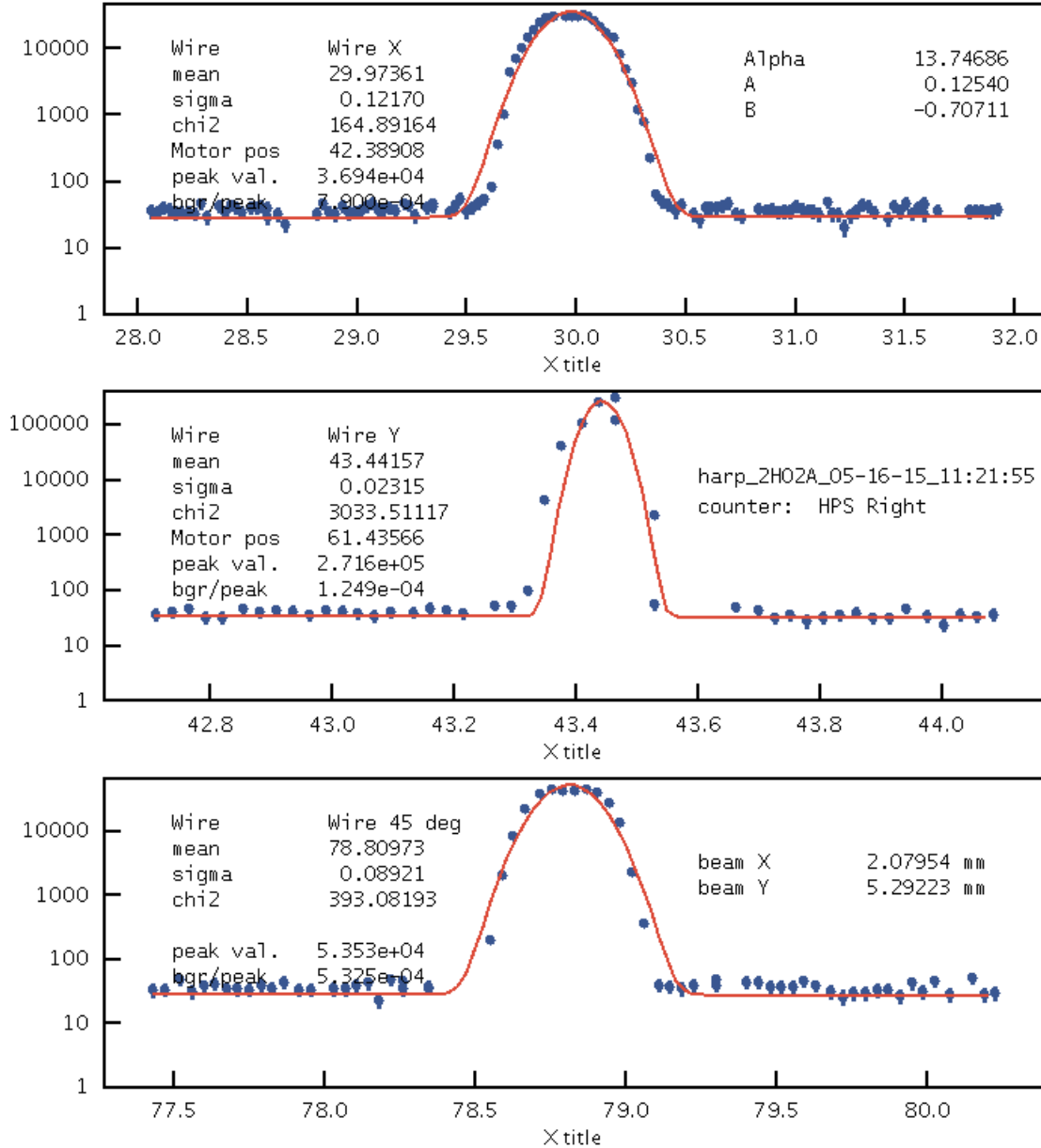


FIG. 4.2.6: Harp scan showing the beam profile during May 2015 running. This particular harp scan is in the Hall B logbook, entry 3341231. The beamline profile in this scan is 122 μm wide in x by 23 μm in y .

In Fig. 4.2.6, the beam profile is characteristically narrower in y (vertically) than in x (horizontally). The proposed beam profile for the HPS experiment was 50 μm in y and 300 μm in x in order to prevent overheating at the target and allow for precise vertex reconstruction. While overheating was not a limiting factor in the experiment, most of the 2015 running had a beam profile of no larger than 50 μm in y and 150 μm in x .

4.2.1 TARGET

The primary HPS target is a thin tungsten foil that is mounted on a support frame having the capability to be fully retracted from the beam when not in use. For proposed 1.1 GeV and 2.2 GeV running, the design thickness of the target tungsten foil is 0.125% radiation lengths (approximately 4 μm of tungsten). The measured thickness of the actual target was 0.116 %. Mounted on the same frame is a tungsten target of 0.25% radiation lengths for future running at 4.4 GeV and 6.6 GeV. The target support frame inserts the foil target from above the beam using a stepping motor linear actuator. By necessity, the bottom of the target foil is free-standing so that the target can be inserted into the active beam without interruption.

4.2.2 COLLIMATOR

A collimator is used in the HPS beamline in order to protect the silicon strips of the SVT detector in the event of the beam moving vertically from its nominal position. The collimator is a 1 cm thick tungsten plate with different sized holes through which the beam can pass. Should the beam drift vertically from its nominal position, the collimator would be able to absorb the beam and protect the silicon before the machine fast shutdown (FSD) would be triggered by excess counts in the beam halo counters. For the 2015 run, the 4 mm collimator hole was used.

4.3 SILICON VERTEX TRACKER

The Silicon Vertex Tracker (SVT) is the key detector of the HPS experiment for measuring particle momentum and trajectories through a magnetic field in order to reconstruct the invariant mass and the vertex position of the e+e- pair. The SVT is composed of six layers of 0.7% radiation length-thick silicon placed downstream of the target and housed in a vacuum chamber within the analyzing magnet. The SVT is separated into top and bottom halves with a 15 mrad opening angle, and the first layer of the SVT is at 0.5 mm from the active beam. A drawing of the SVT is shown in Figure 4.3.1.

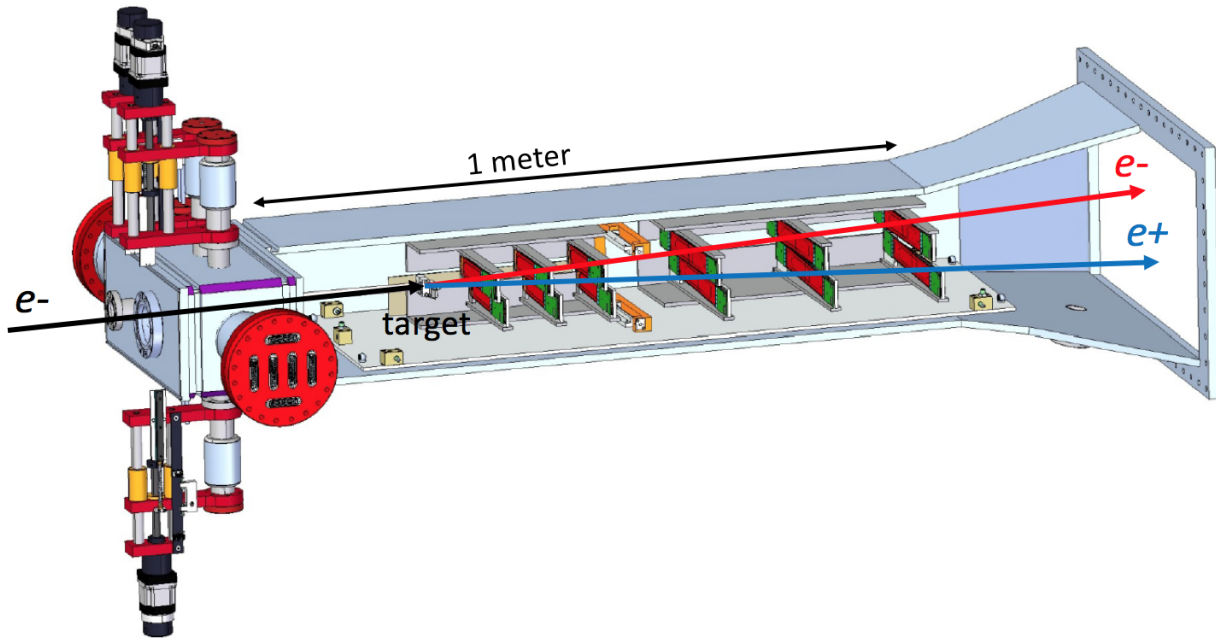


FIG. 4.3.1: A rendering of the HPS SVT. The beam enters from the left through the vacuum box. The silicon sensors are shown in red, and the hybrid readout boards are shown in green.

The SVT, as shown in Figure 4.3.1, is housed in a magnetic field such that particles are bent horizontally (field acts downward). Each of the six layers is composed of two strips capable of measuring a hit position in one dimension. By setting the strips at a stereo angle with respect to one another, each layer of the SVT is capable of three-dimensional hit reconstruction. The first three layers of the SVT are one silicon strip sensor-wide and have a stereo angle of 100 mrad between the strips. The last three layers of the SVT are two strip sensors-wide in order to better match the Ecal acceptance. The stereo angle between the sensors in layers four through six is 50 mrad. The stereo angle is not uniform throughout the SVT in order to eliminate ghost hits that can generate ghost tracks. The first five layers of the SVT cover the Ecal acceptance while the sixth layer has a slightly reduced acceptance but can be used to improve track reconstruction. The full track reconstruction only requires a minimum of five hit tracks in order to pick up tracks that may be missing hits due to an inefficiency.

The hybrid readout boards on each sensor carry the APV25 readout chips that connect the sensor to the DAQ. The power to the APV25 chips is supplied through the hybrid, and the temperature of the strip is also actively monitored at the hybrid. The heat generated by the operating hybrid is pulled out through the aluminum support structure. As the sensors

are cooled for operation, the support structure and sensor contract at slightly different rates. In order to adjust and maintain the sensor at a constant tension, one end of the sensor is attached to a spring pivot in order to maintain rigidity. The APV25 samples the strips every 24 ns and stores the results in a pipeline. Once a trigger is received, the corresponding channel pipeline is readout. The readout yields six samples at 24 ns intervals that can be fit to reconstruct the waveform. A 4-pole functional fit was used to extract the time and amplitude of the corresponding hit. A latency time that is configured in the SVT DAQ is used to correctly determine which channel pipelines are readout that correspond to the trigger. The latency time is approximately equal to the time delay of the trigger. Some early data in the Engineering Run was lost due to the SVT latency being incorrectly timed in.

4.4 ELECTROMAGNETIC CALORIMETER

The HPS Ecal is a homogeneous calorimeter composed for 442 trapezoidal PbWO₄ scintillating crystals each readout by a large area avalanche photodiode (APD) attached to the back of each crystal. The Ecal triggers events and provides particle energy and timing information.

The crystals are re-purposed from the former CLAS Inner Calorimeter detector and have been upgraded with larger avalanche photodiodes. Each crystal is trapezoidal in shape and 16 cm long with the front (back) face $1.3 \times 1.3 \text{ mm}^2$ ($1.6 \times 1.6 \text{ mm}^2$). The calorimeter layout is shown in Fig. 4.4.1.

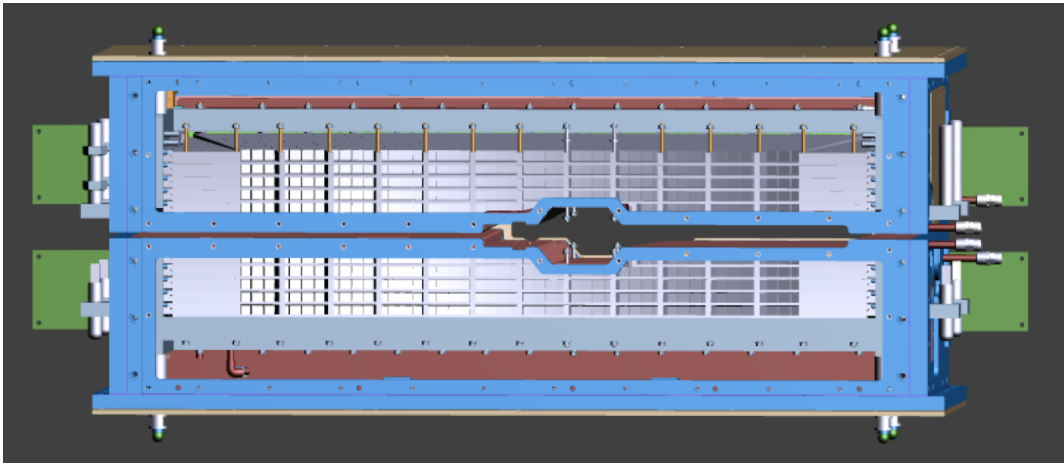


FIG. 4.4.1: Drawing of the Ecal assembly face, looking downstream with the beam direction. The Ecal is assembled in two vertical halves and has a gap in between allowing for the electron and photon beams as well as the sheet of flame.

The Ecal is constructed as two separate vertical halves in order to avoid the 15 mrad

vertical zone of excessive electromagnetic background along the beam line. The crystals in each half are arranged in five layers of 46 crystals. The layer of crystals closest to the beam in each half has nine crystals removed to allow for the passing of the electron beam. The two halves of the Ecal rest at 2 cm vertical distance from the horizontal electron beam plane.

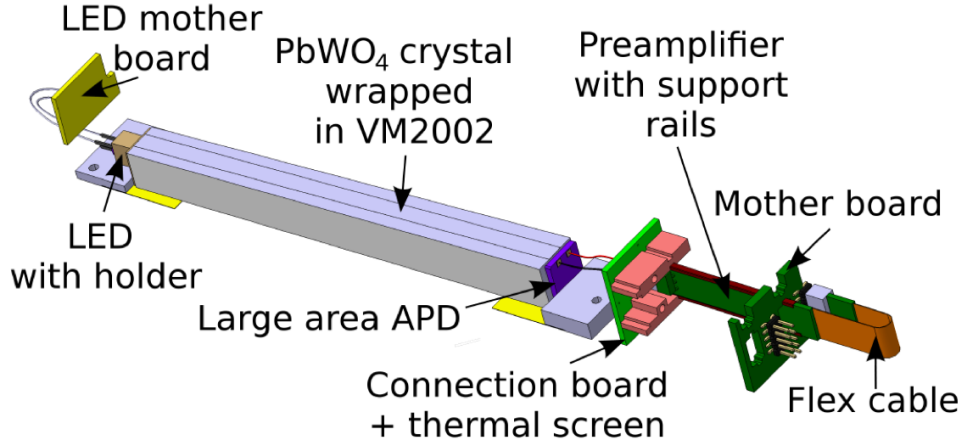


FIG. 4.4.2: Drawing of an Ecal crystal in readout configuration.

Each crystal is wrapped in a VM2002 reflecting foil in order to increase light collection. The original APDs used by the Inner Calorimeter had a surface area of $5 \times 5 \text{ mm}^2$, but these were upgraded for HPS running by replacing each original APD with a large area APD (model S8664-1010) of surface area $10 \times 10 \text{ mm}^2$. The upgraded large area APDs are capable of collecting four times the light as compared to the same energy deposited into the old APDs. The larger signals require less electronic amplification of the signal and improve the signal-to noise-ratio. Ultimately, the upgrade in electronics requires a lower energy threshold for module readout and improves energy resolution.

As a particle deposits its energy into the scintillating crystal, the photons are collected at the back of the crystal by the APD and converted into an electronic signal via the photoelectric effect. Each APD is attached by a twisted pair connector to a preamplifier which converts the signal current to voltage and has low input impedance and noise.



FIG. 4.4.3: Photograph taken during assembly of the Ecal from above. The preamplifiers attached to each crystal are shown on the left. A single layer of wrapped crystals are shown in their tray and the LEDs attached to each crystal are shown on the right.

The gain of the APDs and the scintillation of the crystals in the Ecal are temperature-dependent effects. An Anova A-40 external chiller operating at 17°C pumps cool water through copper cooling pipes that run along the inside of the Ecal at the top, bottom, front and back face of the crystal structure. The internal temperature of the Ecal was monitored using sixteen thermocouples located at various locations within the Ecal structure. The thermocouples are readout using an Omega D5000 series transmitters. Both devices are connected through RS-232 serial communications for external monitoring and alarms should the temperature change significantly.

Low voltage is supplied to the preamplifiers via an Agilent 6221 operating at 5 V and approximately 4.1 A when all preamplifiers are connected. The high voltage to each of the 52 APD groups is supplied by the CAEN A1520P modules in the SY4527 mainframe. Both voltage suppliers are monitored and accessible for remote operations.

4.4.1 LIGHT MONITORING SYSTEM

The Light Monitoring System (LMS) is a design upgrade addition to the Ecal consisting of a bi-color LED attached to the front of each Ecal module and capable of being controlled remotely. PbWO₄ scintillating crystals are relatively radiation tolerant but have a known decrease in light yield after exposure to radiation [4]. This effect is non-uniform in the Ecal as a module's geometrical position relative to the beam will result in different levels of radiation. The LMS has the ability to turn individual modules on and off independently which proved useful in checking each channel's functionality and correct cabling. The use of LEDs in a monitoring system for the PbWO₄ modules is particularly advantageous because the LEDs can be selected such that the shape and duration of the emitted flash can generate a pulse shape similar to the scintillation effect in the crystal [6].

Each crystal has a plastic LED holder glued to the front that contains a bi-color LED, model RAPID 56-0352, capable of emitting red and blue light. The use of two different colors allows for the study of different effects in the Ecal modules. The blue LED has a wavelength close to the 430 nm emission peak of PbWO₄ [6] and is used to check for radiation damage in the crystal as this spectrum would be most affected. The red light is not susceptible to the radiation effects in the crystals, but is useful for checking the stability of the APD gains.

The LMS consists of four driver boards on each half of the Ecal. The four driver boards on each half are connected to one of two main controllers, and each driver can turn on a single LED at a time. The controllers provide communication with the LMS through ethernet and USB interfaces. The controller board for the top half of the Ecal also contains the master clock signal that sets the rate at which the LEDs flash. This clock signal is sent to the bottom controller so that the driver boards on the bottom half of the Ecal can flash at the same rate, and the clock signal is used to trigger LED events when the DAQ is used.

During the initial assembly of the Ecal, the LEDs were used to study the cross talk between Ecal modules. The cross talk between channels was found to be at the level of $2\pm1\%$ and generally occurred in modules of the same row to the immediate left and right of the triggered module. The effect most likely appears due to light leakage out the back face of the crystal where the APD does not cover the entire surface.

The raw waveform response from a red LED signal in a single Ecal module is shown in Fig. 4.4.4. The raw units are given in mV which are a factor of four times less than the units of FADC.

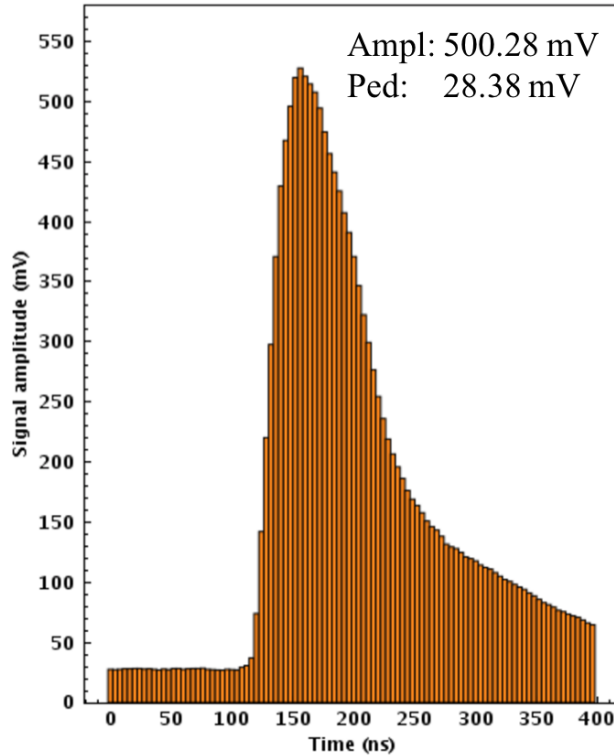


FIG. 4.4.4: A red LED in a single Ecal module as readout through the FADC.

Before and after periods of long beam running, an LED test was run so that the general gains of the Ecal could be checked. The LED test ran a sequence of red and blue LEDs so that the characteristic response of each module was measured. The typical results from an LED test are shown in Fig. 4.4.5.

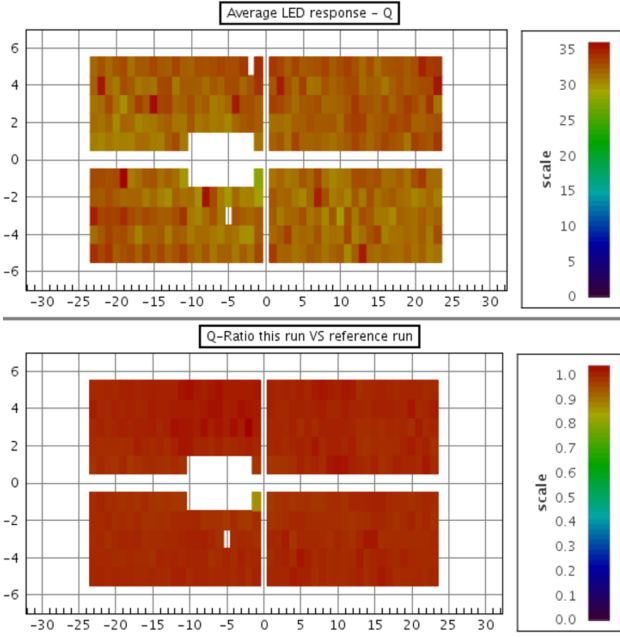


FIG. 4.4.5: The top shows the LED response in each crystal for a specific LED run. The bottom compares each crystal with its database value as stored from a previous LED run.

As shown in Fig. 4.4.5, the individual Ecal module response is given as the pulse-integral in units of GeV. The response values for individual crystals have large units of energy because the LED pulse is so much longer than an actual scintillation pulse in the crystal. A LED test can show differences in the gains of individual crystals on the order of 1% when compared to previous LED test results. During the spring 2015 running, a 5% change in gains occurred over the course of establishing production beam between February and April. This change was seen in LED response studies in addition to the gains obtained with cosmic energy calibration.

4.4.2 AVALANCHE PHOTODIODES

A significant electronics upgrade to the Ecal was the introduction of large area Hamamatsu S8664-3189 APDs for readout. APDs are ideal for reading out the Ecal modules due to their ability to operate in the fringe magnetic field of the HPS beam line. Both the Institut de Physique Nucléaire d'Orsay (IPN) and Instituto Nazionale di Fisica Nucleare (INFN) groups in the HPS collaboration purchased the large area APDs for upgrade. As the IPN group re-designed the motherboards for the upgrade, INFN developed the testing apparatus so that the gains of each APD could be characterized and sorted into one of 52 high voltage groups to minimize gain variations. The large area APDs are shown in Fig. 4.4.6.

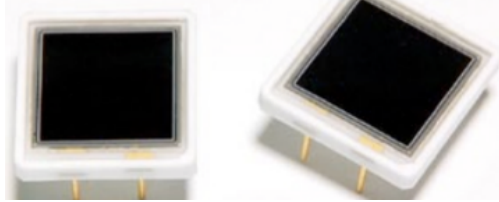


FIG. 4.4.6: The Hamamatsu S8664-3189 large area APDs.

APDs are reverse-biased diodes with an internal high electric field used to multiply the charge carriers through an avalanche mechanism. The characteristic gain of APDs is highly dependent on the temperature of the environment due to the interaction of the charge carriers with the phonons. The gain is higher for lower temperatures. The APD gains have a linear dependence on both voltage and temperature. Prior to grouping the APDs for installation in the Ecal, each APD was tested and bench marked to check for quality and optimal operating voltage in order to achieve a pre-selected gain of 150. The testing apparatus was designed and installed by the group from INFN as the same procedure was used in the construction of the Forward Tagger [5]. The bench marking apparatus is shown in Fig. 4.4.7.



FIG. 4.4.7: On the left, the testing setup is shown and includes a chiller, the light-tight plastic box that contains the LEDs and APDs, an electrometer, and the data acquisition. On the right, the setup inside of the light-tight plastic box is shown that contains a copper cooling plate to maintain the chiller temperature, 10 slots on each side to hold APDs, and the LED in the center of each half.

In order to avoid condensation on the cooling lines, the temperature range for conducting the tests was limited to 16°C, 18°C, and 20°C. During the testing, the current in each APD is measured by the electrometer with the LED on and off while stepping through a range of voltages. The measured dark and light currents for an individual APD during testing are shown in Fig. 4.4.8.

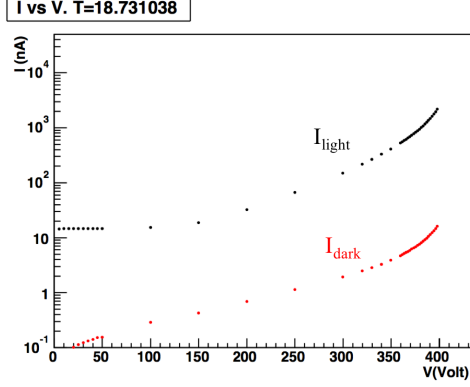


FIG. 4.4.8: The current measured from an individual APD as tested over a range of voltages with both the LED on and off. The measured temperature at the APD for this particular measurement was 18.7 degC.

The full characterization of the APD gain is calculated by the following relation:

$$Gain = \frac{I_{light}(V) - I_{dark}(V)}{I_{light}(G = 1) - I_{dark}(G = 1)} \quad (4.4.1)$$

The gain is determined to be 1 when the avalanche mechanism is not present. The $I_{light}(G = 1)$ in Eq. (5.2.10) the corresponding light current and $I_{dark}(G = 1)$ is the measured dark current when the gain is 1. Using this relation, the gain can be characterized for all measured dark currents and should have a linear relation. This relationship is shown in Fig. 4.4.9.

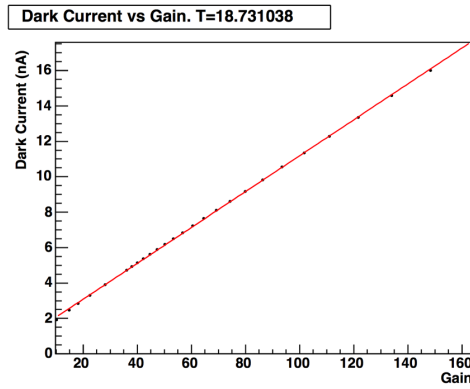


FIG. 4.4.9: The current measured from an individual APD as tested over a range of voltages with both the LED on and off. The measured temperature at the APD for this particular measurement was 18.7 °C.

If the relationship between the dark current and the gain is not linear, as shown in Fig. 4.4.9, then the APD was re-tested to ensure quality. In order to appropriately group APDs for common high voltage inputs from the motherboard and minimize gain variations across the Ecal, APDs were placed into 52 common voltage groups ranging from as little as two to maximum ten APDs in each group. The grouping temperature was chosen to be 18 °C in order to avoid condensation in the cooling lines of the Ecal. The optimal voltage for each APD at 18 °C and a pre-selected gain of 150 can be extrapolated as shown in Fig. 4.4.10.

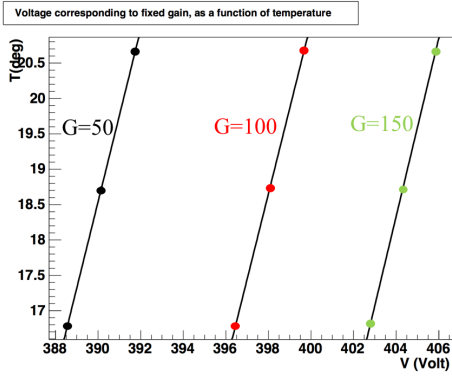


FIG. 4.4.10: The calculated voltages for fixed gains as a function of temperature can be used for group the APDs into appropriate high voltage groups.

4.5 TRIGGER

Events of interest in the HPS experiment are triggered by the Ecal. Each channel of the Ecal is readout to an FADC250 of which 16 signals are connected to each board. The FADC250 continuously samples analog signals at a rate of 250 MHz, or every 4 ns, and has 12-bit precision. As the data size was not considered over burdensome, the 2015 and 2016 data was recorded in raw mode such that 100 samples of raw information in a channel are readout at the trigger time. This raw mode, called Mode 1, allowed for precise offline pulse fitting of the signals for optimal energy resolution and improved timing resolution.

When a signal crosses a pre-defined threshold, a set number of samples before and after the crossing are summed together to provide a pulse charge value which is converted to energy. The conversion to energy requires access to the individual channel gains and pedestals (as found by cosmic calibrations) which are pre-loaded into the data acquisition (DAQ) system. The energy and time of threshold crossing are sent to the General Trigger Processor (GTP) board every 16 ns for clustering.

The GTP clusterer first identifies the crystals carrying the highest energy of all surrounding crystals, also known as seed crystals. The immediately neighboring crystals of the seed hit are compared in both energy and timing coincident with respect to the seed crystal in order to create a cluster. The cluster energy is the sum of all of the hits in a cluster. The timing coincidence is typically chosen to be 4 samples to allow for time-walk effects. The cluster information is then passed to the Subsystem Processor (SSP) to make a trigger decision based on various settable trigger cut requirements.

The SSP includes several different configurations that can run simultaneously containing different settable cuts and prescale values for Ecal modules. The SSP looks for combinations of clusters that pass the configuration requirements and cuts and then sends a trigger to the Trigger Supervisor (TS) board when a cluster or pair of clusters satisfies the trigger requirements. The trigger is then sent to the Trigger Interface (TI) boards in order to trigger readout of all detectors.

The SSP trigger configurations include two cluster pairs triggers, two single cluster triggers, a random pulser trigger, a cosmic trigger, and an LED trigger of which all except for the cosmic and LED trigger were run during data taking with beam. The single cluster trigger, Single-1, was optimized for elastically-scattered beam energy electrons off the target. The looser version of the trigger was Single-0. These triggers were useful in selecting events for calibrating the Ecal and studying the trigger efficiencies. The cluster pairs trigger is the primary trigger for the HPS experiment and studies all possible combinations of clusters in the Ecal for pairs selection. The tuneable cuts used in this trigger are presented in Table 1.

TABLE 1: Pair-1 trigger cuts

Trigger cut	Cut value
Time difference	$ t_{top} - t_{bot} \leq t_{coincidence}$
Cluster energy	$E_{min} < E_i < E_{max}$
Cluster sum	$E_{summin} \leq E_1 + E_2 \leq E_{summax}$
Cluster size	$N_{hits} \geq N_{threshold}$
Energy difference	$E_2 - E_1 < E_{difference}$
Coplanarity	$ \arctan \frac{x_1}{y_1} - \arctan \frac{x_2}{y_2} \leq \theta_{coplanarity}$
Energy-distance	$E_1 + r_1 F \geq E_{slope}$

In Table 1, the variables t_i , E_i , N_i , x_i , and y_i denote the cluster time, cluster energy, number of hits in the cluster, and coordinates of the cluster, respectively. The subscript,

1 denotes the cluster with the lowest energy of the pair. The parameters selected for the cuts include the $t_{coincidence}$, E_{min} , E_{max} , E_{summin} , E_{summax} , $N_{threshold}$, $E_{difference}$, $\theta_{coplanarity}$, r_1 , and E_{slope} , and are chosen from studying A' Monte Carlo in order to optimize the signal acceptance while minimizing the background. The parameter, r_1 , is the distance between the center of the lowest energy cluster and the center of the Ecal (defined as $r_1 = \sqrt{x_1^2 + y_1^2}$). The GTP clusters that are created are prior to track-matching and offline clustering (which further includes hits belonging to a cluster beyond those immediately adjacent to the seed hit). For the 2015 data, a GTP cluster conserves roughly 80 % of the fully reconstructed particle energy when the seed hit is not on the edge of the Ecal.

The time coincidence cut is kept loose enough in the SSP pairs cluster selection to allow for time walk and cabling offsets which are not corrected for until the full pulse is fitted in offline reconstruction. At the GTP stage, the time only corresponds to threshold crossing. The cluster energy cut is inclusive of clusters that are reconstructed by the GTP in the energy range of interest. The minimum hit requirement for clusters was lowered at the start of running due to A' Monte Carlo studies indicating that 1 hit clusters were possible and could improve reach without overburdening the trigger. The cluster sum cut is most significant in removing accidental pairs events with two elastically-scattered beam energy electrons in addition to removing low energy cluster sum events that will not pass thresholds for well-reconstructed events. The energy difference cut removes events that have extremely different cluster energies and do not satisfy A'-type criteria.

The coplanarity cut removes events that are not coplanar including Moller and Wide Angle Bremsstrahlung backgrounds because the e+e- trident events of interest are distributed symmetrically around the beamline. The angle is calculated from the center of the Ecal where the beam line passes through to each cluster in the pair relative to the vertical axis. The pairs should be approximately 180° apart.

The energy-distance cut is applied to the lowest-energy cluster of the pair in order to reject events where the low energy cluster is too close to the beam passing through the Ecal. Trident kinematics show that there is some reasonable distance of separation from the beamline for these lower energy events and that most of these clusters are dominated by bremsstrahlung low energy photons. The cut values used in the 2015 Pair-1 trigger are shown in Table 2.

TABLE 2: Pair-1 trigger cut values for 2015 running

Trigger cut	Cut value
Time difference	$ t_{top} - t_{bot} \leq 12$ ns
Cluster energy	$54 < E < 630$ MeV
Cluster size	$N_{hits} \geq 1$
Energy sum	$180 < E_{top} + E_{bot} < 860$ MeV
Energy difference	$ E_{top} - E_{bot} < 540$ MeV
Coplanarity	$\theta_{top} - \theta_{bot} < 30^\circ$
Energy-distance	$E_1 + (5.5\text{MeV/mm})r_1 > 600$ MeV

The pulser trigger generates a constant rate of triggers at 100 Hz regardless of the physics events as measured by the Ecal. This makes the pulser an unbiased probe for measuring the backgrounds of the experiment and was able to run during running with the beam concurrently with other triggers.

The cosmic trigger was used without beam for calibration of the Ecal and uses the timing coincidence between two scintillators, placed below and external to the Ecal, in order to trigger readout of all Ecal channels for offline reconstruction of the cosmic event. The timing coincidence of the scintillators placed in line and below the Ecal was chosen to be 40 ns where the leading edge of the scintillator signal in the FADC pulse crosses 60 ADC. Once the timing and threshold conditions are met, all modules in the Ecal are readout in Mode-1 (raw ADC waveform) format.

CHAPTER 5

DETECTOR CALIBRATION AND PERFORMANCE

The first detector to be commissioned was the Ecal during preliminary running with a 2 GeV electron beam in Hall B in December 2014. The Ecal was initially calibrated prior to receiving any beam using cosmic energy deposition in the crystals. The Ecal demonstrated that all channels worked and the full readout using FADCs was useful for setting up the DAQ for future running. The SVT was installed in the early spring of 2015 and performed fully during the Engineering Run in the Spring 2015 at Jefferson Lab. The single pass beam energy was 1.056 GeV and was sufficient for not only detector commissioning but also calibration and physics analysis.

5.1 SILICON VERTEX TRACKER PERFORMANCE

The SVT momentum calibration is primarily guided by the accuracy of the alignment in the magnetic field. Tracks on both top and bottom for elastically-scattered electrons should peak at the same beam energy at the same resolution. The Billoir vertexing algorithm is the method by which two tracks are re-fit to create a vertex. The invariant mass is reconstructed from the vertex of the two tracks.

5.1.1 MØLLER MASS

5.1.2 MOMENTUM RESOLUTION

5.1.3 TRACKING EFFICIENCY

(Include discussion on layer efficiency, 3 prong tracking efficiencies, moller mass, and fee peak.)

5.2 ELECTROMAGNETIC CALORIMETER CALIBRATION

The Ecal was calibrated both in energy and time. The first calibration performed, before receiving beam, was the cosmic ray energy calibration. A full timing calibration of the Ecal

was also performed using the accelerator RF signal. A final calibration using physics events from elastically-scattered beam energy electrons and events from wide angle bremsstrahlung yielded the full calibration of the Ecal for all energies and characterized the energy resolution.

5.2.1 SIMULATIONS

The Ecal uses an adapted version of the clustering algorithm that was used by the CLAS Inner Calorimeter (IC). While the HPS Ecal re-uses the IC crystals, the geometrical arrangement differs greatly and merits detailed studies and simulations in order to reconstruct and the incident particle energy. In the HPS Ecal, the angles of incidence of the particles (electrons, positrons, and photons) has a wider spread over the angles of incidence. Additionally, there are more edge effects in the HPS Ecal than in the IC due to the horizontal split for the beam between the top and bottom halves.

Simulations were performed using the detector geometry HPS-EngRun2015-Nominal-v3 detector model in SLIC as part of the hps software package. The detector includes all strips of the SVT, vacuum chambers and flanges, and the Ecal crystals with a honeycomb material in the Ecal vacuum chamber for structural support. The detector also steps particles through a 3D field map corresponding to the currents for 1 GeV beam running.

Single particles: electrons, positrons, and photons were simulated at discrete energies of 0.2, 0.3, 0.4, 0.5, 0.6, 0.7, 0.8, 0.9, 1.0, and 1.1 GeV in order to uniformly cover the ranger of energies detectable in the spring 2015 running at 1.05 GeV. The simulation fully utilizes the procedure for HPS Monte Carlo reconstruction which differs slightly from the individual hit readout methods used in HPS production Monte Carlo because the events exclude pile-up effects. The offline cluster reconstruction uses the same thresholds used in data and production Monte Carlo: 7.5 MeV for individual hits, 50 MeV for seed hits in clusters, and 100 MeV for cluster energies.

Energy reconstruction

As a particle enters the Ecal, it deposits all of its energy in an electromagnetic shower by either bremsstrahlung or pair production. The secondary particles then produce more particles through bremsstrahlung and photon pair production giving rise to a cascade of particles, decreasing in energy. After the electron energy is too low to yield further particles, the remaining energy is deposited through ionization and excitation releasing scintillation photons in the lead tungstate crystal that are gathered at the back of the crystal with

an APD that converts the number of collected photons into an electronic signal via the photoelectric effect. Due to the complex showering cascade that occurs when a particle deposits its energy in the Ecal, several adjacent crystal modules will contain some fraction of the incident energy of the particle. These modules are clustered in offline reconstruction to obtain the total measured energy of the incident particle. The reconstructed energy not corrected for shower loss effects is defined by Equation (5.2.1).

$$E_{rec} = \sum_i E_i \quad (5.2.1)$$

In Equation (5.2.1), the subscript i pertains to each module in the cluster such that E_i is the energy of each module in the cluster. A proportion of the incident particle energy is lost between crystals and out the back of the crystal where the APD does not fully cover the surface of each crystal. After recovering the energy as measured by the Ecal, the incident particle energy can be found by correcting for the shower loss effects as described by Equation (5.2.2).

$$E_{corr} = \frac{E_{rec}}{f} \quad (5.2.2)$$

In Equation (5.2.2), f is the energy-dependent ratio of measured vs incident particle energy. This factor is obtained through simulation. The energy loss corrections as derived from Monte Carlo are shown in Fig. 5.2.1.

The difference in the energy corrections for the various particle types arises from geometrical effects and the incident angles of the particles in the crystals. The focal point of the calorimeter, the point at which all crystals are fanned around, lies 80 cm from the front face of the Ecal. The HPS target is outside this focal distance at approximately 1.3 m from the face of the Ecal in the magnetic field of the pair spectrometer. Additionally, the target is offset beam right in the pair spectrometer magnetic field. The momentum of the particles produced at the target causes charged particles to take different trajectories from the target to the Ecal and, therefore, the entry angle into a crystal, as experienced by each particle type, is different depending on the incident energy. The form of the energy correction function for the central region of the Ecal is described by a three parameter fit in Eq. (5.2.3).

$$\frac{E_{rec}}{E_{gen}} = \frac{A}{E_{rec}} + \frac{B}{\sqrt{E_{rec}}} + C \quad (5.2.3)$$

In Eq. (5.2.3), E_{rec} refers to the reconstructed energy in the Ecal, and E_{gen} refers to the initial particle energy as generated by Monte Carlo. The shower leakage effects in crystals

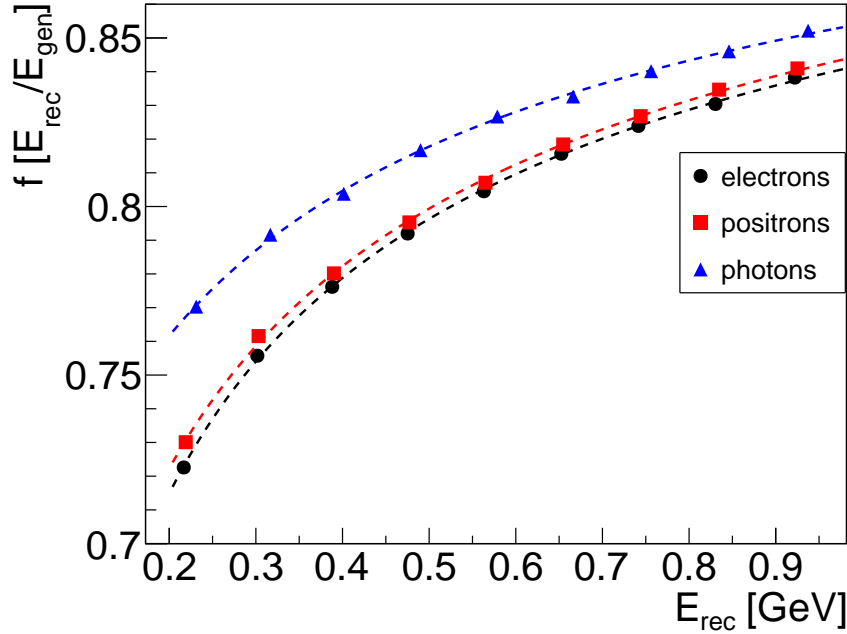


FIG. 5.2.1: Energy correction functions correct the energy measured in the Ecal to reconstruct the energy of the incident particle.

becomes significant at distances close to the edge. The energy reconstruction deteriorates rapidly in the crystal closest to the beam gap, but stabilizes in central region of the Ecal before dropping off rapidly in the outermost crystals of the Ecal (layers ± 5). The energy leakage at the edges was fully characterized using Monte Carlo as a function of position in the Ecal relative to the inner beam gap edge. In Equation (5.2.3), parameter A is not strongly correlated with position and remains as a constant for a given particle type. The parameters B and C do depend on cluster position relative to the beam gap edge of the Ecal. These dependencies can be seen for electrons in Fig. 5.2.2.

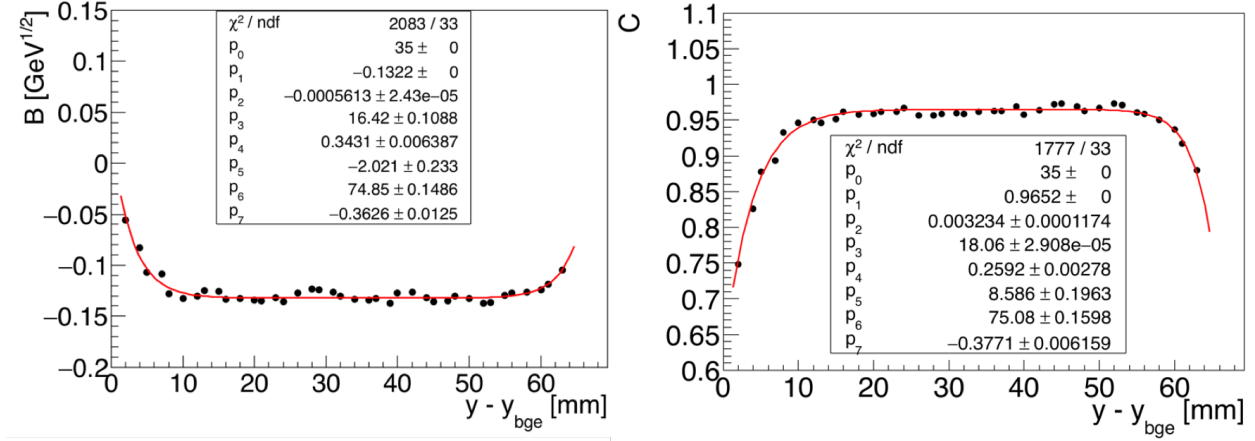


FIG. 5.2.2: Parameters B and C from Eq. 5.2.3 for electrons, as a function of vertical position relative to the innermost beam gap edge.

As shown in Fig. 5.2.2, the energy leakage parameters B and C can be fit with two functions at the edges that match in the central region of the Ecal, away from the edges of the calorimeter. The equations used to fit the B and C parameters are described by Equations (5.2.4) and (5.2.5), respectively.

$$\begin{aligned} B(y < p_0) &= p_1 - p_2 e^{-(y-p_3)p_4} \\ B(y > p_0) &= p_1 - p_5 e^{-(y-p_6)p_7} \end{aligned} \quad (5.2.4)$$

$$\begin{aligned} C(y < p_0) &= p_1 - p_2 e^{-(y-p_3)p_4} \\ C(y > p_0) &= p_1 - p_5 e^{-(y-p_6)p_7} \end{aligned} \quad (5.2.5)$$

The energy leakage correction functions are relatively stable in the central region of the calorimeter and are matched at a central value p_0 . For columns containing 5 crystals vertically, the distance to the beam gap edge is simply the absolute value of the distance from the cluster centroid to the innermost beam gap edge. In the regions above and below the region where row 1 crystals are removed in the Ecal, additional consideration must be made in calculating the distance to the inner beam gap edge in order to be consistent with other regions of the Ecal. For completeness, the corresponding energy correction parameters for positrons and photons are seen in Figures 5.2.3 and 5.2.4, respectively.

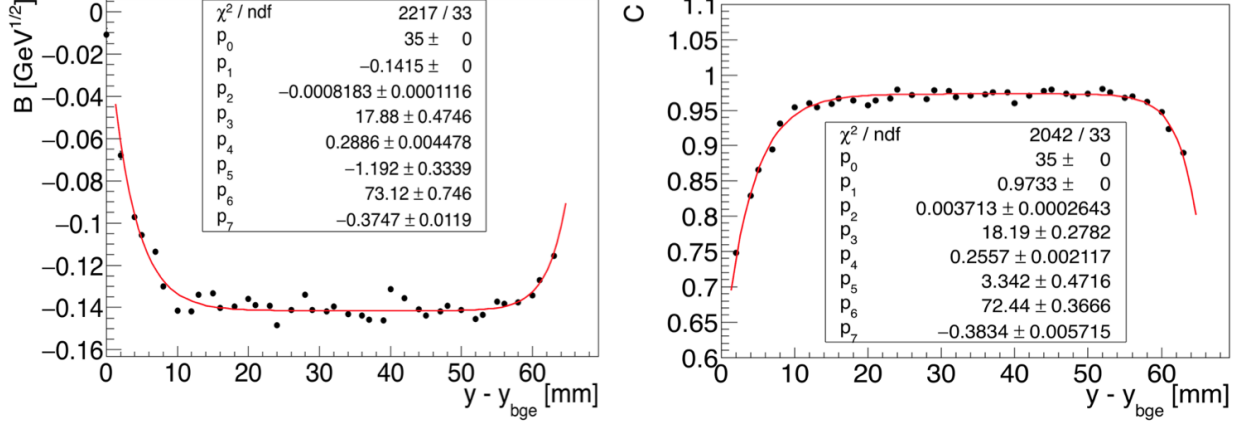


FIG. 5.2.3: Parameters B and C from Eq. 5.2.3 for positrons, as a function of vertical position relative to the innermost beam gap edge.

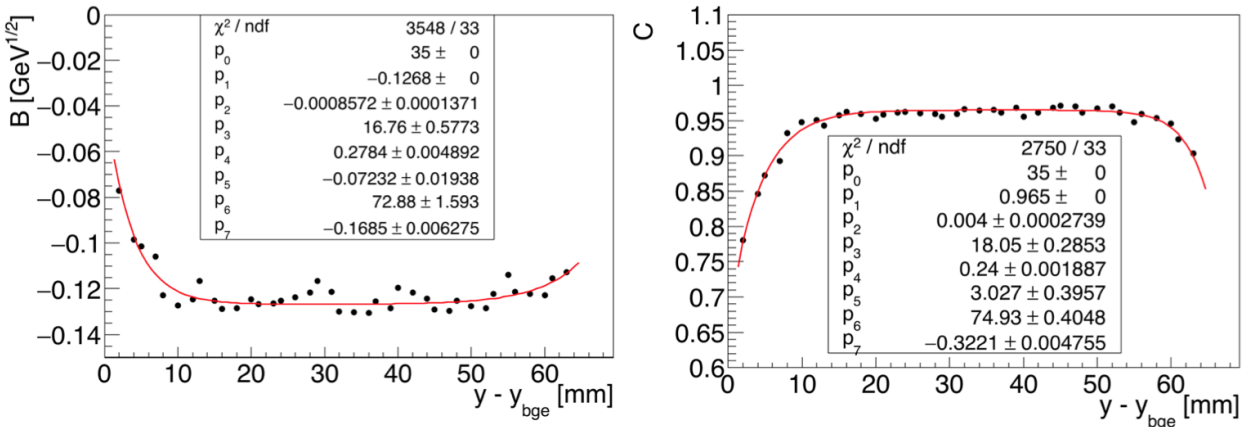


FIG. 5.2.4: Parameters B and C from Eq. 5.2.3 for photons, as a function of vertical position relative to the innermost beam gap edge.

As one can see, the energy corrections are relatively constant at approximately 1 cm from the edges of the Ecal. As a result, we define the fiducial the region of the Ecal to be at greater than 1 cm from the edge, or approximately 3/4 of the font face crystal dimension. This result is consistent with the findings for the CLAS IC.

Energy resolution

The energy resolution of the Ecal is energy-dependent and improves with energy as $1/\sqrt{E}$. From simulation, we obtain the energy resolution as shown in Figure 5.2.5.

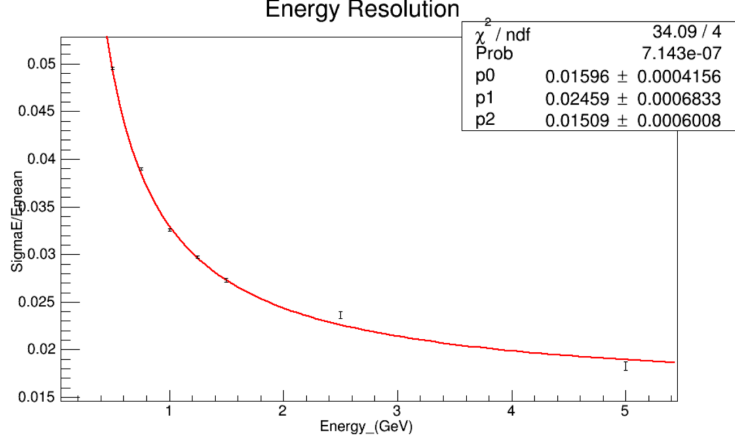


FIG. 5.2.5: Ecal energy resolution from simulation.

The fit to Figure 5.2.5 is described by Equation 5.2.6.

$$\frac{\sigma_E}{E}(\%) = \frac{1.60}{E} \bigoplus \frac{2.46}{\sqrt{E}} \bigoplus 1.51 \quad (5.2.6)$$

The first term corresponds to the preamplifier noise. We were expecting $3 \text{ MeV} \times \sqrt{10} = 0.009 \text{ GeV}$, where 10 is the average number of hit crystals. This term from simulation is not including the FADC error (expected to be 1.3 MeV [8]) which contributes a term (in %) as $0.13\sqrt{10}/E$ to be added, quadratically. The second term corresponds to the statistical fluctuations in the shower development and is influenced by the lateral containment of the shower and energy deposited in the crystal module. The second term from simulation is not including fluctuations in the number of photoelectrons (30 photoelectrons/MeV, multiplied by an excess noise factor parameterizing the fluctuations in the APD gain process, or Fano factor, of around 2 [10]) contributing $0.8/\sqrt{E}$. This term is calculated as $\sqrt{F/N_{pe/GeV}}$. The third term is interpreted as the fluctuation of energy leakage through the back of the crystals. This third term should also include the crystal-to crystal inter-calibration error which we hope to maintain at approximately 1 %. By including these additional resolution effects in the measurement, we obtain the anticipated resolution in Equation (5.2.7).

$$\frac{\sigma_E}{E}(\%) = \frac{1.65}{E} \bigoplus \frac{2.59}{\sqrt{E}} \bigoplus 1.81 \quad (5.2.7)$$

Position reconstruction

Ecal clusters provide position information of comparable resolution to the SVT. Various weighting schemes for calculating a cluster centroid can be problematic due to periodic

patterns resulting from the segmentation of the crystals. The same weighting scheme, used by the CLAS IC algorithm, provided the optimal position resolution. The calculation of the position of the cluster is shown in Equation (5.2.8).

$$\begin{aligned} x_{cl} &= \frac{\sum_i w_i x_i}{\sum_i w_i} \\ y_{cl} &= \frac{\sum_i w_i y_i}{\sum_i w_i} \end{aligned}$$

In Equation (5.2.8), the index i indicates the individual module in the cluster, and w_i is described by Equation (5.2.8).

$$w_i = \max[0, w_0 + \ln \frac{E_i}{E_{rec}}] \quad (5.2.8)$$

The parameter w_0 in Equation (5.2.8) is an energy threshold such that $E_i/E_{cl} > e^{-w_0}$ and is found in simulation to have a value of 3.1 [2]. The logarithmic term enhances the contribution from the tails and improves the position measurement. There are additional effects to be considered when reconstructing the position at which a particle enters the Ecal that can be accounted for in simulation. These effects are the result of the different tracks that charged particles take in the magnetic field and are momentum dependent. The position correction for a generated 1 GeV electron is shown in Figure 5.2.6.

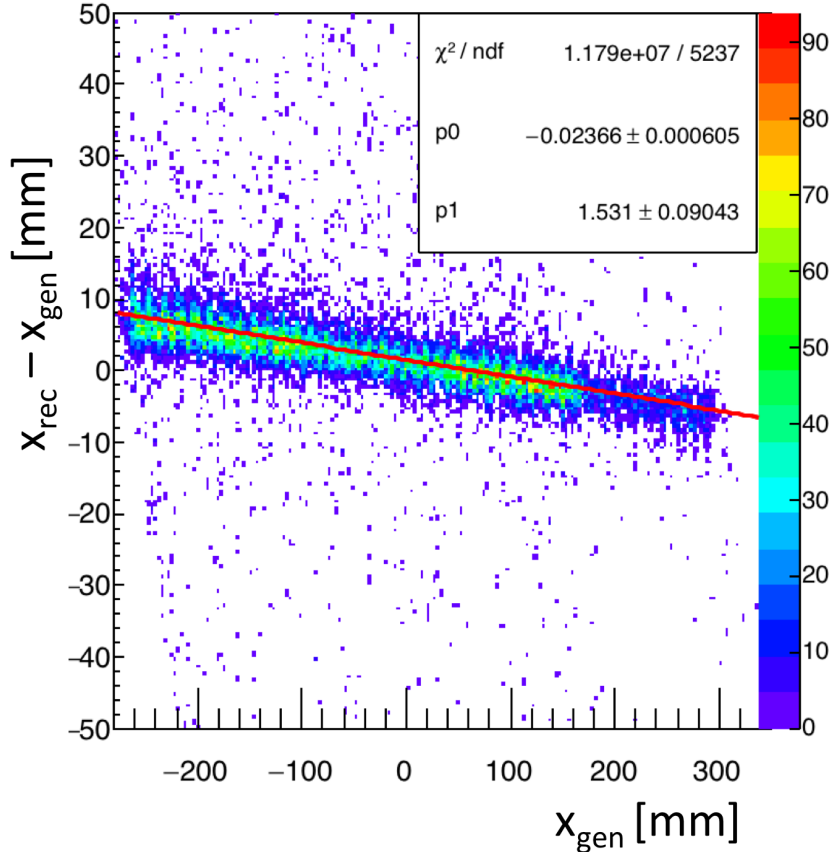


FIG. 5.2.6: The position correction as found for a 1 GeV electron is both energy and position dependent in order to account for the different angle of incidence at the Ecal.

The correction shown in Figure 5.2.6 is energy-dependent but is linear at fixed energy. The correction at each energy by particle-type is fit with Equation (5.2.9).

$$x_{rec} - x_{gen} = A(E_{rec})x_{gen} + B(E_{rec}) \quad (5.2.9)$$

The energy-dependence for the fit parameters $A(E_{rec})$ and $B(E_{rec})$ use the reconstructed cluster energy, not corrected for shower loss. These parameters for the electron horizontal position correction as a function of the reconstructed cluster energy are shown Figure 5.2.7.

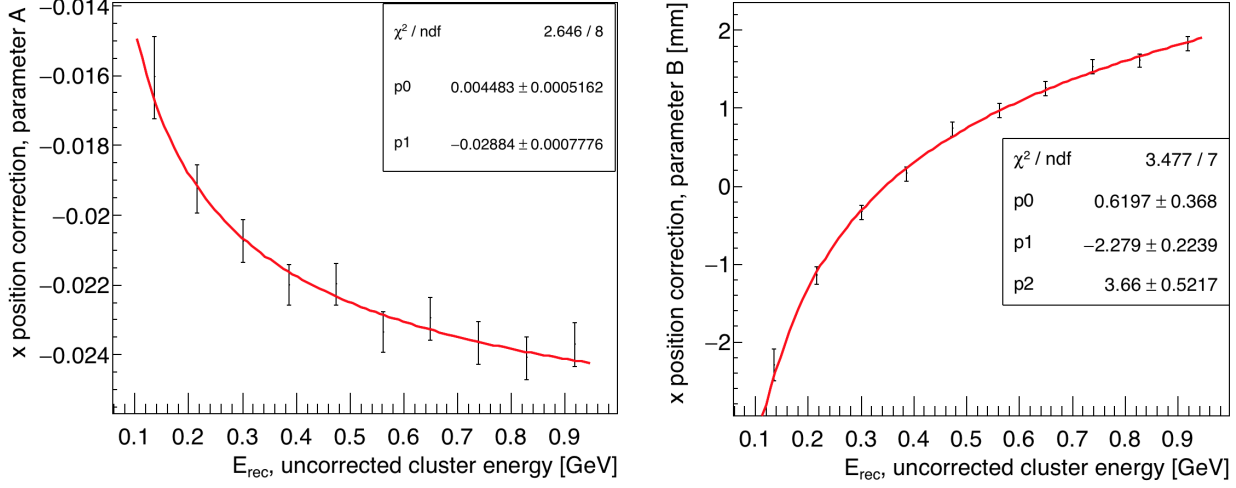


FIG. 5.2.7: The horizontal position correction parameters as functions of the uncorrected cluster energy.

The parameters in Figure 5.2.7 are fit to function form described in Equation (5.2.10).

$$A(E_{rec}) = \frac{p_0}{\sqrt{E_{rec}}} + p_1$$

$$B(E_{rec}) = p_0 \times E_{rec} + \frac{p_1}{\sqrt{E_{rec}}} + p_2$$

The corresponding correction values for all three particle types can be summarized in Table 3.

TABLE 3: Horizontal position corrections.

Particle	$A(E_{rec})$	$B(E_{rec})$
electron	$0.004483/\sqrt{E_{rec}} - 0.02884$	$0.6197E_{rec} - 2.279/\sqrt{E_{rec}} + 3.66$
positron	$0.006887/\sqrt{E_{rec}} - 0.03207$	$-0.8048E_{rec} + 0.9366/\sqrt{E_{rec}} + 2.628$
photon	$0.005385/\sqrt{E_{rec}} - 0.03562$	$-0.1948E_{rec} - 0.7991/\sqrt{E_{rec}} + 3.797$

Position corrections are not needed for the vertical cluster position because the magnetic field is not acting in this direction.

Position resolution

After applying the position corrections to each particle-type at the simulated energies, the residual between the measured and simulated position reconstruction is obtained. The

fitted residuals after correction for 1 GeV electrons are shown in Figure 5.2.8.

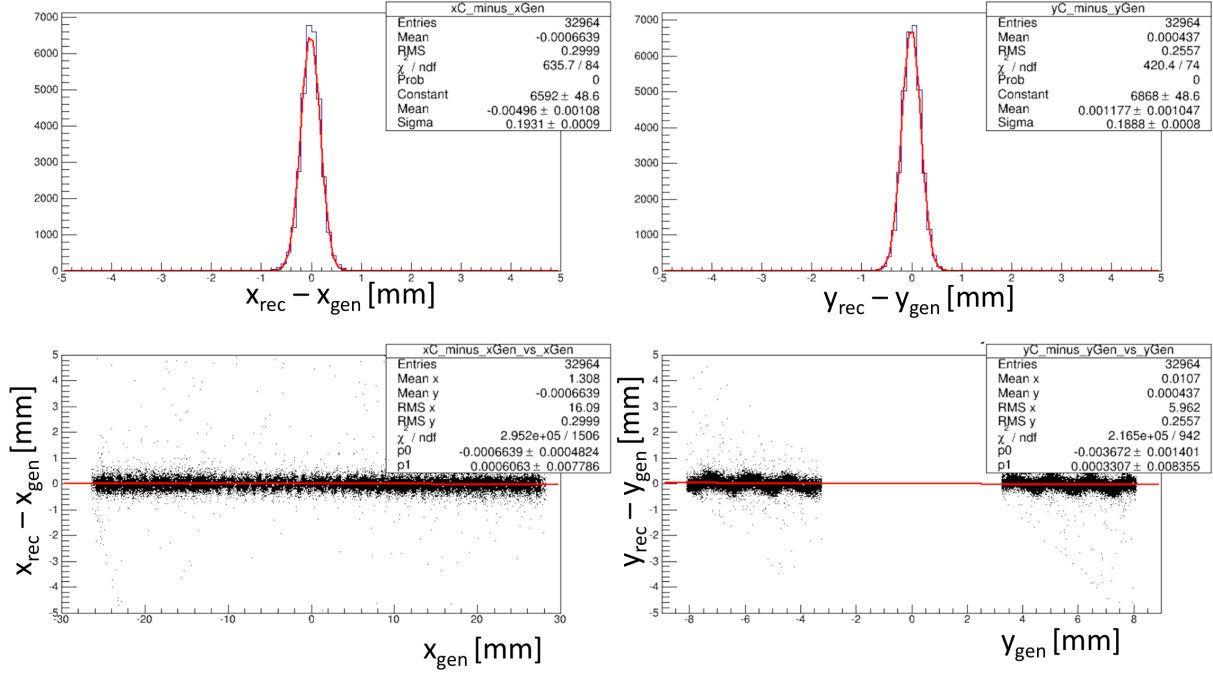


FIG. 5.2.8: The position resolution for 1 GeV electrons, after applying the horizontal position corrections.

As shown in Figure 5.2.8, no correction is required when reconstructing the vertical position of the cluster. The energy-dependent resolution of both the horizontal and vertical position of reconstructed clusters can be seen for electrons in Figure 5.2.9.

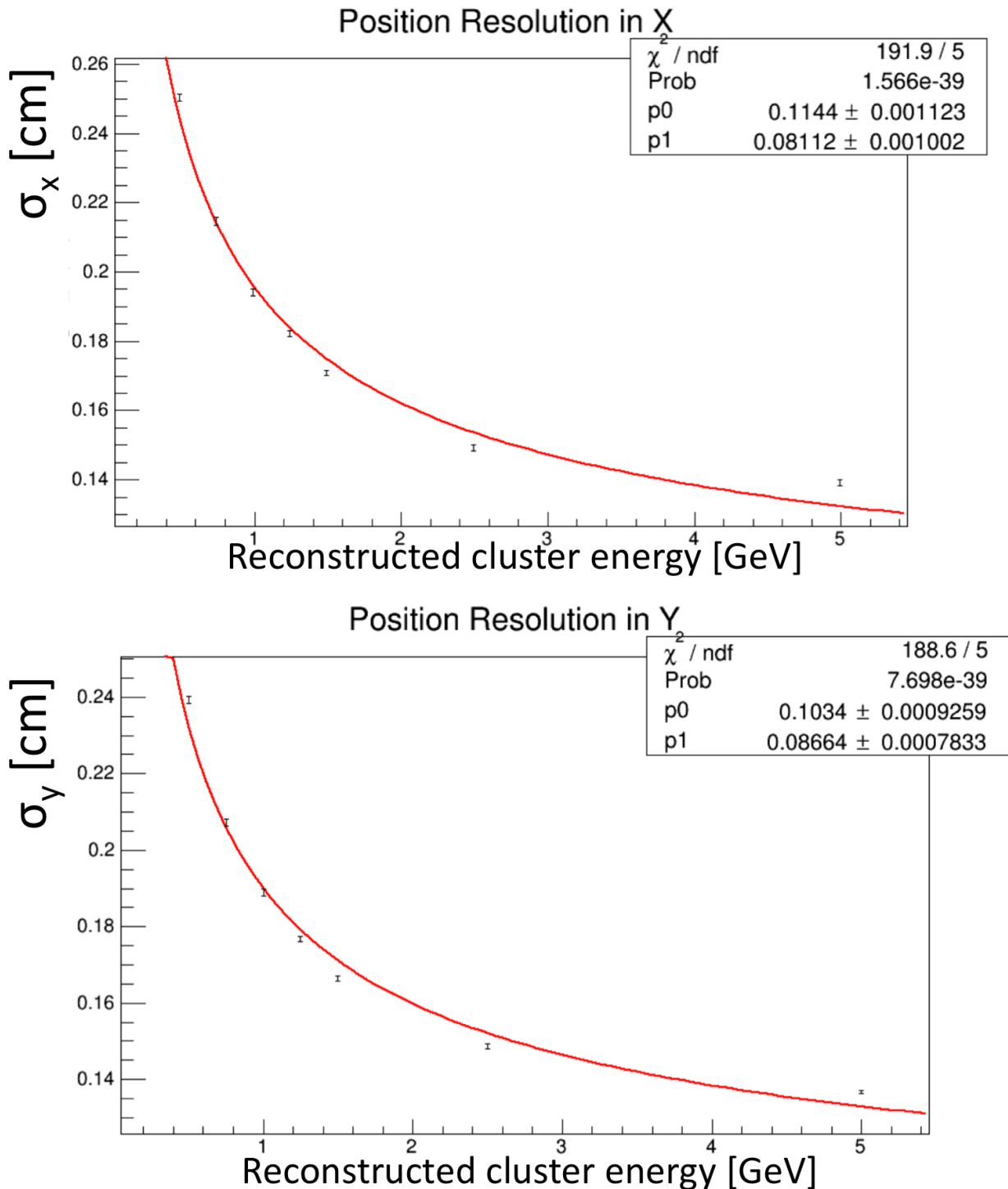


FIG. 5.2.9: The energy-dependence of the position resolution for electrons.

The position resolution is parameterized in terms energy following Equation (5.2.10).

$$\begin{aligned}\sigma_x &= \frac{p0}{\sqrt{E}} + p1 \\ \sigma_y &= \frac{p0}{\sqrt{E}} + p1\end{aligned}$$

The parameters $p0$ and $p1$ are different for the x and y resolutions and are found by fitting the residuals for the energies. The position resolution is better than 2 mm for 1 GeV electrons. As the Ecal face is located at approximately 1.4 m from the target, the Ecal can provide reliable position information when matched with a track. The position resolution for all particle types in the Ecal is summarized in Table 4.

TABLE 4: Position resolution.

Particle	σ_x [mm]	σ_y [mm]
electron	$0.1144/\sqrt{E_{rec}} + 0.08112$	$0.1034/\sqrt{E_{rec}} + 0.08664$
positron	$0.1268/\sqrt{E_{rec}} + 0.07711$	$0.1068/\sqrt{E_{rec}} + 0.08423$
photon	$0.1255/\sqrt{E_{rec}} + 0.08877$	$0.1005/\sqrt{E_{rec}} + 0.08867$

The full derivations for the position resolutions from simulation is described in more detail in Reference [2].

5.2.2 ECAL CALIBRATION USING COSMIC RAY ENERGY

The large area APDs enabled the Ecal to have the sensitivity to detect signals from cosmic muons traversing the Ecal crystals perpendicularly and then to use this signal for the initial calibration of the modules. The experimental setup was modeled using Monte Carlo simulations so that the energy deposited in the crystals from cosmic ray muons and rates could be studied. By measuring the average path length of cosmic ray muons in each crystal, the energy deposited in each crystal of the Ecal was calculated using the known energy deposition from 2 GeV muons [7].

The experimental setup for the cosmic calibrations utilized two scintillators placed below the Ecal to trigger readout of all of the crystals. A schematic for the setup of the cosmic calibration is shown in Fig. 5.2.10.

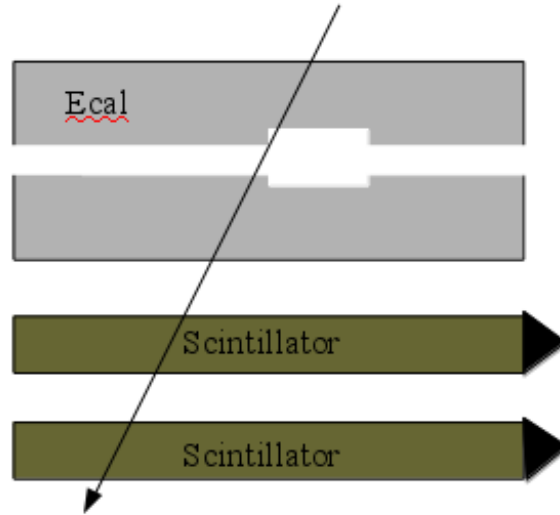


FIG. 5.2.10: Experimental setup for the cosmic ray calibration. As a cosmic ray passes vertically through both scintillators, event readout is triggered.

Each scintillator measures 75 cm long, 22 cm wide and 5 cm thick covering a slightly larger perpendicular area than the Ecal crystals. The two scintillators are less than half a meter apart with the closest scintillator less than half a meter beneath the Ecal. The energy deposited in each crystal in a layer is sensitive to the path length of the track as it passed through the crystal. Simulations show the average energy deposited in a crystal by a triggering vertical track in the scintillators in Fig. 5.2.11.

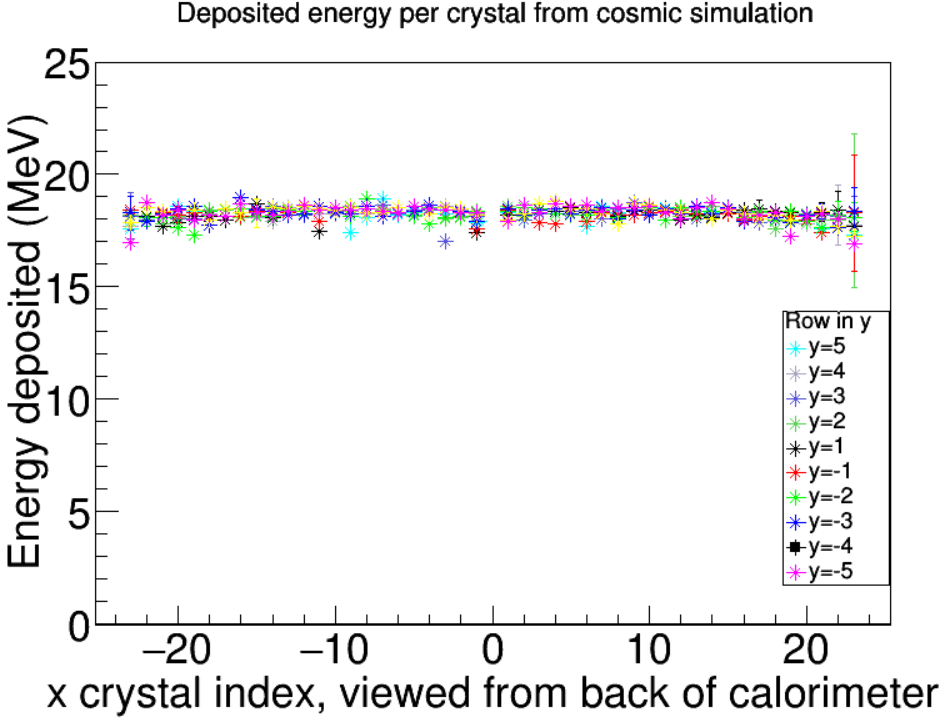


FIG. 5.2.11: The simulated cosmic ray muon energy deposition per crystal of the Ecal. The mean energy was 18.3 MeV.

In Fig. 5.2.11, only tracks passing through one crystal in a row were included. Additionally, the cosmic ray muon track had to pass through an adjacent crystal in the rows above and below a crystal. For crystals near edges, the geometrical requirement was adjusted to include the two crystals immediately above (or below for cases where the edge is above the crystal) the crystal being readout. The average energy deposited per crystal is approximately 18.3 MeV in agreement with the PDG.

In data, the raw FADC waveform for each crystal is readout, and the event is kept for further study after applying strict coincidence cuts between the two scintillators. The trigger rate for data is about 7 Hz. Only 30% of events passed the coincidence cut between the scintillators. For a track passing vertically through all ten layers, we can see the signal in each crystal as shown in Fig. 5.2.12.

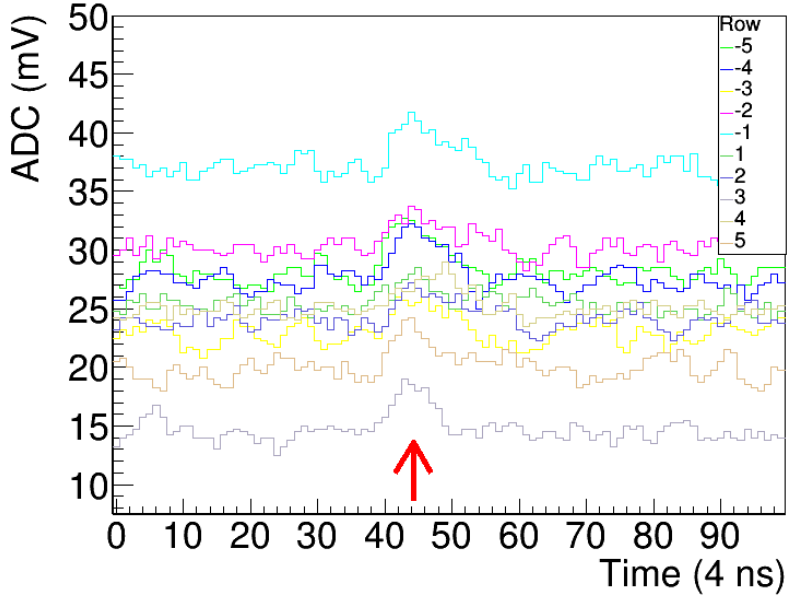


FIG. 5.2.12: Cosmic ray signal passing vertically through all ten layers of crystals in the Ecal. Each crystal’s signal is separated vertically in this plot by an offset (pedestal). The arrow indicates the approximate place in time that the cosmic signal passed through the detector.

As seen in Fig. 5.2.12, each FADC channel has a unique pedestal value. The pedestal for each event was calculated as an average of the first twenty bins of the time window. The integrated signal was used for the final calibration. By searching for a threshold crossing in the time window where cosmic events occurred, the signal was then fully integrated and the pedestal was subtracted. The raw waveform thresholds were 2.5 mV in 2015 and increased to 3.5 mV in 2016 to accommodate the larger signals after the removal of the splitters. Geometric cuts are then applied to the data in offline analysis. Crystals having peaks over a certain threshold must have at least an adjacent crystals located above and below with threshold crossing, but the crystals to the left and right must not cross threshold. These cuts ensure that the track passed as vertically as possible through the Ecal (reducing the variations in path length across each crystal). The integrated signals over many events in each crystal were fit. An individual crystal fit is shown in Fig. 5.2.13.

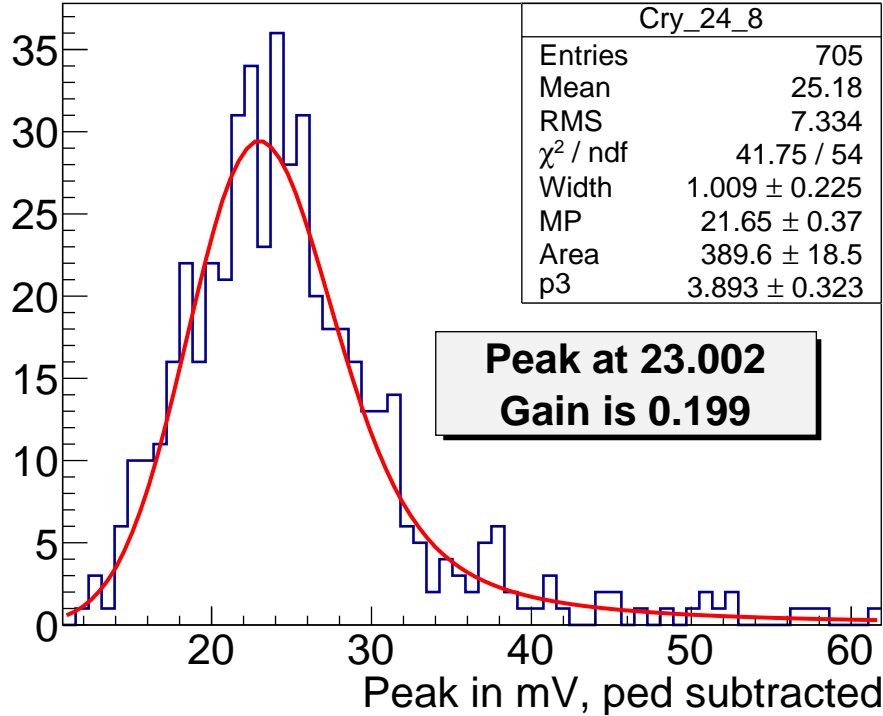


FIG. 5.2.13: Each cosmic signal was integrated and then fit using a Landau-Gaussian convolution function. The peak was calculated numerically from this fit.

The fit shown in Fig. 5.2.13 utilized a Landau-Gaussian convolution as the Landau part corresponds to the crystal's response to a particle's energy deposition as ionization energy loss, and the Gaussian part accounts for the statistical nature of the electronics shaping and readout. The peak of the fit is calculated numerically, and the initial conversion from units of FADC to energy (MeV) is obtained (called the Gain factor). The unit conversion from units mV to FADC is 1 V to 4096 FADC. The 4096 FADC counts can be set to 1 V or 2 V, but for 2015 and 2016 running, the setting was 1 V. This arises from the 12 bit conversion which yields 4095 FADC. Using the peak position for crystal in units of FADC, and by knowing the energy deposition of cosmic ray muons from simulation, the gain factor is calculated as shown in Eqn. (5.2.10).

$$\text{Gain} = \frac{[\text{MeV}]}{[\text{FADC}]} \quad (5.2.10)$$

After approximately 60 hours of cosmic data, the entire Ecal could be calibrated using cosmics, and the resultant gains for all channels in 2015 is shown shown in Fig. 5.2.14 and Fig. 5.2.15.

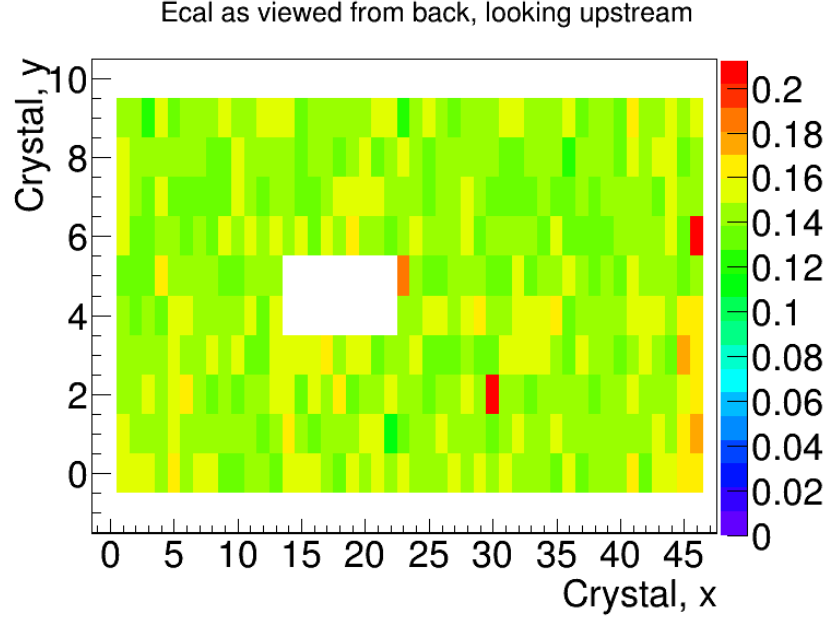


FIG. 5.2.14: Resulting gain calibration using cosmics for 2015 running (before splitter removal).

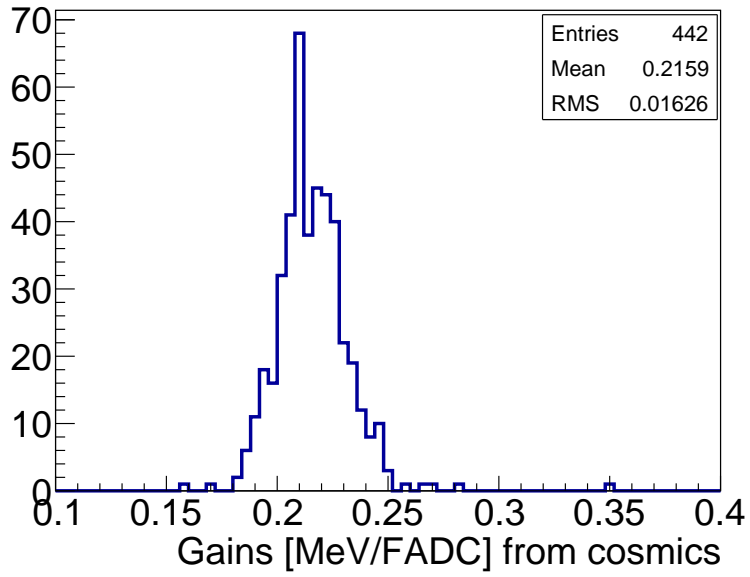


FIG. 5.2.15: Resulting gain calibration using cosmics for 2015 running (before splitter removal).

With the splitters installed the Ecal readout chain, the average gain value was around

0.2 MeV/FADC in 2015. After the removal of the splitters in January 2016, prior to the 2016 Physics Run, the average gains as found by cosmics were around 0.13 MeV/FADC.

5.2.3 ECAL HIT PULSE FITTING

All data was taken using the FADC250 modules which sample at 250 MHz, or every 4 ns. While the firmware has various modes capable of recording data, size was not an issue and Mode 1 was used for all 2015 and 2016 running. Mode 1 is advantageous because the full measured waveform for a module hit is preserved and all methods for extracting the energy and time information from a hit can be done in offline analysis. The trigger decision to readout a module is based off a leading edge threshold which was set to 12 FADC units in 2015.

The full readout response for each module was carefully studied in order to understand the time response and shaping effects of the preamplifier on the Ecal modules [8]. It was found that the raw waveform response was best described by the sum of the pedestal P and a 3-pole function for the pulse with width τ and occurring at time t_0 as shown in Eq. (5.2.11) [8].

$$P + \frac{A}{2\tau^3}(t - t_0)^2 e^{-(t-t_0)/\tau} \quad (5.2.11)$$

The pulse integral value is parameter A . When $t < t_0$, the pulse amplitude is zero. The best resolutions were found by fixing the width parameter for each module as an average of width module as measured over several pulses. An example fit is shown in Fig. 5.2.16.

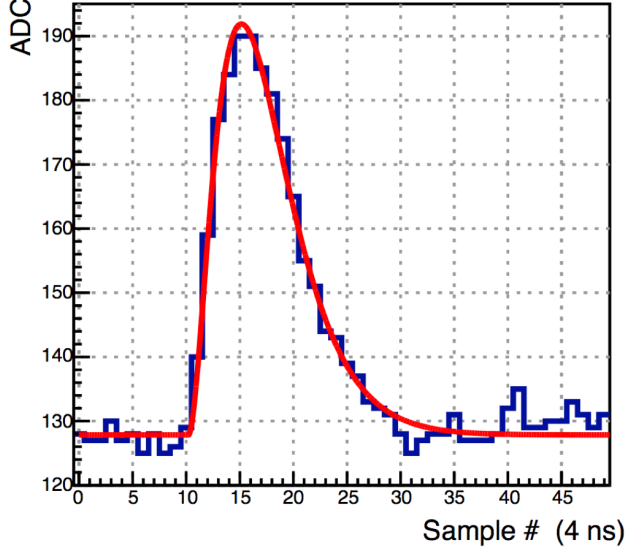


FIG. 5.2.16: Example fit to a real Ecal module pulse.

The pedestal is calculated event-by-event initialized by a running average over the previous fits for the pulse. The fit range was set to 20 ns before threshold crossing and 60 ns after in order to eliminate pulls from pile-up signals in the same event [9]. The pulse-fitting of the wave waveform demonstrated the best time resolution and energy resolution when compared to the other hardware integral methods that could have been implemented [9].

5.2.4 CALIBRATION USING ELASTICALLY-SCATTERED ELECTRONS

The calibration using cosmic ray muons was sufficient for initial data-taking with the electron beam, but the overall energy calibration of the Ecal is optimal using incident particles of the highest energy. With electron beam on target, the Ecal detects electrons from elastic scattering at the target that peak, after correction for shower leakage effects, at the beam energy. As the target is off centerline beam right, there are geometric effects that prevent elastically-scattered beam energy electrons from full coverage of the Ecal. From simulation, the first column of crystals on beam right, and the five columns of crystals on beam left cannot be calibrated using elastically-scattered electrons.

To calibrate the ecal using elastically-scattered electrons, we selected events where the seed hit crystal carried at least 60% of the overall cluster energy. The seed hit was also required to have carried greater than 450 MeV in the 2015 data (1.1 GeV for the 2016 dataset), to have triggered a Singles-1 event readout from the DAQ, and to have occurred in the optimal trigger timing window. The cluster energy was associated with the seed hit module

for the calibration. The calibration uses an iterative procedure, by which the reconstructed peak energy is matched to that found by simulation (prior to shower corrections). For each peak, an iteration coefficient is found that reflects the ratio of the peak position measured in Monte Carlo to the peak position found for a particular iteration in the data. This ratio can be seen in Equation (5.2.12).

$$C_i = \frac{MC_{peak}}{data_{peak}} \quad (5.2.12)$$

After each iteration, this ratio C_i is applied to the original gain coefficient as well as any coefficient found from previous iteration. The data is re-processed applying these changes to the gains and clustering is re-run. This procedure continues until the coefficients found in a particular iteration are all less than 1 %. Crystals on the edge of acceptance with poorly resolved peaks were given an iteration coefficient of 1. After completion of the calibration (approximately 2-3 iterations), the shower loss correction as found in simulation was applied to the reconstructed cluster energies. The final peak position for elastically-scattered electron clusters in the fiducial region of the Ecal (where seed hits are not on edge crystals or at the edge of the acceptance for detecting elastically-scattered electrons) is shown in Figure

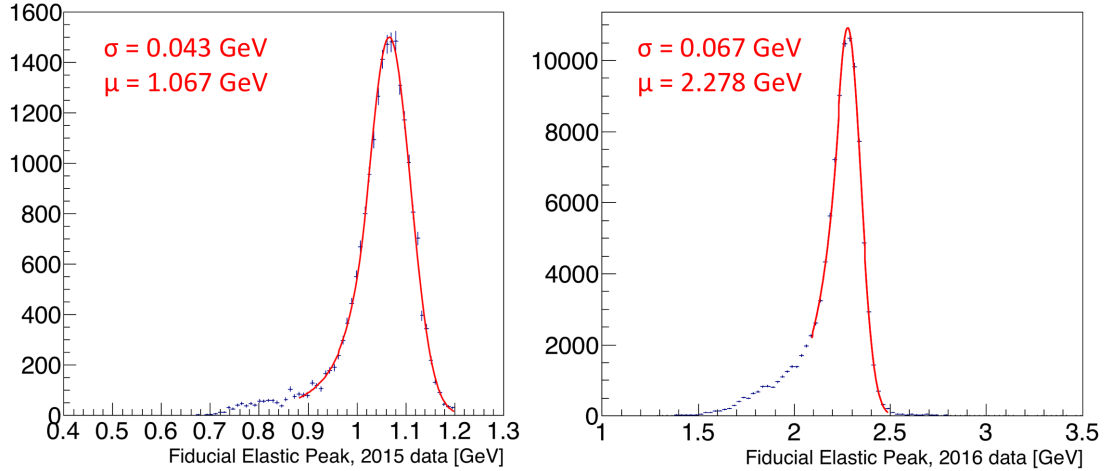


FIG. 5.2.17: Shown are the resultant fiducial peaks for the 2015 and 2016 runs on the left and right, respectively. The peaks are fit with a Crystal Ball function and the peak position and widths are indicated.

As shown in Figure 5.2.17, the energy resolution improves with the beam energy. The

cluster energy spectrum is fit with a Crystal Ball function which contains a Gaussian component and a power law low energy tail. The Ecal has an energy resolution of approximately 4% in the fiducial region at approximately 1 GeV and 2.9% at 2.3 GeV.

The final gains obtained after calibration with elastically-scattered electrons were compared to the gains obtained with cosmics alone in order to check for systematic offsets. While no systematic offsets were found with respect to the cosmic energy calibration, the comparison between the low and high energy calibrations can tell us that the initial energies used for the cosmic calibration are roughly accurate, but it is limited in telling us anything about the linearity of the gain between these two energies. If there was found to be any systematic offsets, these should be applied to the gains of the crystals that could not be calibrated using the elastically-scattered electrons due to acceptance, and the effects on the triggered data would need to be quantified.

5.2.5 WIDE ANGLE BREMSSTRAHLUNG FOR STUDIES OF EDGE EFFECTS

The primary physics trigger looks for two cluster events and recorded a high yield of WAB particles composed of a final state electron and photon. The spectrum of cluster energies in the 2015 dataset shows an excess of WAB events occurring along the black diagonal line where the energy sum of the two particles is approximately equal to the uncorrected beam energy.

Initial studies after the calibration using elastic electrons showed that the energy sum of two particles in exclusive events having mid-range energies was lower than the reconstructed elastic energy, indicating that the shower loss corrections in the mid-range beam energy required further study. WAB events were used to refine the shower loss corrections for mid-range energy particles. WAB events are identified by have track-matched clusters and no track matching a photon cluster. The reconstructed energy sum of of the two particles must be equivalent the beam energy as shown in Equation (5.2.13).

$$E_i = \frac{E_{e-}}{f_{e-}(E_{e-})} + \frac{E_\gamma}{f_\gamma(E_\gamma)} \quad (5.2.13)$$

In Equations (5.2.13) and (5.2.15), f refers to the shower loss correction described by Equation (5.2.2). The underlying assumption is that the relationship between the electron and photon shower loss corrections found in Monte Carlo are preserved according to Equation (5.2.14).

$$\frac{f_{e-,data}(E_{e-})}{f_{\gamma,data}(E_{\gamma})} = \frac{f_{e-,MC}(E_{e-})}{f_{\gamma,MC}(E_{\gamma})} \quad (5.2.14)$$

In maintaining the relationships shown in Equations (5.2.13) and (5.2.14), a chi-squared minimization yields the optimal adjustments to the shower loss correction functions for mid-range energy particles as shown in Equation (5.2.15).

$$\chi^2 = \sum_i \frac{(E_{beam} - E_i)^2}{\sigma_{e-}^2(E_{e-}) + \sigma_{\gamma}^2(E_{\gamma})} \quad (5.2.15)$$

For each event, the energy sum of the two corrected clusters, E_i , is calculated as described by Equation (5.2.15). The end result is a small correction to the shower loss correction functions that ranges from less than 2% at cluster energies below 400 MeV and less than 1% above 400 MeV. After incorporating these updated corrections to the shower loss correction functions, the energy resolution can be extracted for all energies and positions in the Ecal.

5.2.6 ENERGY RESOLUTION IN DATA

The elastically-scattered electrons provided the clearest point in extracting the energy resolution of the Ecal at the beam energy. Using WAB particles, electrons and photons, the energy resolution of the Ecal was fully characterized in terms of energy and position relative to the edges.

To study the energy resolution in the fiducial region of the Ecal, all electrons were matched to tracks, and the track position extrapolated to the incident face of the Ecal was used to determine the electron's vertical distance relative to the beam gap edge. For elastically-scattered electrons, one track-matched electron is used. For WAB electrons, the photon cluster was required to be at least 10 mm from the Ecal edges as this way, the reconstructed photon energy is reliable. By selecting WAB events where the energy difference between the two particles is less than 100 MeV, the resolution of the energy sum peak was fitted to extract the resolution. The resolution was extracted according to Equation (5.2.16).

$$\sigma_{E_{\gamma}+E_{e-}}^2 = \sigma_{e-}^2(E_{e-}) + \sigma_{\gamma}^2(E_{\gamma}) \quad (5.2.16)$$

When both particles are in the fiducial region and are roughly equal in energy, then the energy resolution of the sum could be divided by $\sqrt{2}$ assuming that the energy resolution of both particles is the same. This same procedure was used to study the resolution when the particle energies were more asymmetric in energy in order to obtain the single particle energy resolution at various energies.

The experimentally-obtained fiducial energy resolution agrees well with Monte Carlo but generally yields a slightly larger energy resolution across all energies (on the order of about 15%). The energy resolution obtained in data is shown in Figure 5.2.18.

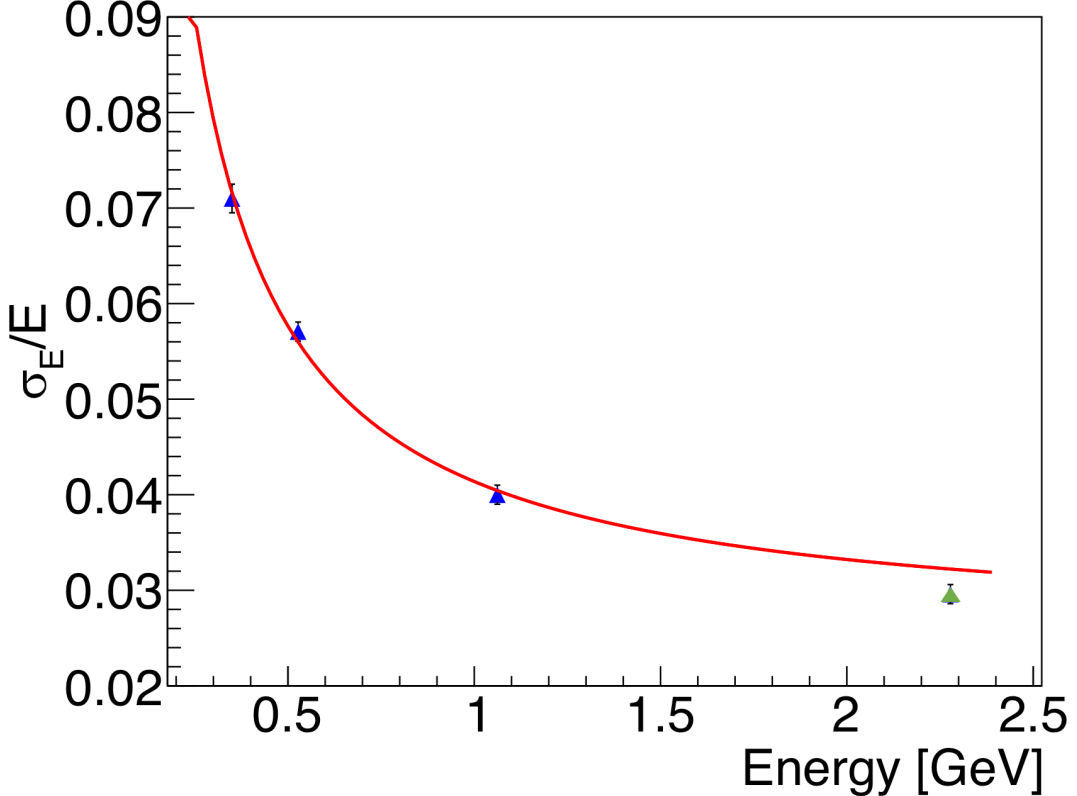


FIG. 5.2.18: The blue points are derived from the 2015 running for the energy resolution of a single particle. The green point at approximately 2.3 GeV was determined from the elastic calibration of the 2016 data. The fitted energy resolution was determined from the 2015 data only, but it is shown here extrapolated to the 2016 energy.

The fit to the energy resolution in data is shown in Equation (5.2.17) and is fit to the blue points representative of the 2015 data in Figure 5.2.18.

$$\frac{\sigma_E}{E}(\%) = \frac{1.62}{E} \bigoplus \frac{2.87}{\sqrt{E}} \bigoplus 2.5 \quad (5.2.17)$$

The first term in Equation (5.2.17) is generally attributed to the noise from the pre-amplifiers and is roughly consistent to that found in Monte Carlo. The second term is related to the statistical fluctuations of the shower containment and the APD gain. This term is larger than the term found in Monte Carlo but is still roughly consistent. The third

term contains both the energy leakage out the back of the Ecal as well as the crystal-to-crystal inter-calibration error. This term is significantly higher than that derived in Monte Carlo, but is much closer to the term as found in data for the CLAS Inner Calorimeter. It's possible that this term is affected by the inability to calibrate several crystals along the outer edges of the calorimeter with elastics.

The energy resolution as found in 2016 at 2.3 GeV (shown in green on Figure 5.2.18) is slightly better than that predicted by the fit to the 2015 points. It is likely that the energy resolution of the Ecal improved overall in 2016 as compared to 2015 because the TDCs were removed, and the signal going into the FADCs was no longer split.

5.2.7 TIMING CALIBRATION AND PERFORMANCE

The time obtained from the raw fitting of the waveform still requires further corrections in order to account for various crystal-to-crystal time offsets that can result due to time walk and differences in hardware (such as cable lengths). The overall time offset for each crystal can be corrected using the accelerator RF signal, and the time walk can be removed through careful study of hits and hit energies in a cluster versus that of the seed hit energy. The corrected individual crystal time is shown in Equation (5.2.18).

$$t = t_0 + \Delta t_{RF} + \Delta t_w(E) \quad (5.2.18)$$

In Equation (5.2.18), t_0 is the time calculated from fit to the raw ADC distribution of a crystal, Δt_{RF} is the hit time offset with the accelerator RF signal and $\Delta t_w(E)$ is the energy-dependent time-walk correction. The accelerator has a an intrinsic frequency of 499 MHz and the RF signal is sampled every 80 signals into Hall B. The RF signal is split in the hall and readout by two FADC250 channels. The raw waveform of the RF signal is shown in Figure 5.2.19.

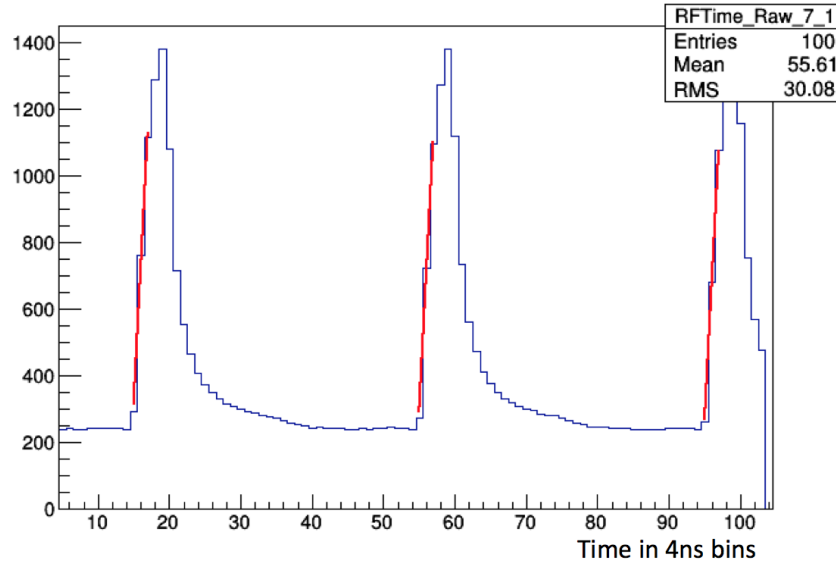


FIG. 5.2.19: The raw distribution of the RF signal as read in by the HPS FADC is shown with a straight line fit to the leading edge of the signal.

The strategy to read off the time from the RF signal was chosen in order to minimize the measured intrinsic resolution of the FADC modules. After identifying the peak bin (4 ns per bin), the pedestal was calculated by averaging the values in 4 bins occurring at 6 to 9 bins prior to the peak. The threshold used in selecting the fitting points was found by calculating the 1/3 height between the averaged pedestal and the peak. The points for the straight line fit were then chosen as the last point below this threshold and the next two points above the threshold. These points were chosen due to the linear uniformity of the pulse away from the peak bin. The time that was used from this fit was at the half height between the pedestal and the peak. This combination of parameters minimized the width of the time difference distribution between the RF signals in the two FADC channels as shown in Figure 5.2.20.

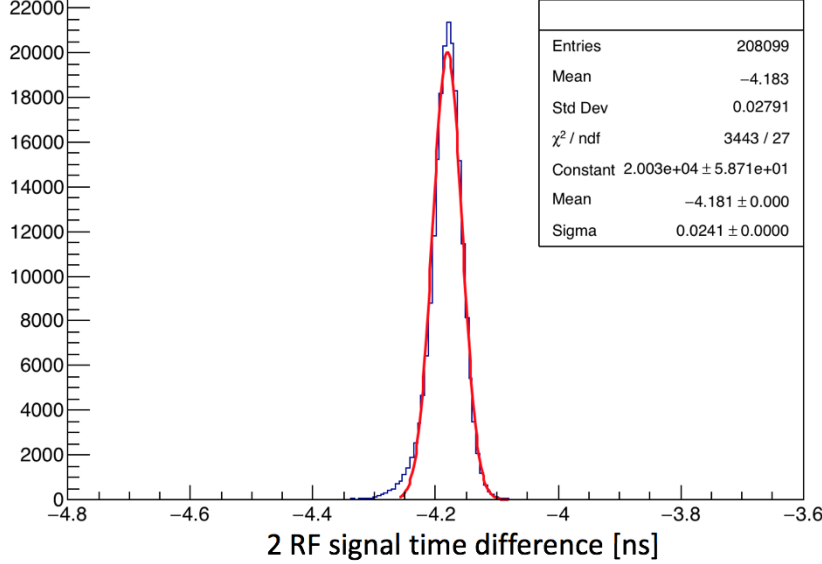


FIG. 5.2.20: The intrinsic time resolution of the FADC modules can be obtained by the width of the two RF signal time difference to be approximately 24 ps.

The internal time resolution of the FADC modules was measured to be approximately 24 ps from the width of the time difference between the two RF signals.

The individual crystal module time offsets are measured with respect to the accelerator RF time. For time offsets less than 2 ns, or the time between electron bunches from the accelerator, we calculate the fine time offset per crystal as shown in Equation (5.2.19).

$$\Delta t_{fine} = \text{modulo}(t_0 - t_{RF} + N \times 2.004, 2.004) - 1.002\text{ns} \quad (5.2.19)$$

In Equation (5.2.19), t_0 is the time for the crystal as reported from pulse-fitting, t_{RF} is the reported RF time, and N is an arbitrarily large integer to shift the distribution to all positive values. 2.004 pertains to 499 MHz accelerator RF frequency. Before applying Equation (5.2.19), we observe the beam bunch structure in the time difference between the crystal hits and the RF time in Figure 5.2.21.

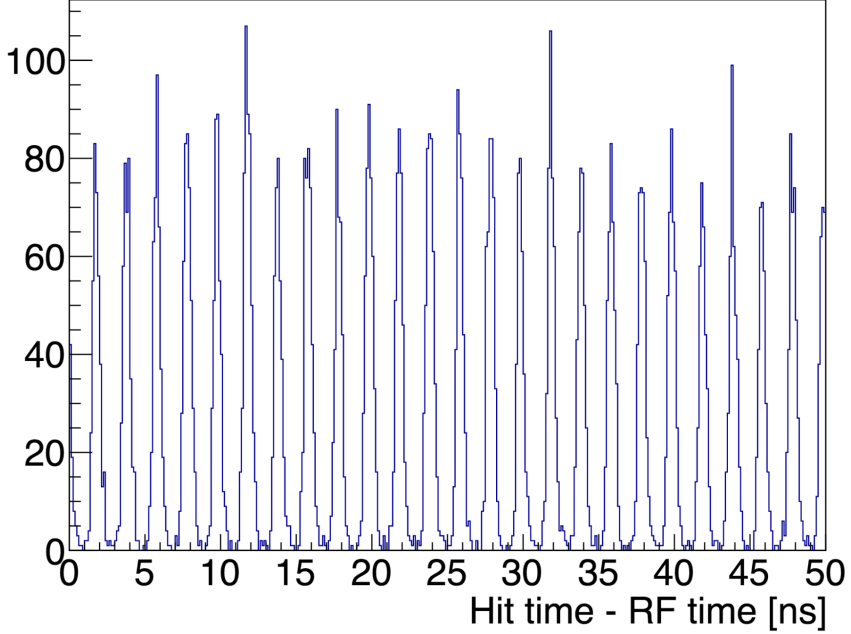


FIG. 5.2.21: From the time difference between Ecal hits and the RF time, electron beam bunch structure is seen to occur at approximately 2 ns, consistent with known accelerator RF.

By applying Equation (5.2.19) to Figure 5.2.21, we can align all of the signals and see the fine offset of each module with respect to the RF time. This technique only shows the offsets less than 2 ns and results in all crystals being aligned to the nearest $2n$ ns, where n is any integer.

To fully align the crystals, we choose a crystal to align with RF signal at 0, and then align all other crystals with respect to this crystal. Because the primary trigger for HPS is a cluster pairs trigger, we can compare the time difference between clusters to make this correction. The time of the highest energy hit in a cluster was used to set the time for the cluster. Comparison studies to check if an energy-weighted distribution using all hits in a cluster could provide a better estimate of the cluster time were conducted, but these calculations found no significant difference due to the seed hit energy dominating the time distribution and producing the same results as if one had used the time from the seed hit only. Well-correlated pairs of clusters were selected by looking for pairs with an energy sum equal to the beam energy and an energy difference of less than 200 MeV. The times for both clusters must have occurred in the 30-70 ns time window for the 2015 run which was the optimal time window for triggered events. The time difference correction between two pairs of clusters after the fine time offset correction is shown in Figure 5.2.22.

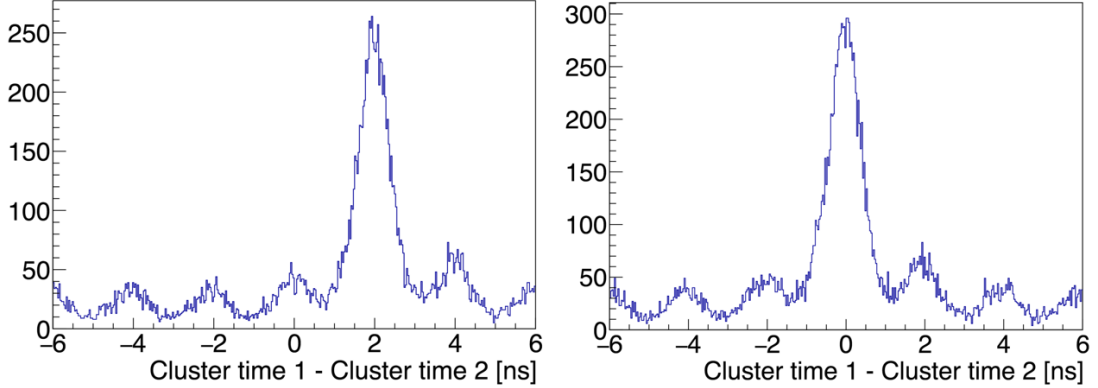


FIG. 5.2.22: After correcting all clusters with the fine timing offset correction, clusters are aligned to the nearest 2 ns time offset with respect to the RF signal. Shown on the left is a cluster pair that has an overall 2 ns time difference that needs to be accounted for in the final offset with the RF time. The plot on the right shows a different cluster pair with an offset centered at 0.

In Figure 5.2.22, a large 2 ns offset between a cluster pair is seen on the left prior to this step in the timing correction with respect to the RF signal. A different cluster pair, shown on the right, is seen to have no overall time offset that needs to be accounted for with respect to the RF time.

After correcting for the time offsets of all crystals with respect to the RF time, an energy-dependent correction, known as the time walk correction, must be accounted for. Time walk is the time difference of a signal crossing threshold in an ADC due to the finite rise time of the leading edge and the difference in signal amplitudes for particles of different energies. The effect causes particles of lower energy to cross the threshold later in time than particles of higher energy. This effect is not physical and can be removed by studying the time difference between hits in a cluster versus the seed hit as a function of the hit energy. Pulse fitting of the raw signal removes most of the time walk when compared to other methods that can be used to obtain a hit time. In the 2015 data, the seed hit was greater than 400 MeV and provided a reasonable threshold against which to compare hit times at lower energies. For the 2016 data, because there were high energies available, the time walk correction was able to use a much higher seed hit threshold of 1 GeV, and the energy-dependence could be extended to higher energies. The time walk can be extracted from the comparison of the hit times within a cluster as shown in Figure 5.2.23.

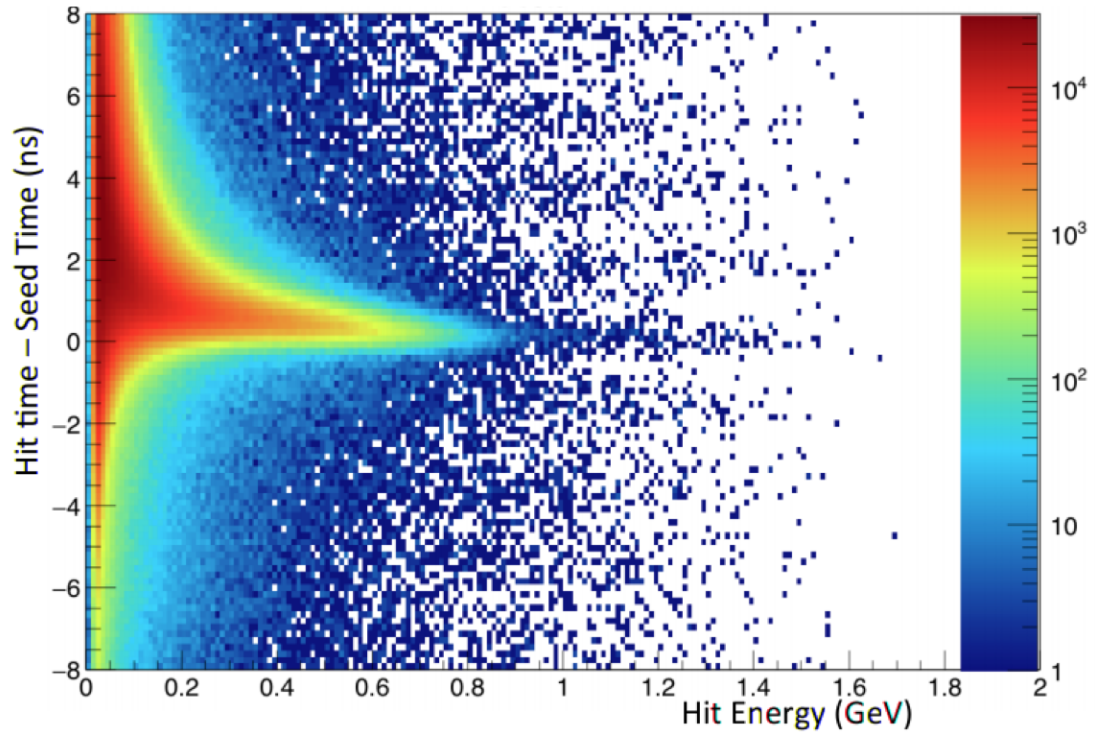


FIG. 5.2.23: The time walk correction for the 2016 data can be extracted from the difference of hit times in a cluster versus the seed hit time as a function of the the hit energy.

The time walk correction as found for the 2016 data is shown in Figure 5.2.24.

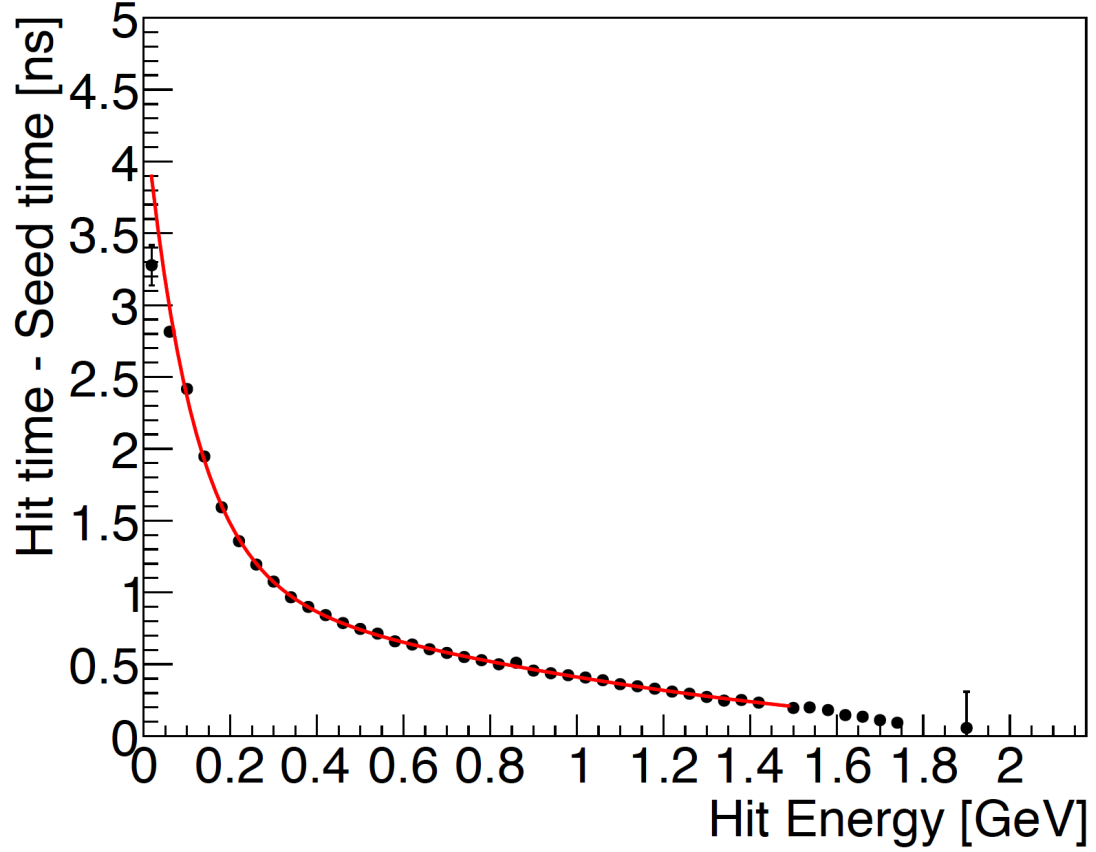


FIG. 5.2.24: The time walk correction for the 2016 data was found by comparing the time difference between hits in a cluster versus the seed hit time.

The time walk shown in Figure 5.2.24 is described by the form in Equation (5.2.21).

$$\Delta_{t_{walk}} = e(p_0 + p_1 E) + p_2 + p_3 E + p_4 E^2 \quad (5.2.20)$$

After removing all crystal-to-crystal time offsets and applying the energy-dependent time walk correction to all modules, the resulting time resolution for all energies can be obtained as shown in Figure 5.2.25.

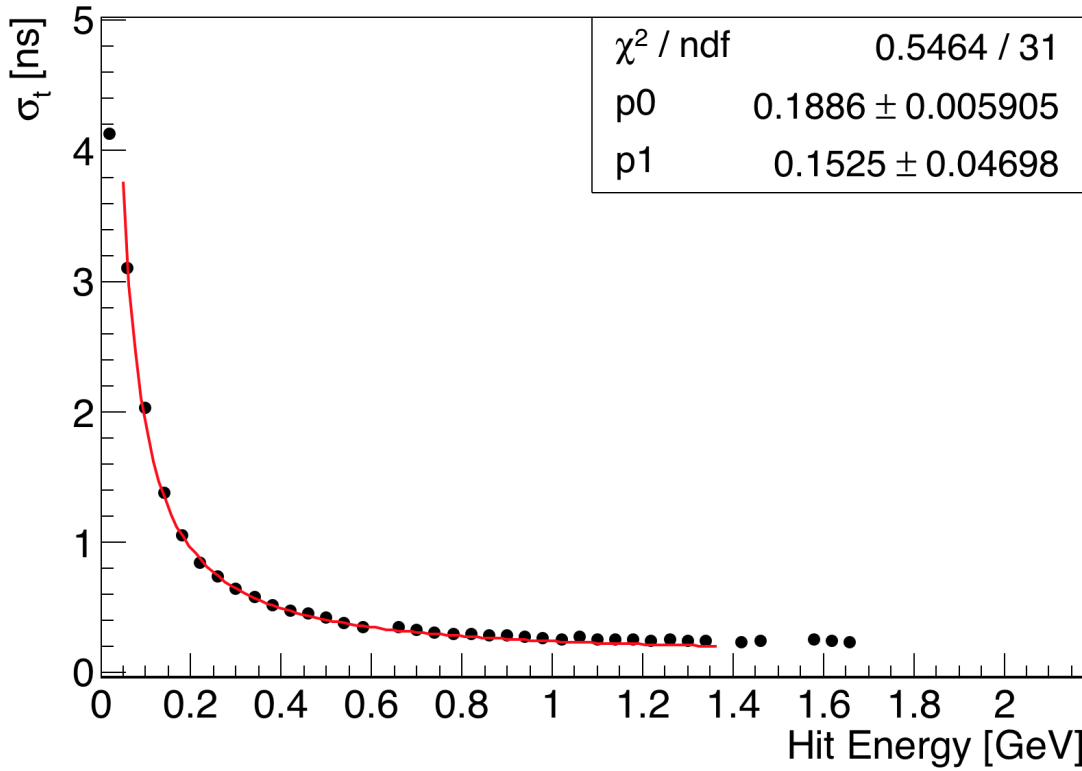


FIG. 5.2.25: The time resolution as a function of energy is shown.

The time resolution as a function of hit energy shown in Figure 5.2.25 is characterized by Equation

$$\sigma_t [\text{ns}] = \frac{p_0}{E} \bigoplus p_1 \quad (5.2.21)$$

The measured time resolution for the time difference for two clusters is shown in Figure 5.2.26.

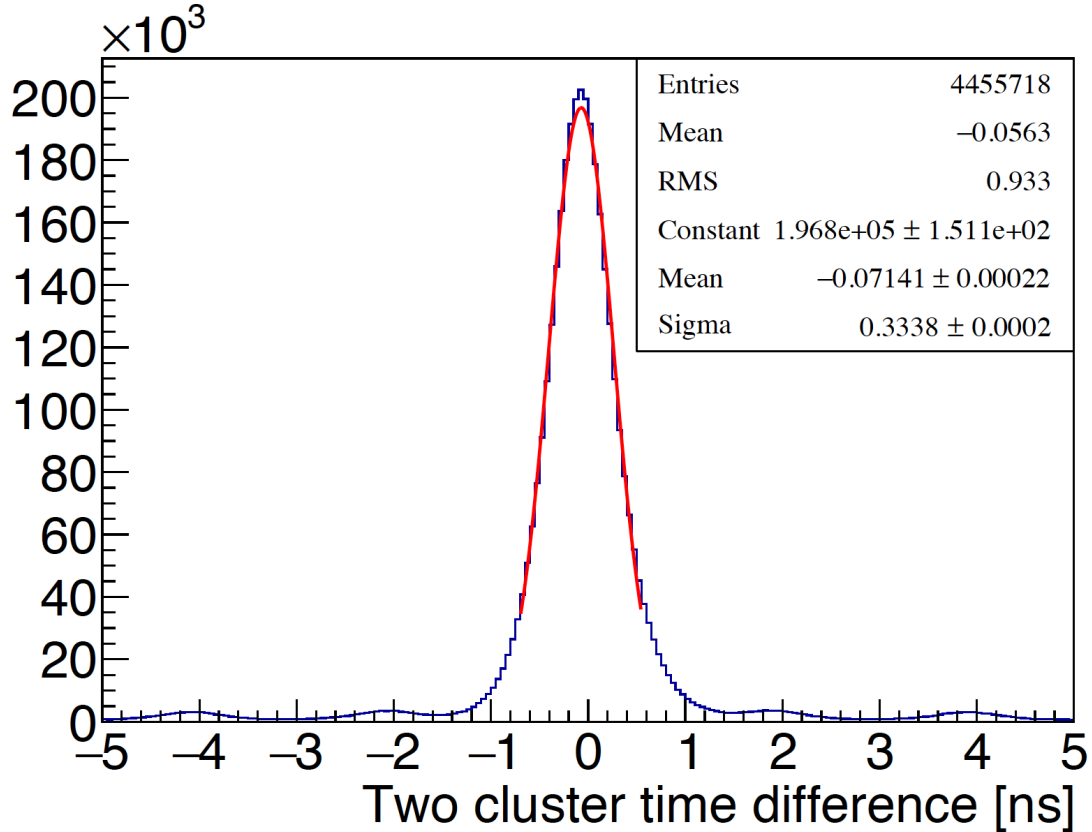


FIG. 5.2.26: The time difference between two clusters is shown. The energies sum to greater than 80% of the beam energy and has a resolution of approximately 330 ps .

As shown in Figure 5.2.26, for two clusters that have an energy sum greater than 80% the beam energy in 2016, the resolution is approximately 330 ps. For the 2015 running at a lower beam energy, the resolution of the time difference between two clusters was found to be approximately 470 ps. This difference between the 2015 and 2016 two cluster time resolution is primarily due to the difference in the time walk at the energies that dominate the two clusters chosen.

CHAPTER 6

SEARCHING FOR DISPLACED VERTICES

6.1 MONTE CARLO SIMULATION

6.1.1 RADIATIVE FRACTION

Background events can be produced from QED trident processes and wide-angle bremsstrahlung (WAB). The trident processes can be separated into "radiative" and "Bethe-Heitler" diagrams. In particular, the heavy photon production is related to the radiative trident cross section. The A' production for a mass bin is described as shown in Equation (6.1.1).

$$\frac{d\sigma(A' \rightarrow e + e^-)}{d\sigma(\gamma^* \rightarrow e + e^-)} = \left(\frac{3\pi\epsilon^2}{2N_{eff}\alpha} \right) \left(\frac{m_{A'}}{\delta m_{A'}} \right) \quad (6.1.1)$$

In Equation (6.1.1), N_{eff} , the number of available decay states, is one for the HPS experiment which explores a mass range in which the heavy photon can only decay to one Standard Model final state ($e + e^-$). The ϵ^2 refers to the coupling factor between the heavy photon and the Standard Model while the α is the fine structure constant. The $\frac{m_{A'}}{\delta m_{A'}}$ refers to the central mass value considered in the mass bin of study. The fraction of radiative reactions amongst trident events in the HPS search region is the radiative fraction. Using MadGraph5 Monte Carlo to model the tridents and radiatives and MadGraph4 Monte Carlo to model the wide angle bremsstrahlung (WAB) background, the radiative fraction can be determined as shown in Figure 6.1.1.

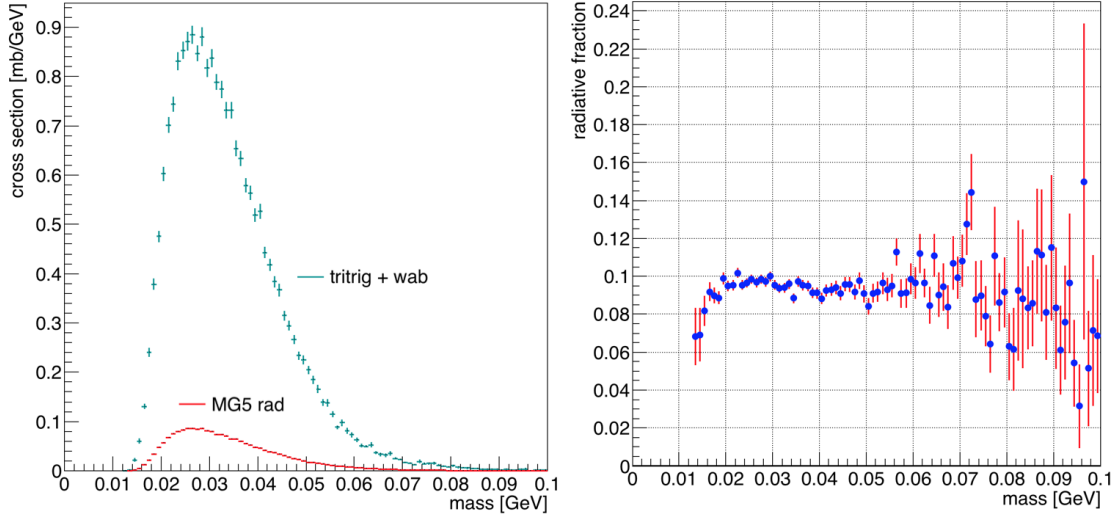


FIG. 6.1.1: Radiative fraction using MadGraph5 Monte Carlo and spinfix WAB.

As shown in Figure 6.1.1, the radiative fraction relevant to the vertex analysis is approximately 9.5% for all masses. This fraction is defined as the ratio of radiative events to the background events (tritrig+WAB in Figure 6.1.1) and is the same for both the 0.5 mm and 1.5 mm data sets.

6.1.2 VERTEX RECONSTRUCTION EFFICIENCIES

The events relevant to the vertex analysis were triggered using the pairs-1 HPS trigger cuts. The data is loosely selected as pairs that have a cluster in the top and bottom of the Ecal. A radiative cut, a cut on the measured sum of the energy of the two reconstructed particles in order to select A' events of interest, is chosen to be greater than 80% of the beam energy. Tracks are reconstructed using various methods and a Generalized Broken Lines (GBL) track re-fit is performed using a minimum of five hits in a track. A vertex is constructed using the "UnconstrainedV0Candidates" collection. An unconstrained vertex studies the closest approach of an e^+e^- track pair to construct a vertex. While the beamspot constrained vertex collection was not used for measuring vertex position of a pair, the χ^2 of the beamspot constrained vertex fit described the quality of how closely the two tracks pass each other in addition to how well the total momentum projects back to the beamspot position at the target. The beamspot constrained collection is not used as the primary collection for studying the vertex position because the beamspot position at the target is not precisely known. If using the z vertex position from a beamspot constrained fit, the size

of the beamspot weights the significance of the beamspot as a factor in the vertex fit. A bad beamspot position can systematically pull the measured vertex position. For genuine A' displaced vertices, the z vertex position is relatively unchanged when using a beamspot vs an unconstrained vertex fit. For identifying backgrounds, prompt vertices that are pushed to large z through measurement error, the beamspot constraint can arbitrarily bias the location of the scattered vertex. In order to avoid bias to the reconstructed z vertex position, the unconstrained fit is used.

The tracks are projected to the Ecal and matched to clusters based on position and momentum. There exists an established parameterization of the track-cluster matching that can be used to measure the quality of the match as a count of standard deviation, $n\sigma$. Furthermore, the Ecal has a superior timing resolution to the SVT and the time difference between two clusters can be used to study both accidentals and elimination of tracks originating from different events.

There are a few cuts that originate specifically from studies of high z background events and physics processes which include cuts on the positron track's distance of closest approach in the XZ plane to the target (DOCA), the $e + e^-$ momentum asymmetry, and the number of hits shared between tracks. All of these cuts will be discussed in detail for the 0.5 mm L1L1 dataset and their adaptations will be summarized for other datasets. Additionally, all data described here uses the tweakPass6 results.

6.2 SVT AT 0.5 MM FROM THE BEAM

The following section consists of three different datasets used to measure a combined 0.5 mm reach. The 0.5 mm data was recorded during stable beam times when the SVT bias voltage was on, and the SVT layer 1 was positioned at ± 0.5 mm from the beam.

6.2.1 L1L1

The follow section discusses the cuts and results of the 0.5 mm dataset where both the $e + e^-$ tracks have their first hit in layer 1 of the SVT.

Cuts

The cuts used on the L1L1 0.5 mm dataset are shown in Table 5.

TABLE 5: Cuts applied to the L1L1 datasets.

Cut type	Cut	Cut Value	%killed	%killed core	%killed tails
track	Fit quality	track $\chi^2 < 30$	60	34	87
track	Max track momentum	$P_{trk} < 75\%E_{beam}$	11	9	22
track	Isolation		4	2	19
vertex	beamspot constraint	$bsc\chi^2 < 10$	26	20	72
vertex	beamspot - unconstrained	$bsc\chi^2 - unc\chi^2 < 5$	9	9	21
vertex	maximum P_{sum}	$< 115\%E_{beam}$	1	0	2
ecal	Ecal SVT matching	$\chi^2 < 10$	7	6	49
ecal	track Ecal timing	$< 4\text{ns}$	4	4	7
ecal	2 cluster time diff	$< 2\text{ns}$	6	6	13
physics	momentum asymmetry	< 0.4	13	13	27
physics	e+ track d0	$< 1.5\text{mm}$	0	0	1
event	max shared hits amongst tracks	< 5 shared hits	14	14	15

In Table 5, the "cut type" is a simple summary of what the cut is intended to have the significant most effect on. The three columns under "data" show where the cut removes data from the vertex distribution as a function of the percentage of events that are killed by the cut. The "%killed" refers to the total statistics removed by the cut in events downstream of the target. The "%killed core" refers to events that are found in the core of the vertex distribution (within 10 mm of the target). The "%killed tails" refers to events after 10 mm from the target.

The effects of the cuts on the z vertex for all masses is shown in Figure ?? in the cumulative order in which the cuts are applied. The initial track fit χ^2 from the GBL fit of the track removes a lot of background and begins to really shape the vertex distribution. The next significant cut is the beamspot constrained χ^2 cut. The beamspot constrained χ^2 includes both the closest approach of the two tracks and the momentum projection of the vertex back to the beamspot position at the target. The momentum asymmetry is a cut that is primarily designed to remove WAB contributions to the data. Heavy photon generated $e + e^-$ pairs are generally close in energy whereas the electron in WAB typically carries a much larger energy than the counterpart photon. The last cut listed in Table 5 removed events where the $e + e^-$ individual tracks share five hits with other tracks. When studying the original high z background from the pass6 dataset, it was clear that nearly all of the high

z events were poorly reconstructed tracks due to missing hits in Layer 2 or five hits with other tracks in the event having nearly the same momentum. The cuts cleaned up all of the original high z background. The effects of the cuts on the z vertex distribution can be seen in Figure 6.3.1.

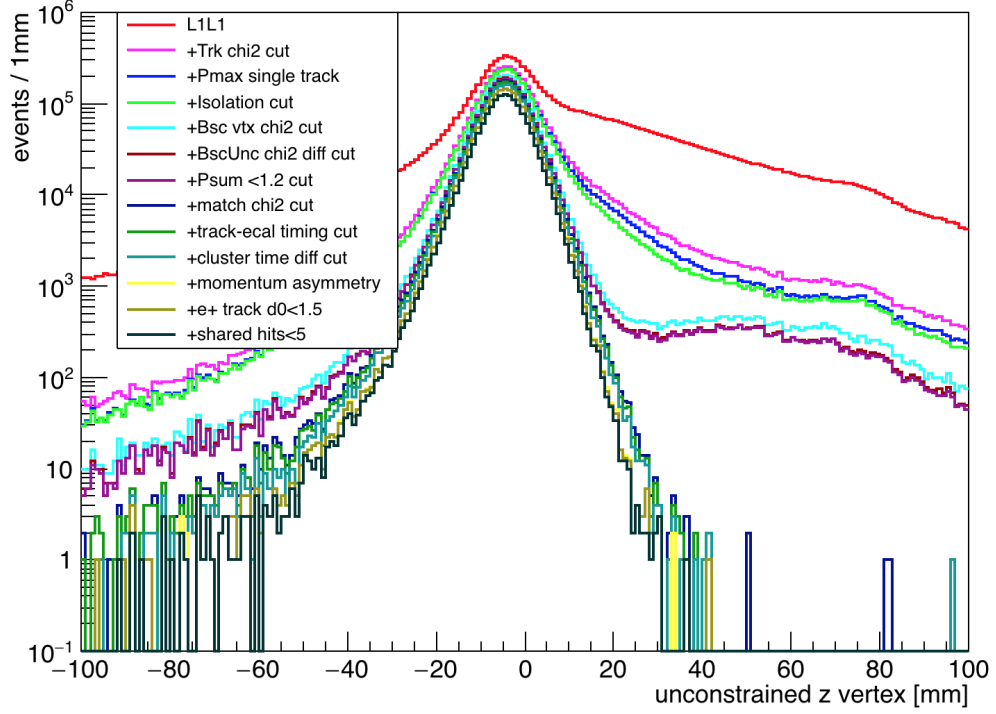


FIG. 6.2.1: Cut effects on the z vertex distribution for all masses in the L1L1 0.5 mm dataset.

The ratio of the final events selected after applying all cuts to the original events selected after initial cuts is shown in Figure 6.3.2.

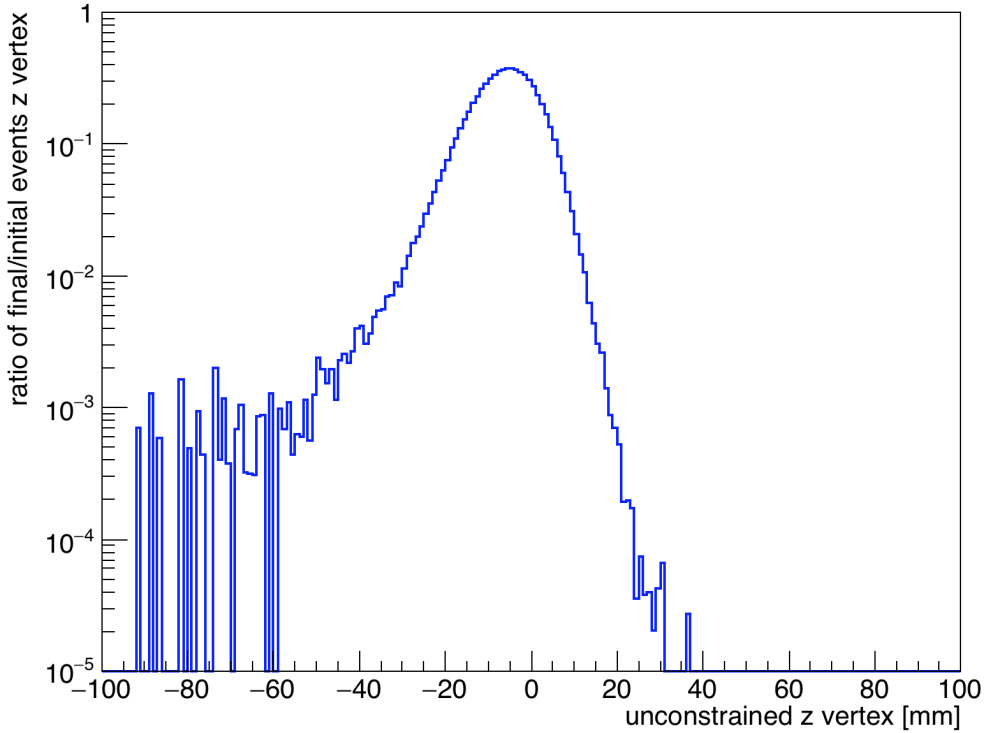


FIG. 6.2.2: The ratio of the z vertex distribution in the final event selection to those events in the initial event selection in the L1L1 0.5 mm dataset.

The two cluster time difference can be used to study the effects of cuts on accidentals as well as the contamination of accidentals in the final sample. The evenly space 2 ns peaks as apparent in Figure 6.3.3 are due to the intrinsic 499 MHz frequency at which electron beam bunches enter Hall B and interact with the HPS target.

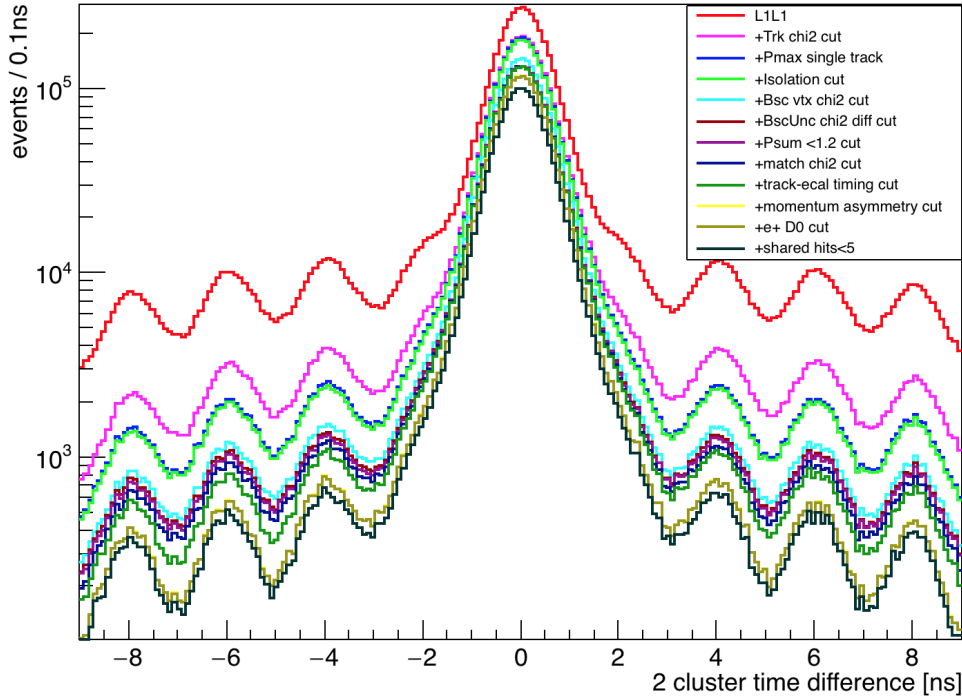


FIG. 6.2.3: Cut effects on the two cluster time difference distribution for the L1L1 0.5 mm dataset.

The effect of the cuts as shown in Figure 6.3.3 on the final and initial distributions can be seen as a ratio in Figure 6.3.4.

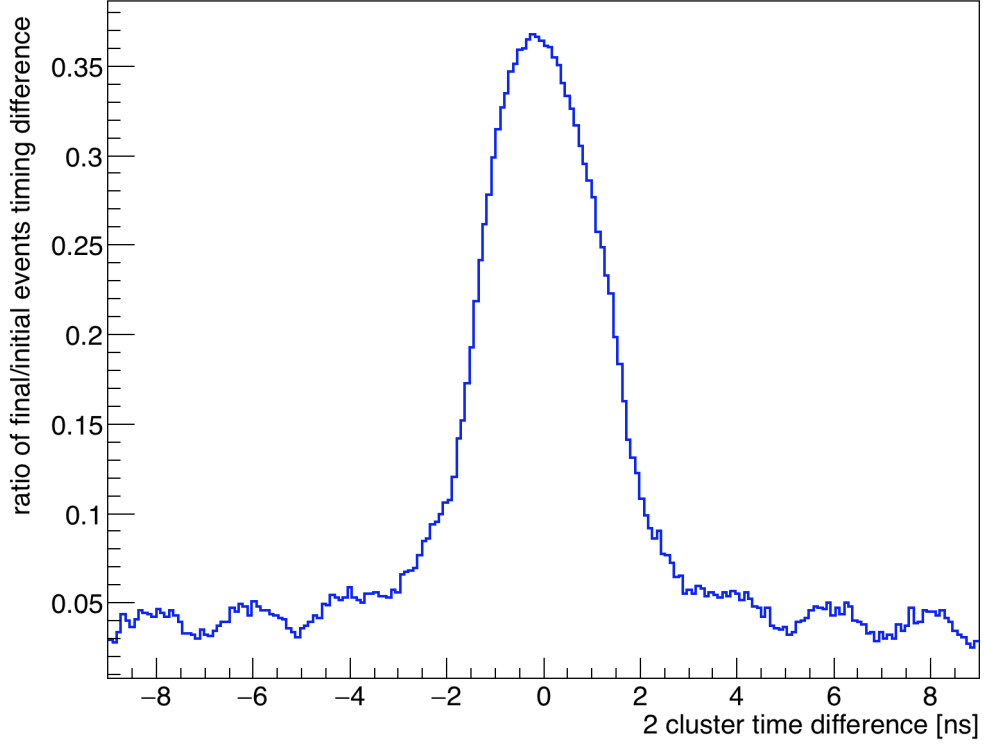


FIG. 6.2.4: The ratio of the two cluster time difference distribution in the final event selection (without the ± 2 ns cut) to those events in the initial event selection for the L1L1 0.5 mm dataset.

After all cuts are applied, the accidental contamination is less than 1% in the ± 2 ns event selection (this cut is the only one not shown in Figure 6.3.3). Further studies to identify the production of high z vertices using accidentals is discussed later on in this section. The cut effects on the mass distribution for the vertex search can be seen in Figure 6.3.5. In particular, the track-cluster matching removes the low end tail of the mass distribution which is consistent with the geometric acceptance of the experimental setup.

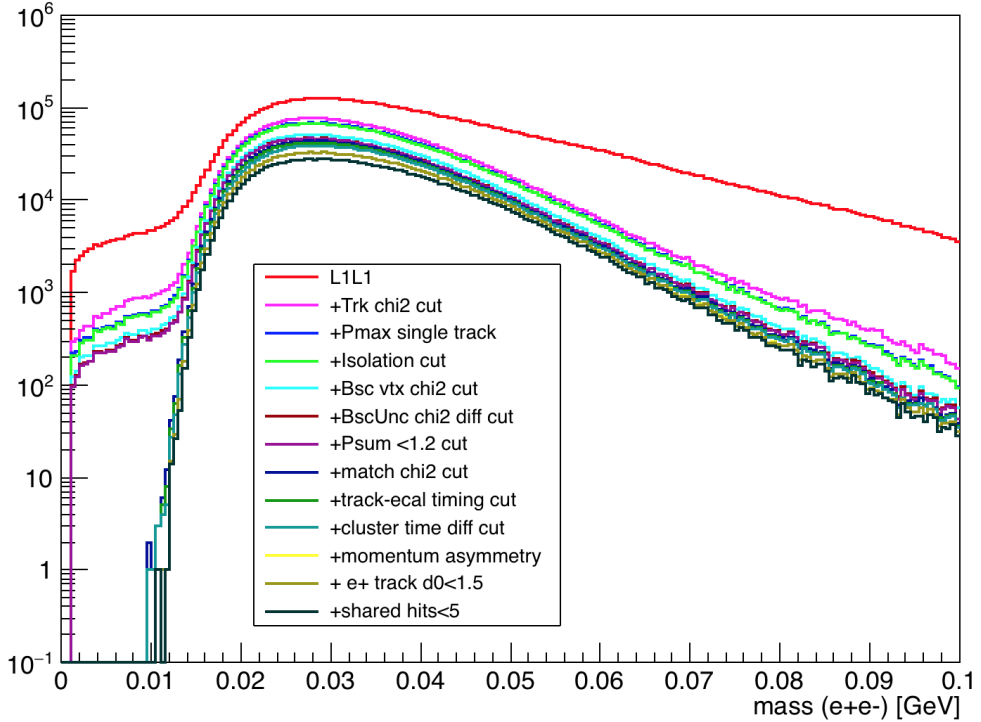


FIG. 6.2.5: Cut effects on the mass distribution for the L1L1 0.5 mm dataset.

An overview of the significant cuts will be discussed here. Any cut that is different from the L1L1 dataset will be discussed separately in the section with the relevant dataset.

The initial selection for the dataset requires that both tracks have hits in Layer 1 of the SVT and Layer 2. Previously, the requirement of Layer 2 was not used, but as the rates are highest in Layer 1 of the SVT, the extrapolation from Layer 3 to Layer 1 is critical in order to correctly measure the vertex of the track. Additionally, the inefficiency in measuring a hit in Layer 2 is approximately 2% of the time (and is different for electrons and positrons). Included in the initial event selection is also the radiative cut at 80% of the beam energy. After these initial cuts, we apply the track selection cuts. To ensure general track quality, the track χ^2 is used as shown in Figure 6.3.6.

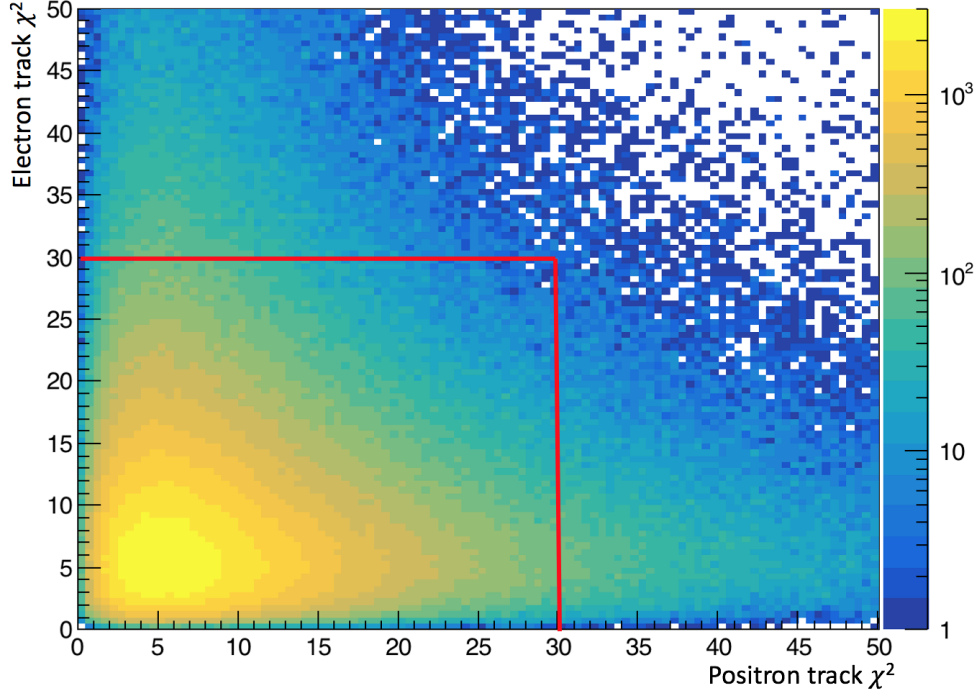


FIG. 6.2.6: The electron and positron track χ^2 are shown with the cut indicated by the red line. This cut is an initial track selection quality cut and uses no vertex or timing information.

After choosing tracks based on their individual fit qualities, we remove electron tracks that have greater than 75% of the beam energy. This cut is made to ensure that we are not choosing elastically-scattered (beam energy) electrons and corresponds also to the general maximum value we can expect for an electron track in trident events. A comparison between the data and Monte Carlo is shown in Figure 6.3.7.

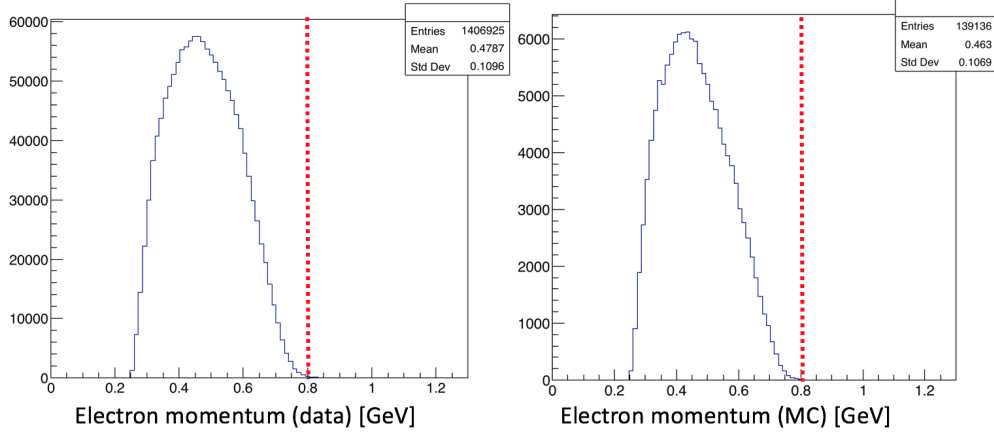


FIG. 6.2.7: The maximum momentum of the electron track as shown in data (prior to cutting) and Monte Carlo. Events with higher electron energies are attributable to other types of backgrounds in the data such as elastics and wide angle bremsstrahlung and not the trident background.

The next cut applied is the isolation cut. The isolation value for the electron and the positron in the L1L1 dataset is the distance to the next closest hit away from the beamline in Layer 1 relative to the electron and positron hit used in the track. This cut compares the isolation value (parameter δ) to the track projected value in y at the target position (also known as the track z_0 parameter). If the projected isolation to the target is larger than the z_0 parameter at the target, then we assume that the better hit was already chosen for the track. A picture of the variables used in this cut is shown in Figure 6.3.8.

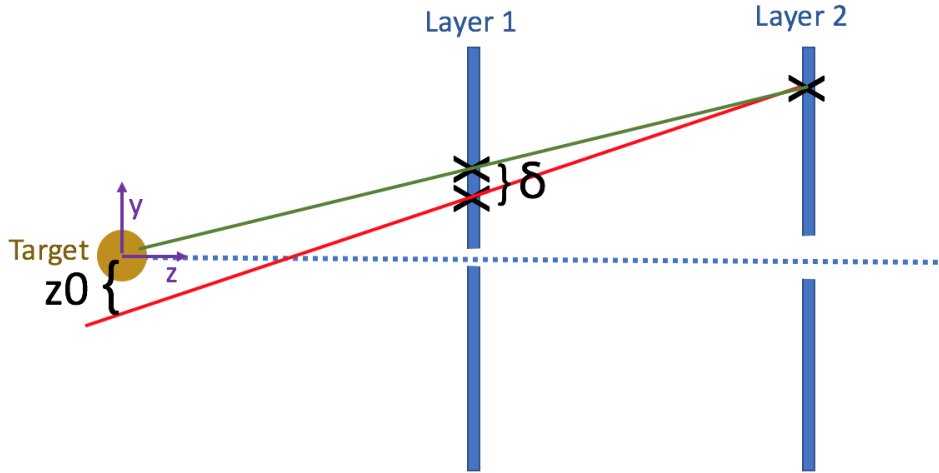


FIG. 6.2.8: The distance between the closest hit away from the beam in Layer 1 is compared to its projection at the target the track impact parameter, z_0 at the target.

The cut shown is described numerically in Equation (6.3.1).

$$2\delta + z_0 \times \text{sign}(PY) > 0 \quad (6.2.1)$$

Because the distance from Layer 2 to the target is twice the distance between Layer 1 and the target, we compare the isolation times a factor of 2 to the z_0 parameter in order to compare the projection to the target. The z_0 parameter is opposite in sign as compared to the *y*-component of the track momentum because we only consider downstream vertices.

In identifying downstream vertices, we use the unconstrained vertex collection to optimize our search for detached vertices. For each vertexed $e + e^-$ pair, we can see how the vertex is changed when different additional constraints are applied to the vertex. The unconstrained vertex collection only looks at the distance of closest approach between the two tracks. The target constrained vertex collection is optimized for a bump hunt analysis and requires that the vertex of the $e + e^-$ pairs occurs at the target. The beamspot constrained vertex collection requires that the momentum of the vertexed pairs projects back to the beamspot location at the target and considers the distance of closest approach between the two tracks.

The beamspot constrained vertex χ^2 , can give us information about how well the vertex momentum points back to the beamspot location at the target. The beamspot constraint is particularly useful in identifying events where a track has scattered significantly because the projected momentum misses the beamspot location at the target. Real signal will always project back to the beamspot. The effect of the beamspot constraint cut on the vertex χ^2

distribution alone can be seen in Figure 6.3.9.

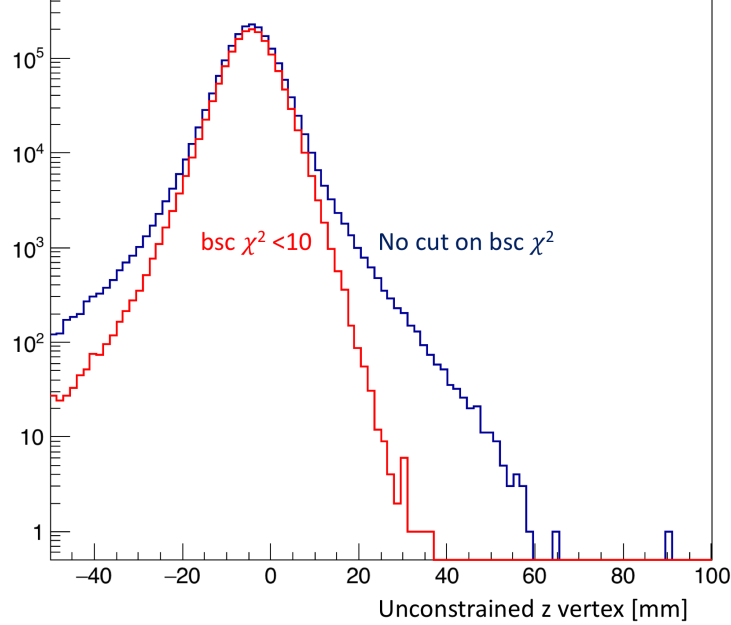


FIG. 6.2.9: The effect of a cut on the beamspot constrained χ^2 on the vertex distribution for all masses. While this plot is shown for all masses, the effects of the cut on the tails of the distribution can still be seen. The cut removes events where tracks did not pass close to each other in space to generate a vertex and/or the vertex does not point back to the beam position at the target.

The difference between the beamspot constrained and unconstrained χ^2 can also be used to exclusively identify how well a vertex points back to the target. The effect of this cut can be seen in Figure 6.3.10.

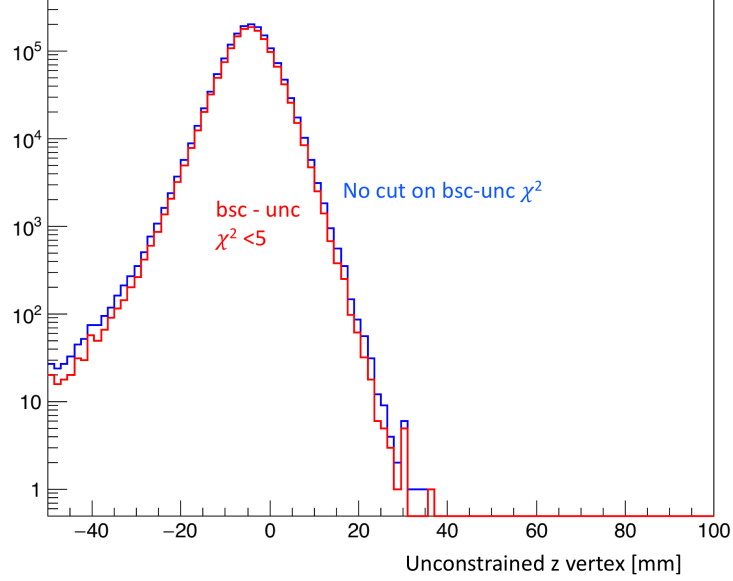


FIG. 6.2.10: The effect of a cut on the difference between the beamspot and unconstrained constrained χ^2 on the vertex distribution for all masses. The effects of the cut on the downstream tails of the distribution tells us how well a vertexed pair of tracks points back to the beamspot position at the target.

The next cut is the maximum momentum of the $e + e^-$ pair. This cut removes very few events but is still necessary to ensure that we are not including events that are not correlated. After having established the quality of the tracks and vertex using the SVT information only, the tracks are projected to their positions at the Ecal and the quality of the matching of the track and Ecal cluster is described as a function of the track momentum and position at the Ecal. This parameter is a function of the number of σ from distributions studied used 2015 data. The matching parameter and relevant cut value are shown in Figure 6.3.11.

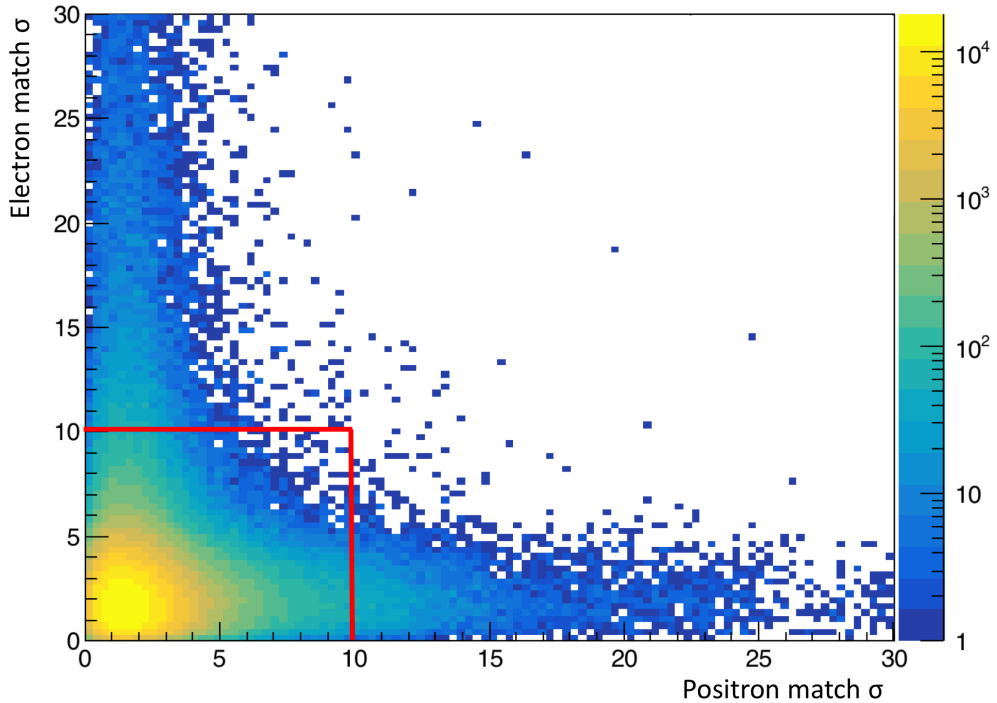


FIG. 6.2.11: The matching parameter for both electrons and positrons is shown. The maximum is set to 30σ , and the cut is set to 10σ for each particle.

The matching cut most significantly removes the small angle/low mass background events that we saw in Figure 6.3.5. The timing difference between the tracks and Ecal clusters removes some out of time events, but the timing resolution on the clusters is more precise than the track time and a cut on the two cluster time difference is critical for removing accidentals. The cut can be seen in Figure 6.3.12.

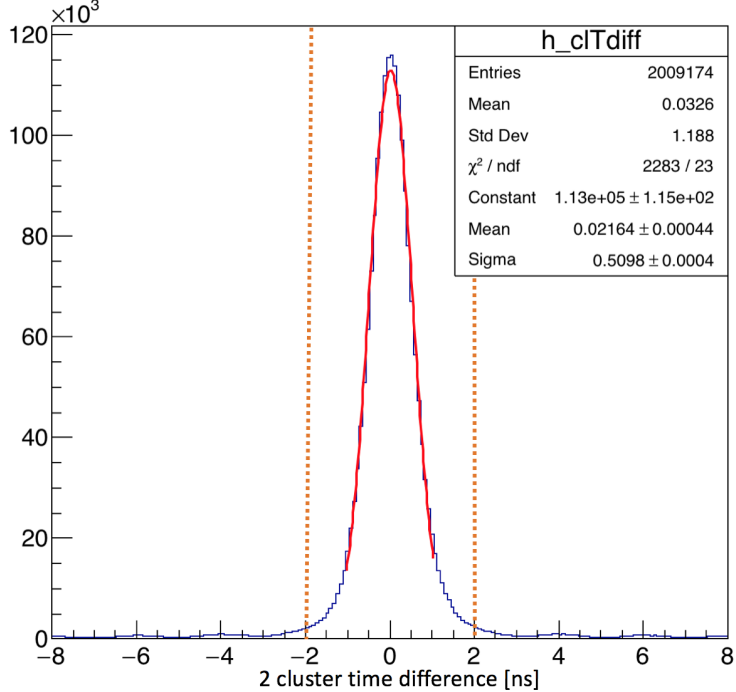


FIG. 6.2.12: The two cluster timing difference is shown with a fit to the Gaussian central part of the distribution. Additional smaller peaks can be seen in intervals of 2 ns in the tails of the distribution. The timing cut can remove these events where overlapping beam buckets generate out of time vertices.

Additional cuts aimed to remove the contaminating wide angle bremsstrahlung background events include a cut on the momentum asymmetry of the two tracks and the positron $D0$, or $DOCA$ (distance of closest approach to the target in the x-z plane), are used. The $e + e-$ pairs produced in radiative trident processes from heavy photon decays are closely symmetric in momentum. The momentum asymmetry is defined as the momentum difference of the two particles divided by the momentum sum. The electron in wide-angle bremsstrahlung typically carries a significantly higher portion of the beam energy when compared to the positron that is produced from the pair production of the lower energy photon. The effects of the momentum asymmetry cut on the vertex distribution are shown in Figure 6.3.13.

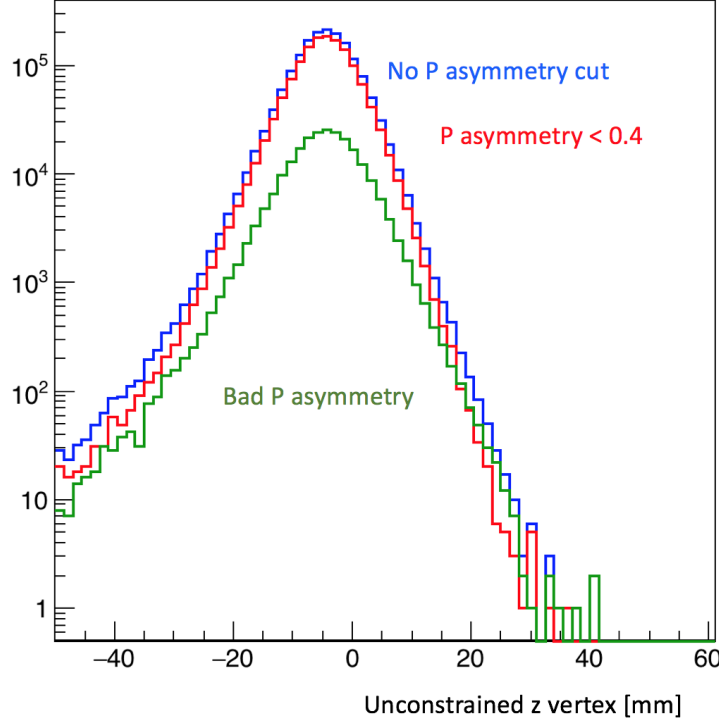


FIG. 6.2.13: The effect of the momentum asymmetry cut on the tails of the vertex distribution can be seen in the red and green curves.

The momentum asymmetry cut can effectively reduce contamination from wide-angle bremsstrahlung in the final event sample. In wide-angle bremsstrahlung, the scattered electron and the positron from pair conversion are detected. When a positron is produced downstream of the target in this process, the projected *DOCA* of the resultant track to the target will be positive due to the curvature of the positron track in the magnetic field from starting downstream. The cut on the *DOCA* and its effect on the vertex distribution can be seen in Figure 6.3.14.

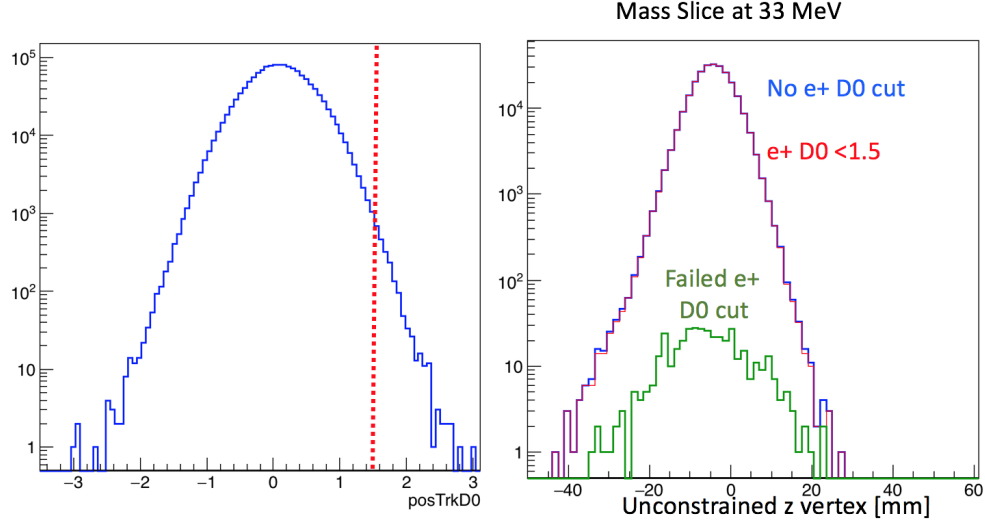


FIG. 6.2.14: Positrons that are produced from the photon in wide-angle bremsstrahlung events will have a distance of closest approach that will curve widely at the target location, yielding a largely positive value.

The final cut on tracks was derived after studies of the high z background events showed a higher probability of one or both of the tracks sharing five hits with another track in the event. In these cases, the track with the best χ^2 track fit is selected, but the momentum difference with the other track with which it shares five hits is quite small. The momentum difference of the track with the other tracks that share hits is shown versus the number of hits shared between the tracks in Figure 6.3.15.

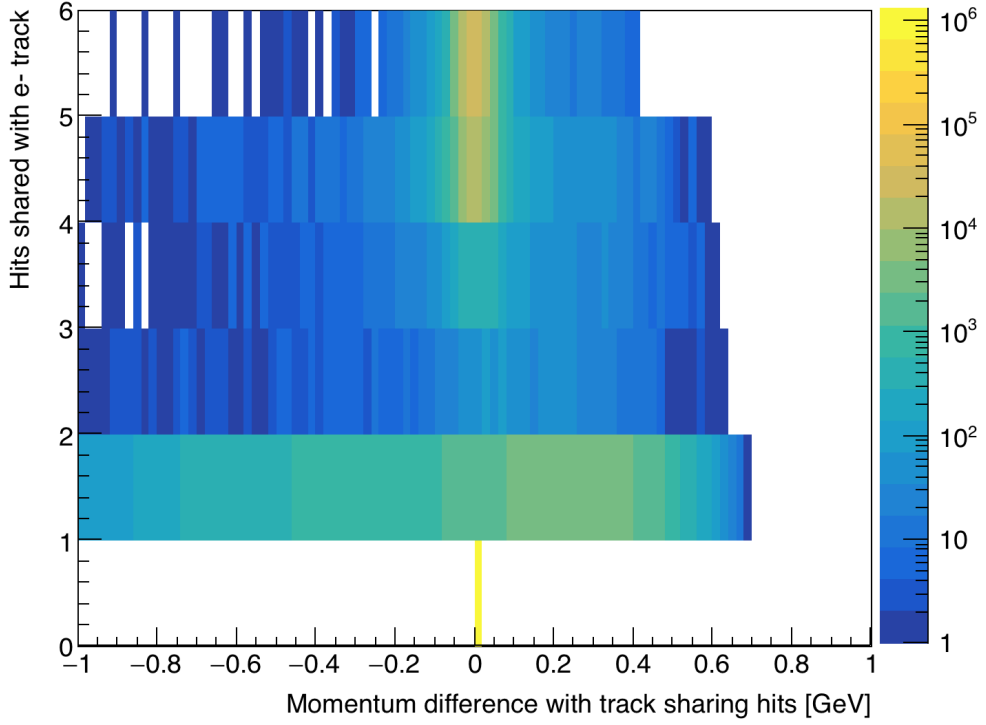


FIG. 6.2.15: This plot shows that many of the tracks sharing 4 and 5 hits with the initial track selected in the event have nearly the same momentum.

By removing tracks that only have a one hit difference with other tracks, the high z background in the unblinded sample is reduced.

Vertex reconstruction efficiency, ϵ_{vtx}

The integral as described in Equation (??) contains an ϵ_{vtx} parameter that varies as a function of both mass and vertex position z. Using A' Monte Carlo, the ϵ_{vtx} can be calculated and the efficiency can be parameterized as a function of mass and z. At each mass, the ratio of the measured to generated heavy photon events is scaled such that for L1L1, the fitted ratio is 1 at that target position. The L1L2 and L2L2 datasets are scaled to ensure the same relative relationship between the three datasets. The efficiencies for a 35 MeV heavy photon are shown in Figure 6.3.16.

0.5mm, A' mass = 35 MeV

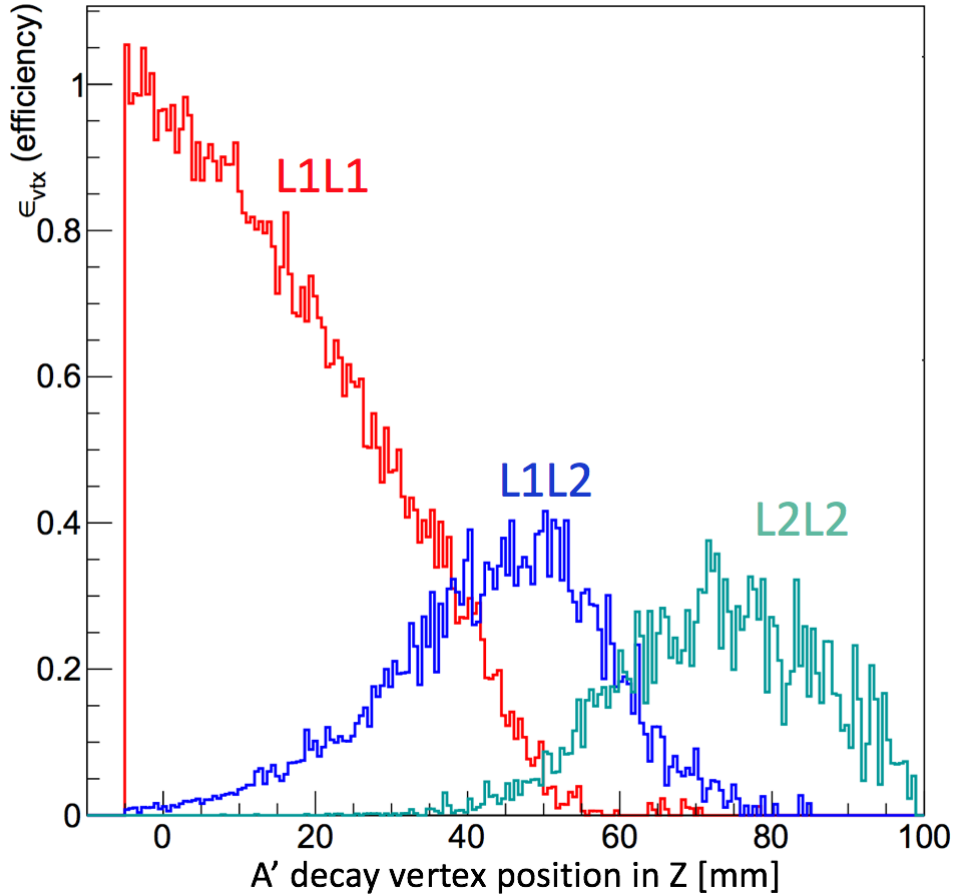


FIG. 6.2.16: 35 MeV A' reconstruction efficiency versus the vertex position.

As all datasets are mutually exclusive of each other, one can see that the total reconstruction efficiency for all z vertex positions is the sum of the efficiencies for the individual datasets as shown in Figure 6.3.16. These efficiencies are then integrated from different zCut values to zMax (roughly set at the z position of Layer 1). The efficiency at each mass is for each dataset is fit as shown for a 30 MeV heavy photon in Figure 6.3.17.

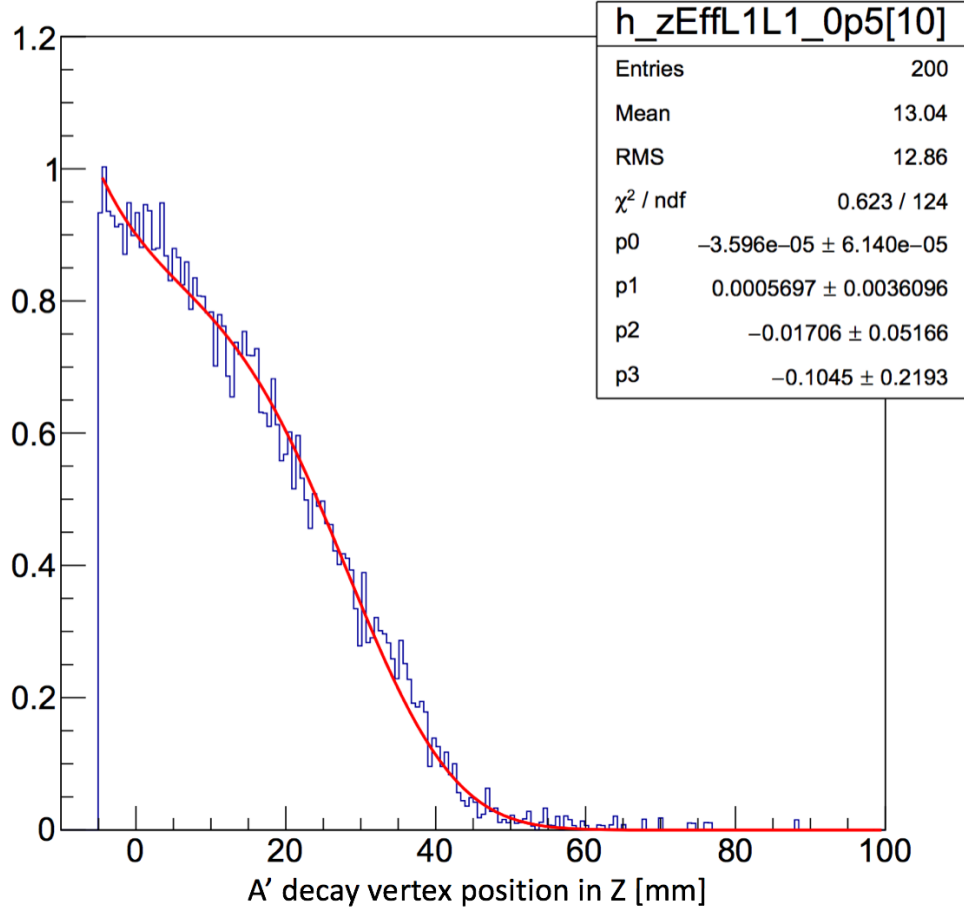


FIG. 6.2.17: Fit that describes the L1L1 efficiency for a 30 MeV heavy photon.

The parameters of the fits to all masses are then parameterized as a function of mass. Once these relations are derived, then we obtain a value for ϵ_{vtx} that can be used in the integration for calculating the expected A' signal yield. For L1L1, the vertex reconstruction efficiency can be described as shown in in Equation (6.3.2).

$$\epsilon_{vtx} = \exp(p_0 + p_1 z + p_2 z^2 + p_3 z^3) \quad (6.2.2)$$

The parameters in Equation (6.3.2) are functions of mass and are shown below:

$$\begin{aligned}
 p_0 &= -0.2359 + 3.606m \\
 p_1 &= -0.03537 + 0.5395m \\
 p_2 &= -0.001201 + 0.1404m - 2.614m^2 + 10.65m^3 \\
 p_3 &= -0.0002078 + 0.008753m - 0.1396m^2 + 0.8077m^3
 \end{aligned}$$

The full integral value yields some fractional number that, when multiplied by the expected heavy photon yield from the cross section, tells us how many heavy photons we can expect to reconstruct in the given decay vertex region. For the L1L1 dataset, it is critical to set the zCut as low as possible in order to obtain the highest signal yield. In Figure 6.3.18, the value of the integral indicated by the color on the z-axis, is shown for $\epsilon^2 = 5E - 9$ as a function of mass and zCut. The zMax was set to 100 mm in this calculation.

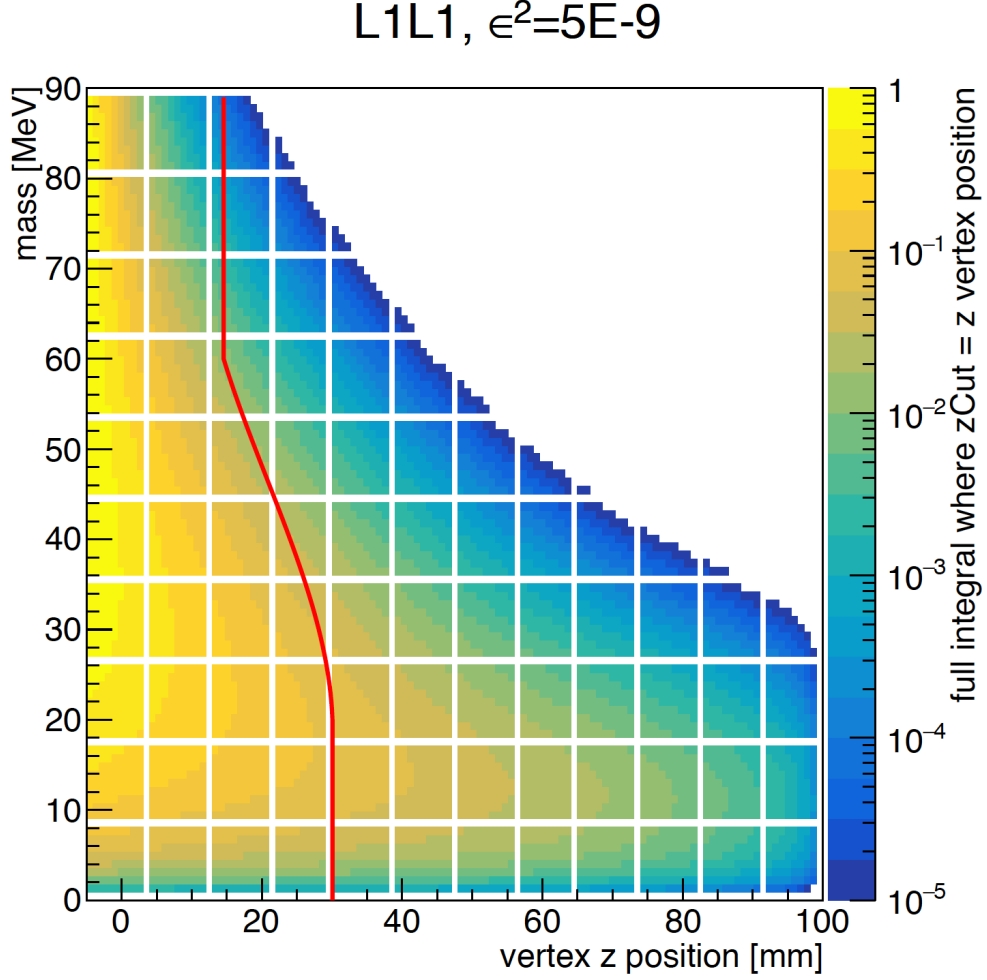


FIG. 6.2.18: The colored value is the value of the full integral from Equation (??) for the L1L1 dataset using the zCut value on the x-axis. The red line indicates the zCut value derived in data for 0.5 background events. This zCut shown is for the 10% unblinded data.

The red line shown in Figure 6.3.18 indicates the zCut projection for the 10% unblinded L1L1 dataset. In Figure 6.3.19, the integral from this zCut to 100 mm is shown as a function of mass for various couplings.

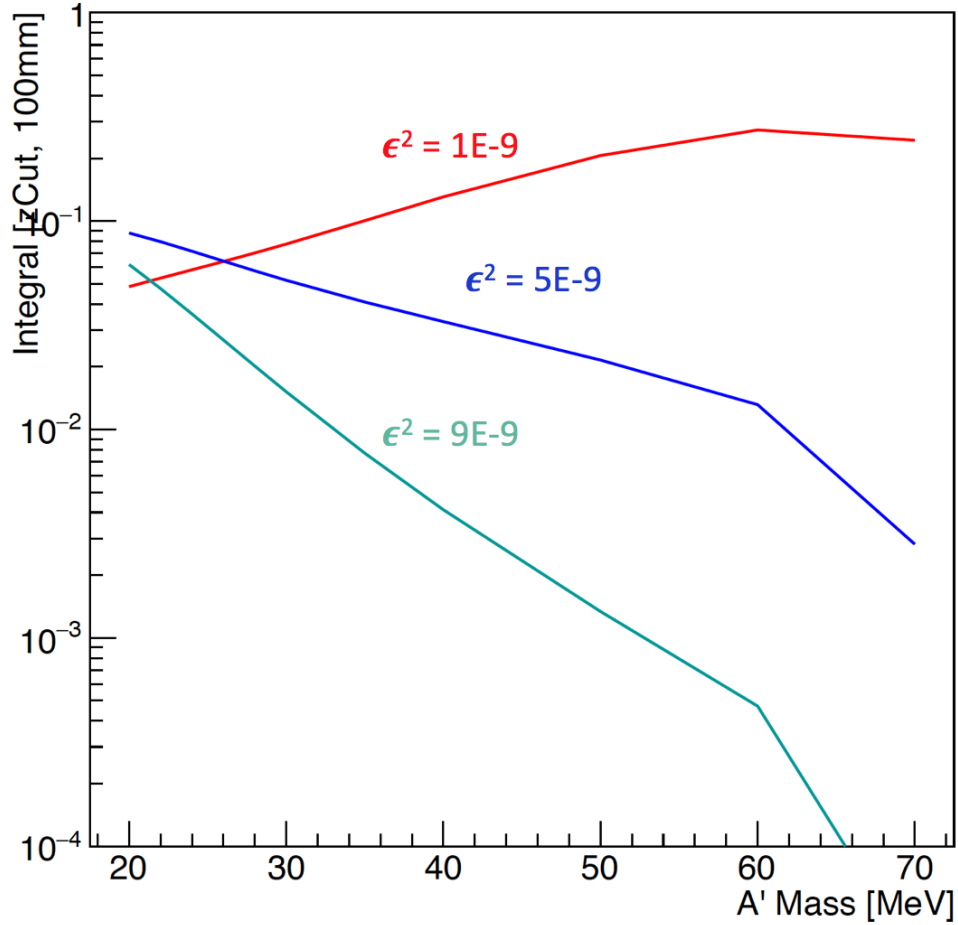


FIG. 6.2.19: For a fixed ϵ^2 coupling, the full integral value from z_{Cut} to the first layer of the SVT is shown as a function of mass.

In the L1L1 dataset, the vertex reconstruction is most efficient for larger couplings as shown in Figure 6.3.19. Due to the geometric effects of the requirement to reconstruct tracks both passing through layer 1 of the SVT, the integral shows the highest efficiency for smaller couplings with larger masses.

Mass resolution

The mass resolution is determined from A' Monte Carlo and has been checked with the $e - e-$ mass resolution from Moller scattered electron pairs in data. By generating heavy photons at discrete masses, applying the cuts proposed in data, and fitting the A' mass peak residual with respect to the generated mass peak, the mass resolution can be measured as a function of mass. Fits to this peak are shown in Figure 6.3.20.

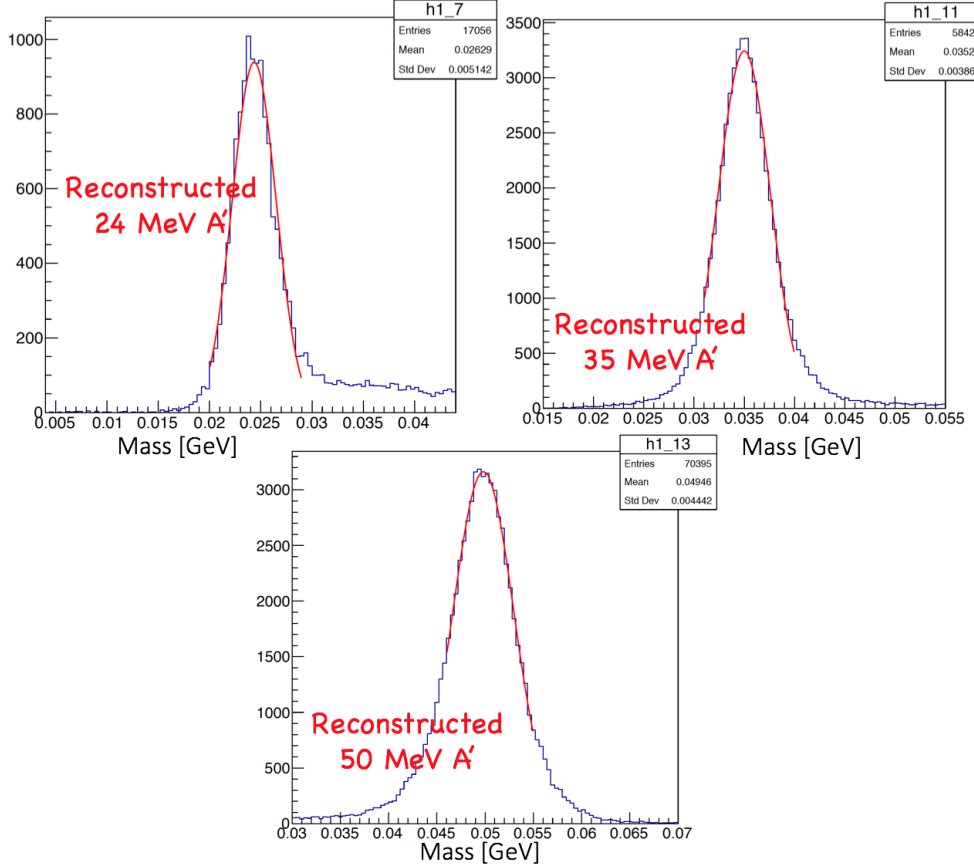


FIG. 6.2.20: Fits to the residual of the A' mass peak as reconstructed in Monte Carlo.

This resolution encompasses the measured angular resolution of the pair as well as the resolution of the measured momentum. It has been shown previously that while the mass resolution is dominated by the angular resolution term, there is no dependence with the vertex z position. The mass resolution as a function of mass using heavy photon Monte Carlo is shown in Figure 6.3.21.

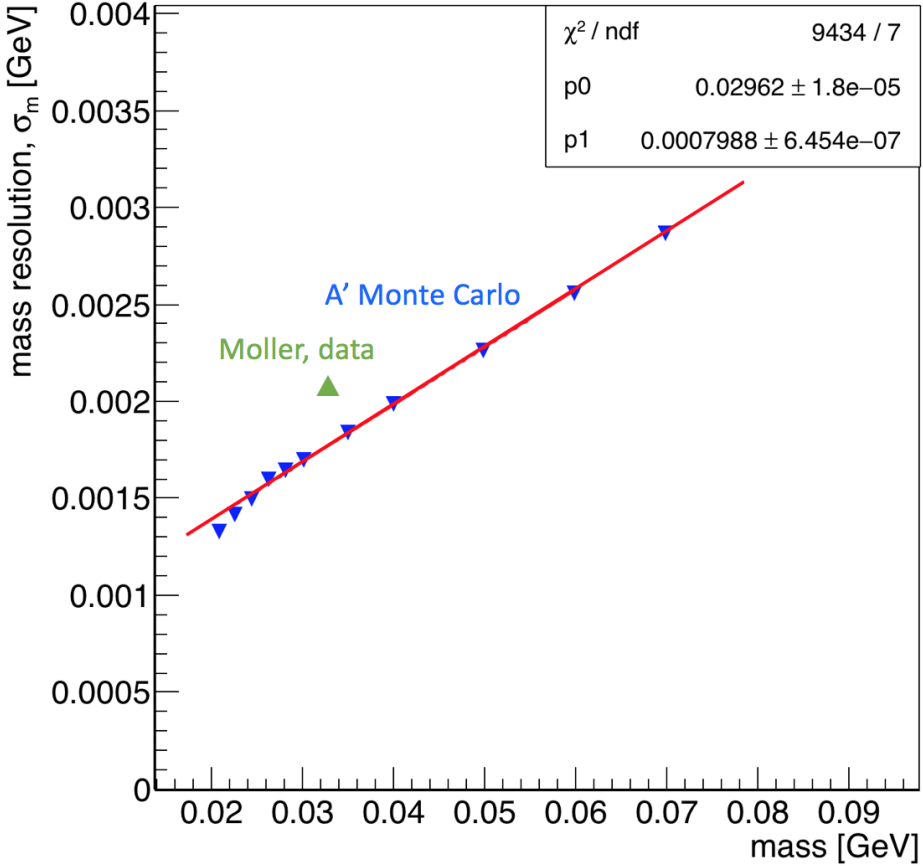


FIG. 6.2.21: The mass resolution from A' MC can be parameterized linearly as $p_0 m + p_1$ with the fit values shown on the plot. The Moller mass is one of the only real benchmarks to compare with the data and indicates a possible offset with the mass resolution measured in data.

Simulations of the Moller mass can be used to study systematic offsets between the measured mass in data and the mass as found in Monte Carlo. Using Moller Monte Carlo (with no beam background), the Moller mass can be seen in Figure 6.3.22.

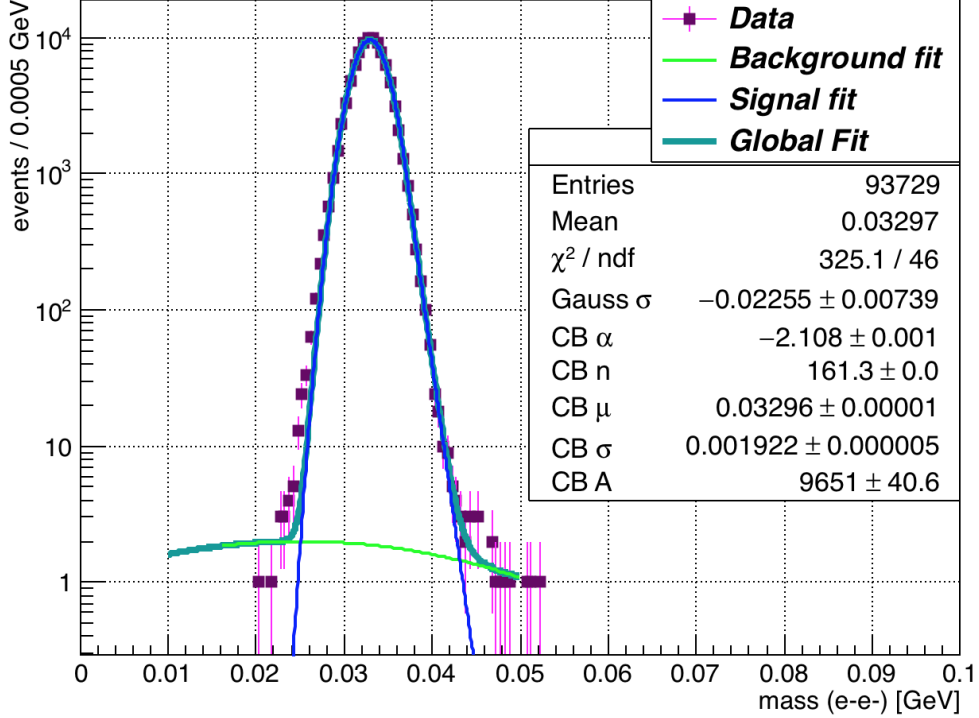


FIG. 6.2.22: The fit to the moller mass peak as found in Monte Carlo is shown. The fit uses a crystal ball function to describe the signal and a Gaussian to fit the low background under the peak.

The Moller mass from Monte Carlo can be immediately compared with the Moller mass as found in data. The difference in resolution between the peak from the pure Monte Carlo Moller sample and the Moller sample in data is approximately 17%. This difference should be applied to the heavy photon mass resolution found in Monte Carlo in order to appropriately scale the bin widths when slicing and fitting the vertex distribution by mass. The Moller peak from data is shown in Figure 6.3.23.

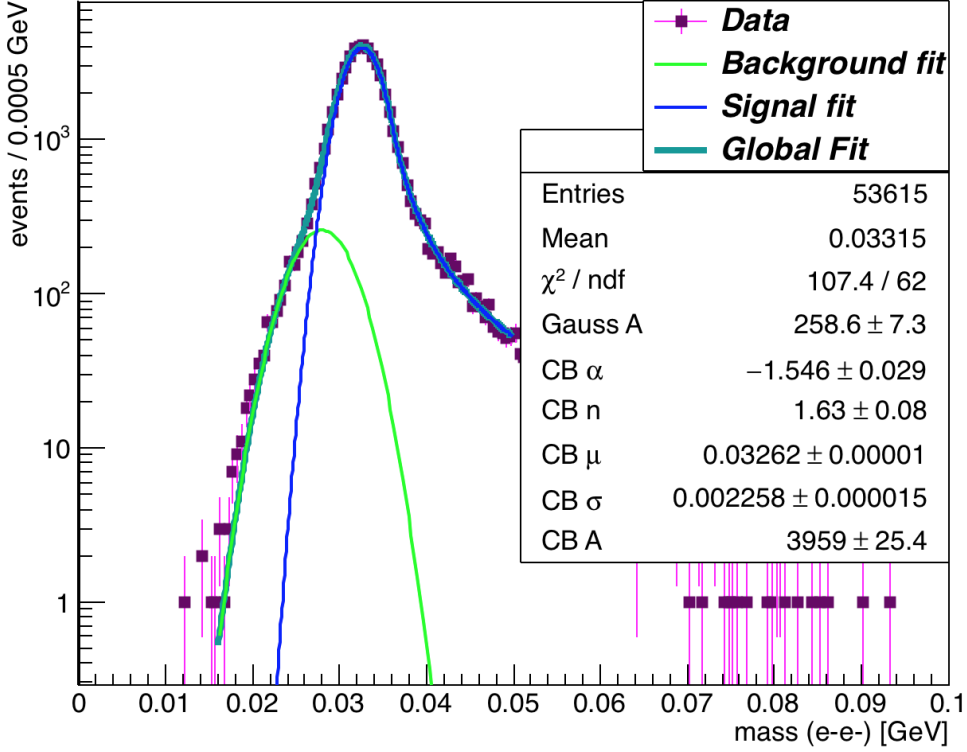


FIG. 6.2.23: The fit to the Moller mass peak as found in data is shown. The fit uses a crystal ball function to describe the signal and a Gaussian to fit the low mass background side to the peak.

After applying the 17% scaling to the mass resolution from A' Monte Carlo, we obtain the mass resolution in Equation (6.3.3).

$$\sigma_m = 0.02428m + 0.000787 \quad (6.2.3)$$

The scaled mass resolution in Equation (6.3.3) is used in the vertex analysis to find the z vertex cut.

Accidentals

The effects of accidentals on the vertex backgrounds must be understood if one is to understand the signal significance after unblinding. The rigorous way to accomplish this can be done by selecting electrons and positrons from different beam buckets and vertexing these pairs to create a high statistics sample to study. As the ability to vertex pairs from different beam buckets is not yet implemented in the HPS software, we can select $e + e -$

pairs with larger than 3 ns time difference and less than 9 ns time difference. As we go to larger time differences, we begin to lose events due to the SVT inefficiency outside of the trigger window. The final data selection cut is for clusters that are within ± 2 ns and includes two beam buckets. By looking for high z vertices generated in the six out of time beam buckets, we can obtain an estimate for the number of accidentals we will expect to see when we unblind. For the L1L1 dataset, the vertex distribution for the selected accidentals is shown in Figure 6.3.24.

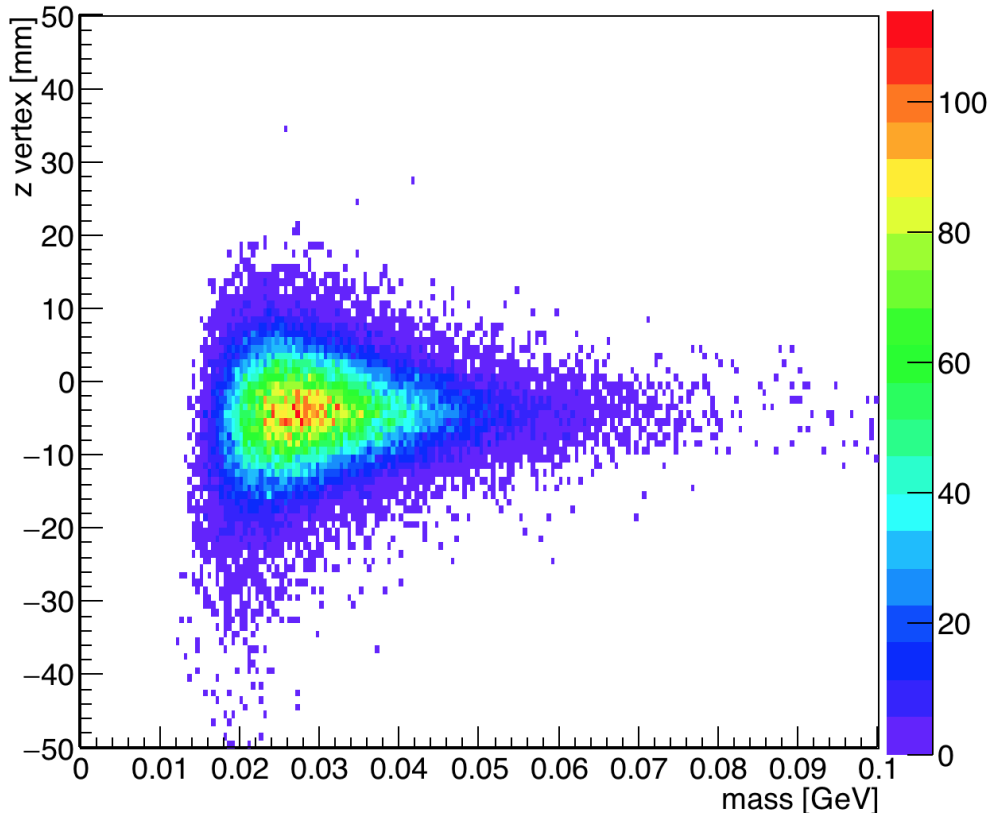


FIG. 6.2.24: After selecting events where the cluster time difference is greater and 3 ns and less than 9 ns, the vertex distribution for the six beam buckets is shown.

As seen in Figure 6.3.24, there are 3 visible high z events. If we translate this effect to the two beam buckets in our selected events peak, we could expect 1 ± 0.6 accidental events in the 10% unblinded data. This could account for 10 ± 6 events in the full 100% dataset. It is worth noting that the high z background events appear to be randomly distributed among the mass bins.

Projected reach

We estimate our reach by using Equation (??). In order to establish 90% confidence limits, we should expect to see 2.3 events or greater in the corresponding mass bin. The resultant z vertex distribution as a function of mass for the L1L1 dataset is shown in Figure 6.3.25.

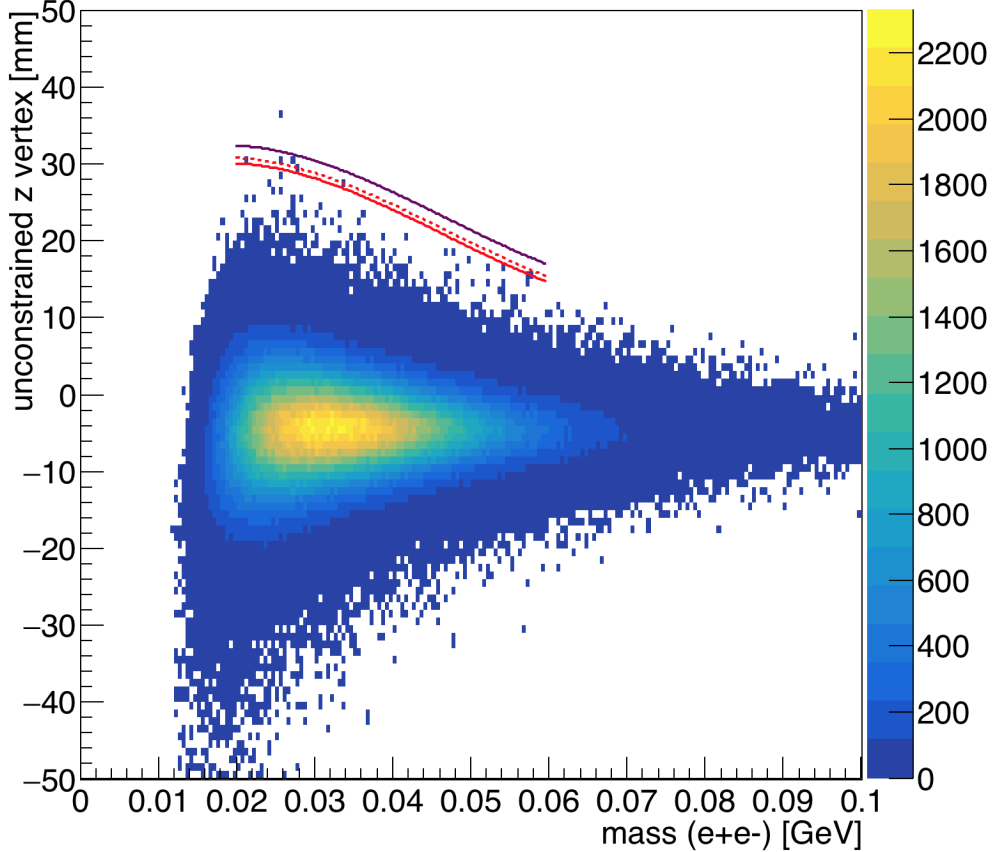


FIG. 6.2.25: Reconstructed z vertex as a function of mass for the L1L1 dataset with the first layer of the SVT at 0.5 mm from the beam. The solid red line indicates the zCut found for 10% of the data (unblinded), and the dashed red line indicates the limit at which events have a quantile greater than 0.5 with respect to the predicted background model. The purple line shows where the projected zCut will be for the full dataset after unblinding.

As shown in Figure 6.3.25, we see the zCut found for the 10% data sample after fitting the peaks and looking for the location where we have 0.5 background events in the bin. Because we have an average of 0.5 background events in each bin, we characterize the events that lie beyond the zCut using the distribution function of the exponential model for the tail. A quantity between 0 and 1 can tell us how far an event located at a particular z value,

relative to the zCut, is from being described by the background function. This distribution is described in terms of the tail length, l , by $1 - e^{(zCut-z)/l}$ and can be inverted to find the value of z relative to the zCut yielding a specific quantile. All but one event that lie beyond the zCut can be explained in accordance with the background model. After unblinding, high z events will be further investigated, and it's possibly attributable to the estimate on the rate of accidental contamination in the sample.

The final reach with the projected zCut for the 100% L1L1 dataset is shown in Figure 6.3.26.

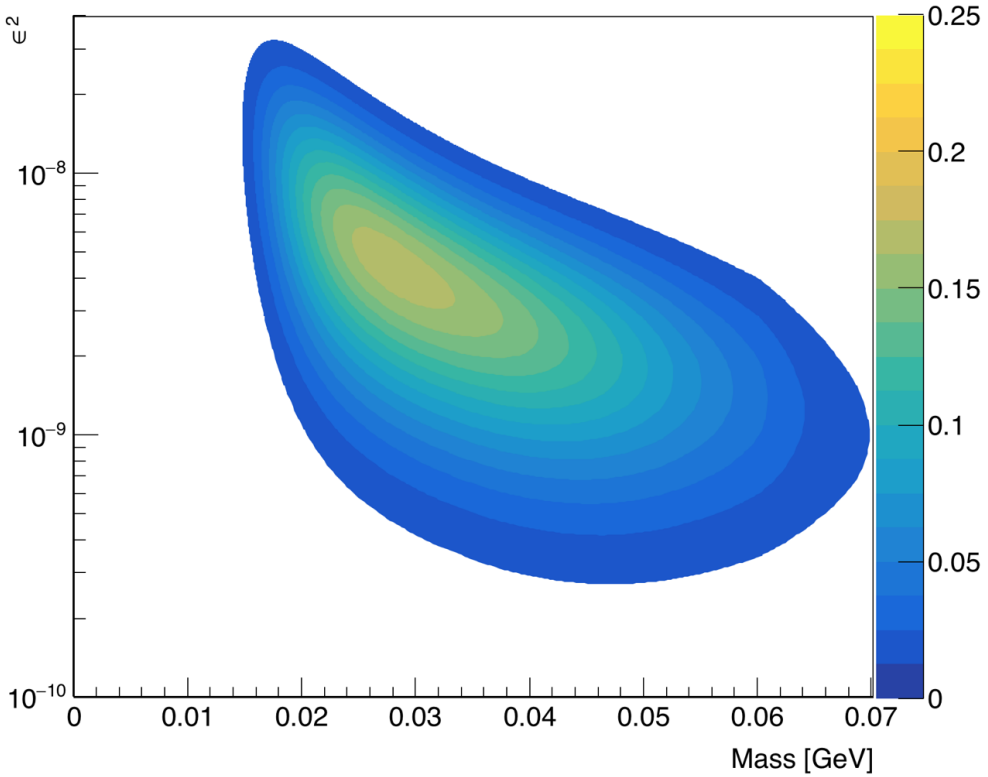


FIG. 6.2.26: The expected signal yield for the full 0.5 mm 100% dataset. This uses the zCut projection shown in Figure 6.3.25.

As seen in Figure 6.3.26, the highest signal count that can be expected from the full dataset is 0.21 events. This reach is only for the L1L1 dataset and only accounts for 1.7 days of beam time.

6.2.2 L1L2

The L1L2 dataset with the SVT at the nominal 0.5 mm position consists of tracks where the one track missed the active region of Layer 1. This dataset combines the case for which the electron passes through Layer 1 and the positron passes through Layer 1 in order to obtaining the zCut because it was noted that the tails of the distributions are the same (despite the known backgrounds being different and could merit improved cuts that would divide the dataset in the future).

Cuts

The cuts applied to the L1L2 dataset are shown in Table 6.

TABLE 6: Cuts applied to the L1L2 datasets.

Cut type	Cut	Cut Value	%killed	%killed core	%killed tails
track	Fit quality	track $\chi^2 < 30$	38	15	47
track	Max track momentum	$P_{trk} < 75\%E_{beam}$	12	8	14
track	Isolation		11	4	15
vertex	beamspot constraint	$bsc\chi^2 < 10$	46	24	60
vertex	beamspot - unconstrained	$bsc\chi^2 - unc\chi^2 < 5$	20	16	24
vertex	maximum P_{sum}	$< 115\%E_{beam}$	1	1	1
ecal	Ecal SVT matching	$\chi^2 < 10$	7	7	8
ecal	track Ecal timing	$< 4\text{ns}$	5	5	5
ecal	2 cluster time diff	$< 2\text{ns}$	8	6	10
physics	momentum asymmetry	< 0.4	14	15	13
physics	e+ track d0	$< 1.5\text{mm}$	7	3	11
event	max shared hits amongst tracks	< 5 shared hits	8	7	8
track	cuts on kink tails	ϕ and λ kink tails	19	9	36

The initial selection requires that a track that missed Layer 1 has a projection to the z location at layer 1 that is less than 1.5 mm from the beam. This ensures that the sample is not overly contaminated by events that passed through the active region but failed to identify a hit. As a result, the core of the distribution sits on the downstream side of the z-axis and reflects the geometric constraints we have imposed. The first cut that is different from the L1L1 dataset is the isolation cut. In this dataset, we apply the same isolation cut to the track that passed through Layer 1, but we apply a slightly different isolation cut for the track that did not pass through layer 1. The isolation in layer 2 is measured and projected

to the target position to be compared with the impact parameter of the track in y at the target. Additional cuts are applied to the tails of the kink distributions for the tracks. The summary of these cuts is made in the Table 7.

TABLE 7: Cuts applied to the kinks in layers 1-3.

Cut	Value
Layer 1: ϕ kink, λ kink	$ 0.0001, 0.002$
Layer 2: ϕ kink, λ kink	$ 0.002, 0.004$
Layer 3: ϕ kink, λ kink	$ 0.002, 0.004$

The uncut kink distributions for the electron with the cut indicated by the red dashed line is shown in Figures 6.3.27, 6.3.28, and 6.3.29.

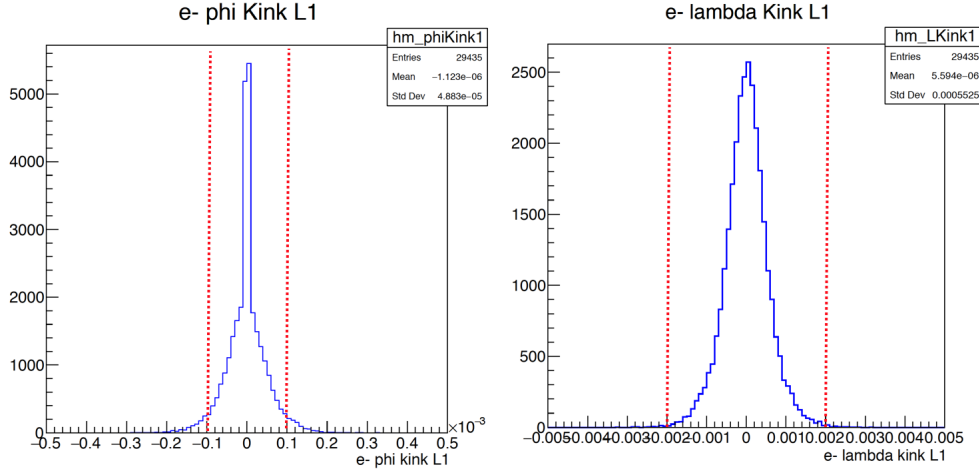


FIG. 6.2.27: The kink distributions for tracks passing through Layer 1. The cut is shown at the red dashed line.

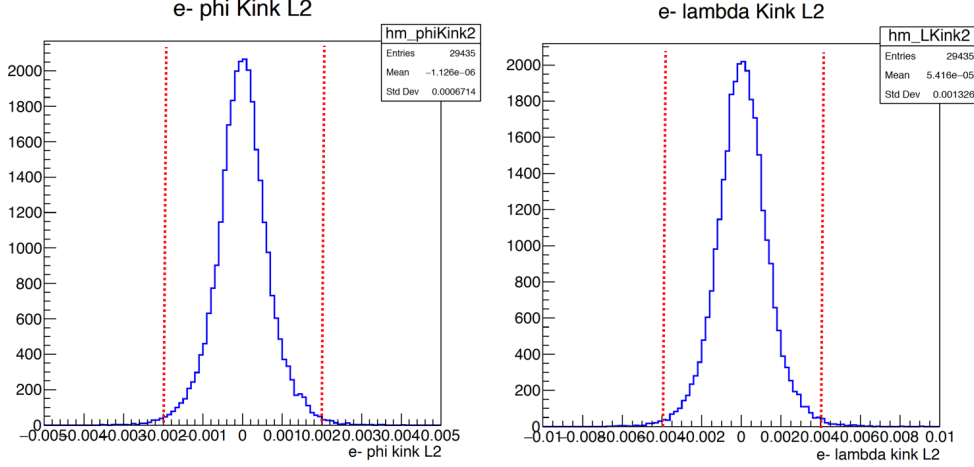


FIG. 6.2.28: The kink distributions for tracks passing through Layer 2. The cut is shown at the red dashed line.

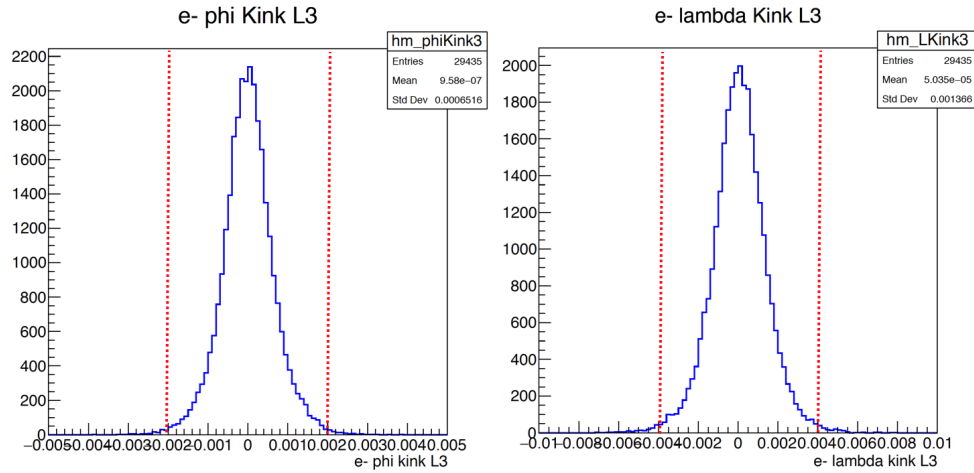


FIG. 6.2.29: The kink distributions for tracks passing through Layer 3. The cut is shown at the red dashed line.

The positron kink distributions look like the electron kink distributions are not shown here. These cuts significantly remove events from the tails and merit further study with the unblinded dataset to increase statistics in understanding cuts. The effects of all the cuts on the reconstructed vertex position distribution are shown in Figure 6.3.30.

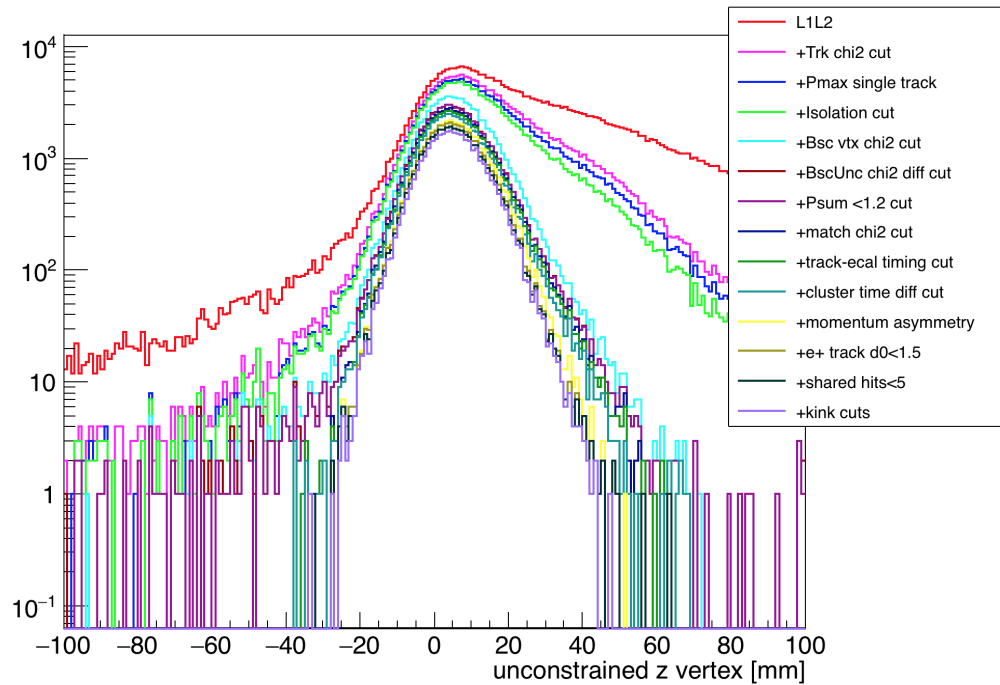


FIG. 6.2.30: The effects of the cuts on the L1L2 dataset on the unconstrained z vertex.

The effects of the cuts on the reconstructed mass distribution are shown in Figure 6.3.31.

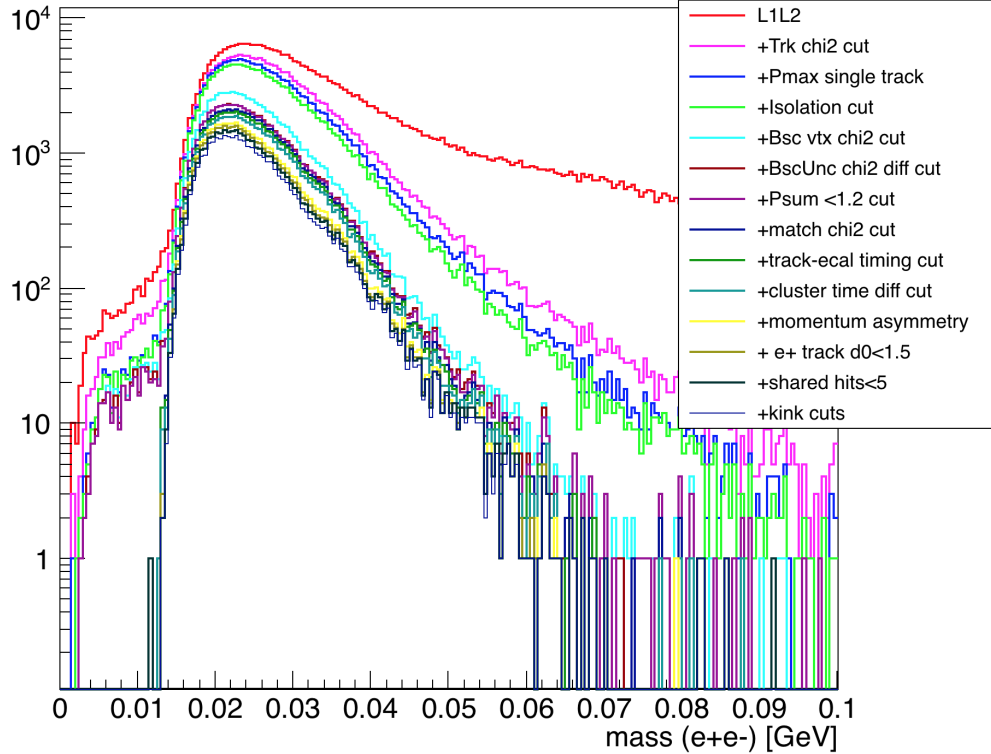


FIG. 6.2.31: The effects of the cuts on the L1L2 dataset on the mass distribution.

This dataset has the tendency to contain more WAB contamination than the L1L1 dataset. In particular, we know from Monte Carlo that positrons are unlikely to have a hit in Layer 1 when the photon in WAB pair produces after the target. Additionally, this sample contains a 5:1 ratio of having an electron versus a positron in the first layer.

Vertex reconstruction efficiency, ϵ_{vtx}

The vertex reconstruction efficiency is calculated again as the ratio of reconstructed versus thrown heavy photon Monte Carlo for a range of masses through fixed ϵ^2 coupling. As shown in Figure 6.3.16, the reconstructed vertex efficiency as a function of z position can be roughly fit with a Crystal Ball function for events that have any track missing the Layer 1 active region. These efficiencies at each mass are fitted with Equation (6.3.4).

$$\begin{aligned}\epsilon_{vtx}(t >= -|\alpha|) &= Ne^{-0.5t^2} \\ \epsilon_{vtx}(t < -|\alpha|) &= NA(B - t)^{-n}\end{aligned}$$

where:

$$\begin{aligned}\alpha &= 0.97 \\ n &= 141.5 \\ t &= \frac{z - z_{mean}}{\sigma} \\ A &= \left(\frac{n}{|\alpha|}\right)^n e^{-0.5|\alpha|^2} \\ B &= \frac{n}{|\alpha|} - |\alpha| \\ N &= \text{amplitude of the Gaussian}\end{aligned}$$

$$Ne^{-0.5\frac{(z - z_{mean})^2}{\sigma^2}} \quad (6.2.4)$$

The parameters of the fit are parameterized as function of mass to find the relations shown in Equation (6.3.5).

$$\begin{aligned}z_{mean} &= -58.89 + 5208.95m - 76469.9m^2 + 386631m^3 \\ \sigma &= 3.05 + 629.99m - 14691.8m^2 + 114123m^3 \\ N &= -0.3125 + 37.0172m - 472.052m^2\end{aligned}$$

The vertex efficiency for vertices with one track missing Layer 1 can be integrated in accordance with Equation (??). For a fixed coupling, the integral can be calculated using various zCut values as shown in Figure 6.3.32.

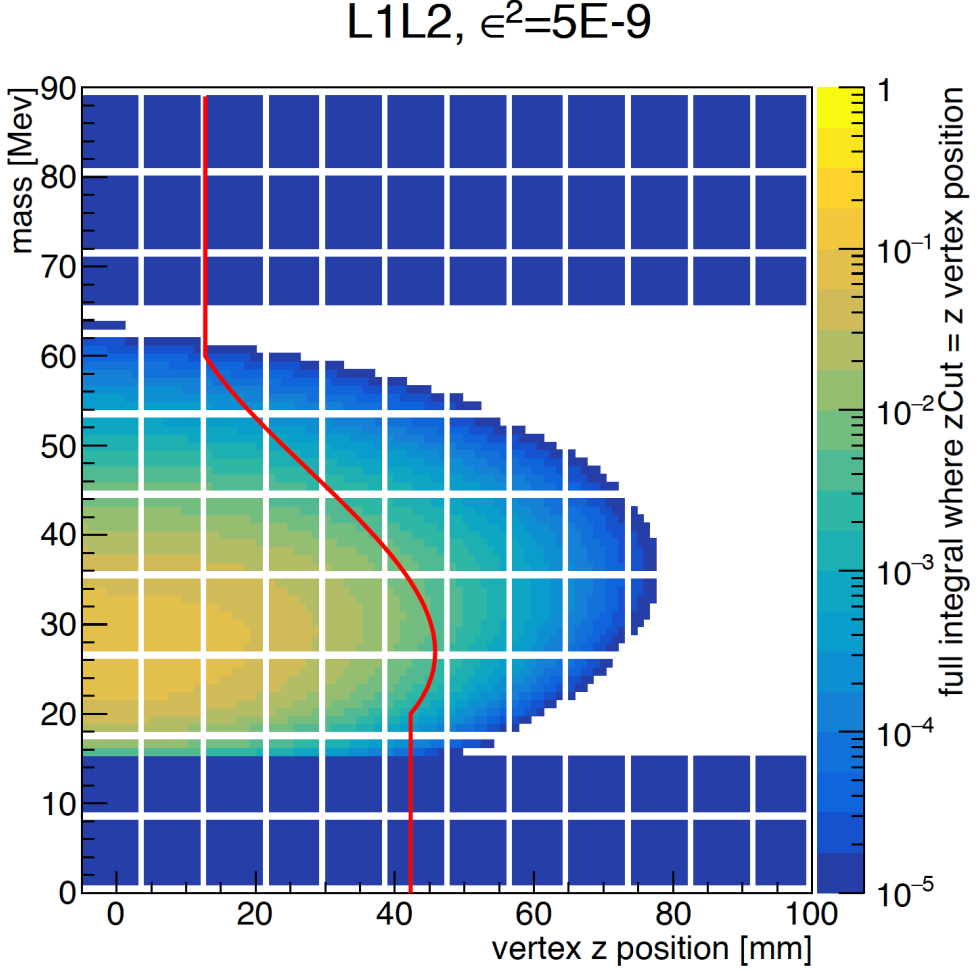


FIG. 6.2.32: The colored value is the value of the full integral from Equation (??) for the L1L2 dataset using the z_{Cut} value on the x-axis. The red line indicates the z_{Cut} value derived in data for 0.5 background events. This z_{Cut} is drawn from the z_{Cut} for the 10 % unblinded data.

As shown in Figure 6.3.32, the current location of the z_{Cut} , if improved by approximately 2-3 mm could improve the reach of the L1L2 dataset. The tails of the z vertex distribution require further studies using the fully unblinded dataset.

Mass resolution

The mass resolution for the L1L2 dataset is obtained by studying A' Monte Carlo, as was the same for the L1L1 dataset. Due to the geometry, the L1L2 dataset improves reach for heavy photons that decay further downstream. The mass resolution is shown in Figure 6.3.33.

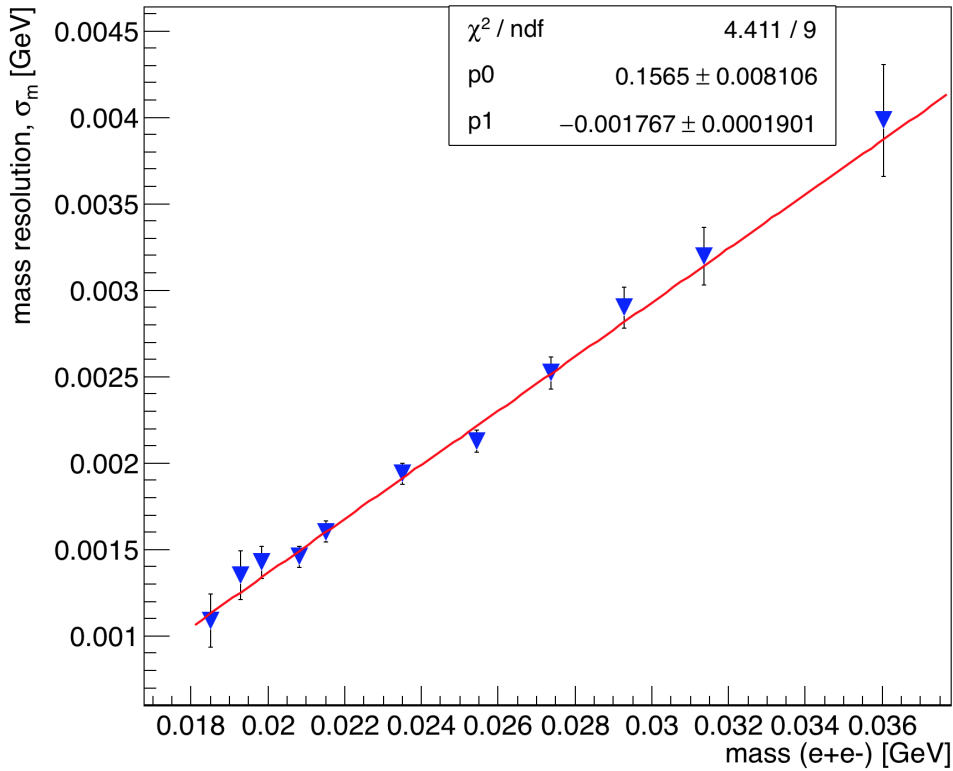


FIG. 6.2.33: The fitted mass residual, or mass resolution, plotted as a function of the measured mass.

The mass resolution for L1L2 decays is noticeably worse than the resolution obtained for the L1L1 dataset.

The fit to the Moller mass distribution in the L1L2 dataset is shown in 6.3.34.

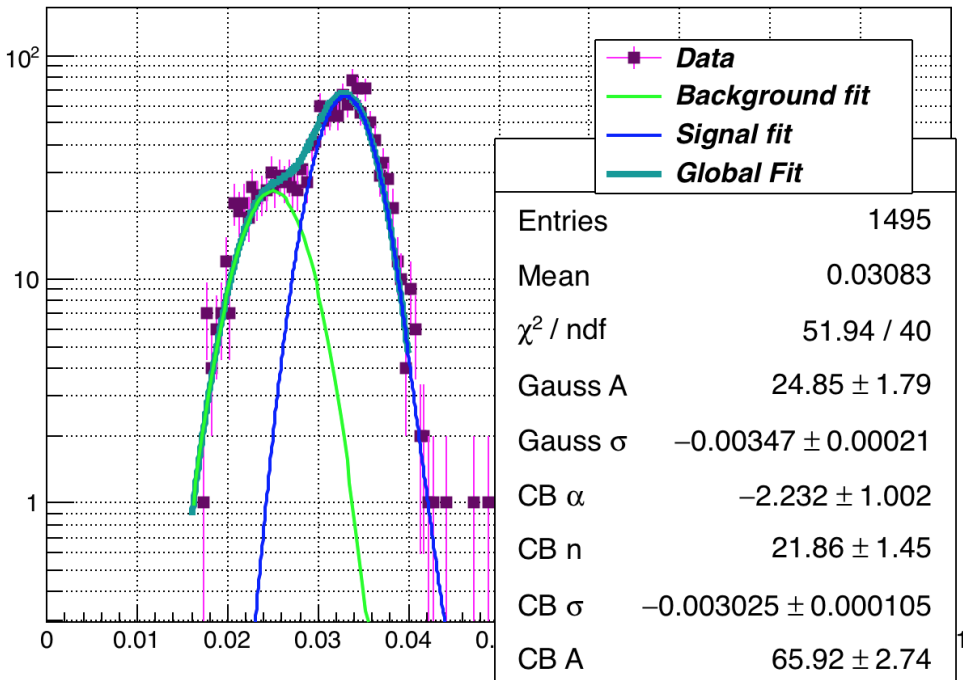


FIG. 6.2.34: The fit to the L1L2 Moller mass distribution in 10% of the data.

The Moller mass peak has a resolution that differs by approximately 2% with the heavy photon Monte Carlo mass resolution, but the low mass background under the front of the peak is significantly higher than was seen in the L1L1 dataset. This low mass background could be increasing due to the lack of precision without a hit in Layer 1 in tracking and could be responsible for the lack of an apparent mass peak in the L2L2 dataset to be discussed in the next section.

Accidentals

The same exercise in studying accidentals in the L1L1 dataset is applied to the L1L2 dataset. By choosing vertices where the time difference between the two clusters is across six beam buckets (time differences greater than 3 ns and less than 9 ns), we observe the vertices produced as a function of mass in Figure 6.3.35.

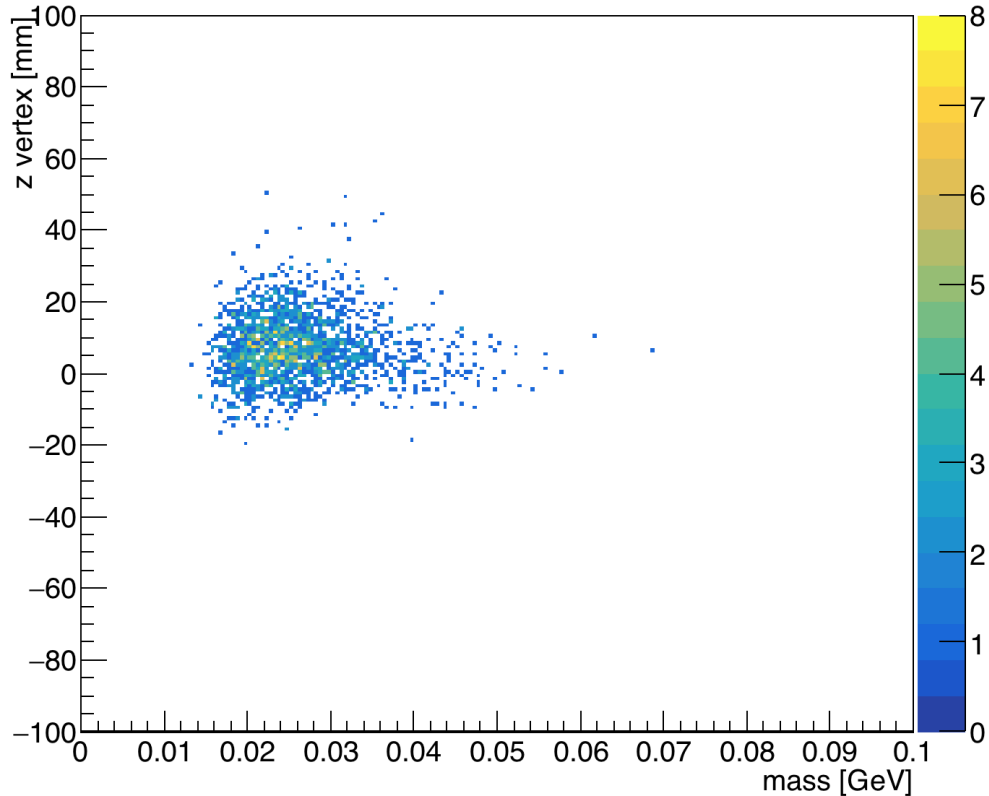


FIG. 6.2.35: The vertices that are produced when the time difference between the two clusters is greater than 3 ns and less than 6 ns. There are 3 approximately high z background events.

As shown in Figure 6.3.35, we see that we have obtained approximately 3 high z background events across the six beam buckets. Again, this allows for the possibility to have 1 ± 0.6 background events before in the events selected of the unblinded 10 % dataset. This rate is seemingly higher than for the L1L1 dataset due to the significantly decreased statistics in the dataset and will require further study with unblinding.

Projected reach

The high z tails of the z vertex distribution as a function of mass can be seen for both datasets where the positron and electron have a Layer 1 hit separately in Figure 6.3.36.

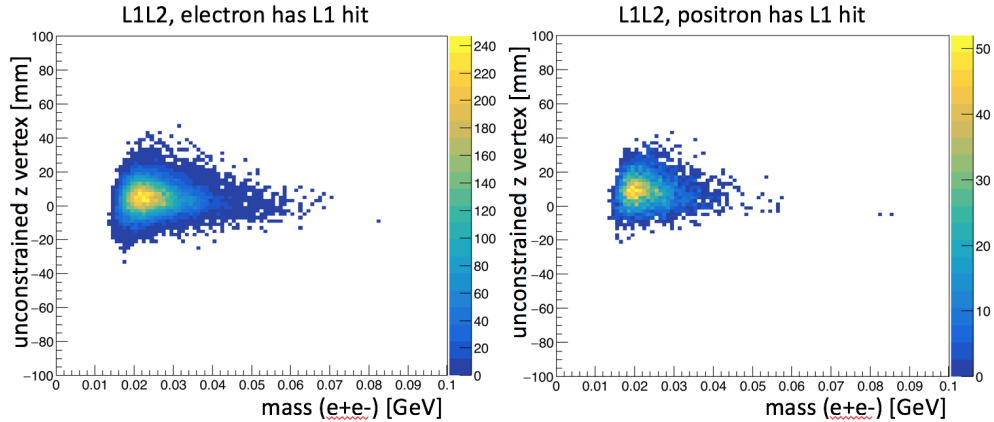


FIG. 6.2.36: The final z vertex distribution as a function of mass for the L1L2 datasets where the electron has a Layer 1 hit (shown on the left) and the positron has a Layer 1 hit (shown on the right) separately.

Because the high z tails for both datasets are similar, the zCut is obtained when we combine these datasets. After unblinding, it could be necessary to tune cuts separately and may merit a separate zCut. For now, the final z vertex distribution as a function of mass can be seen in Figure 6.3.37.

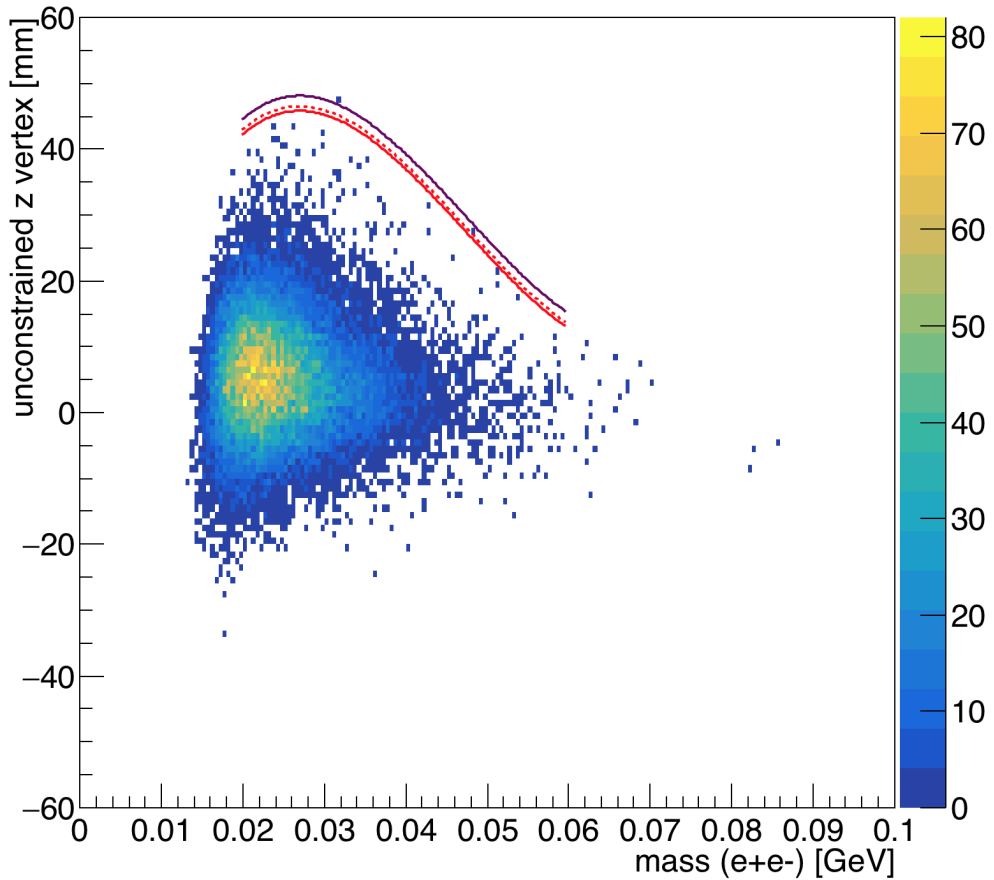


FIG. 6.2.37: Reconstructed z vertex as a function of mass for the L1L2 dataset with the first layer of the SVT at 0.5 mm from the beam. The solid red line indicates the zCut found for 10% of the data (unblinded), and the dashed red line indicates the limit at which events have a quantile greater than 0.5 with respect to the predicted background model. The purple line shows where the projected zCut will be for the full dataset after unblinding.

The corresponding reach for the 0.5 mm L1L2 dataset is shown in Figure 6.3.38.

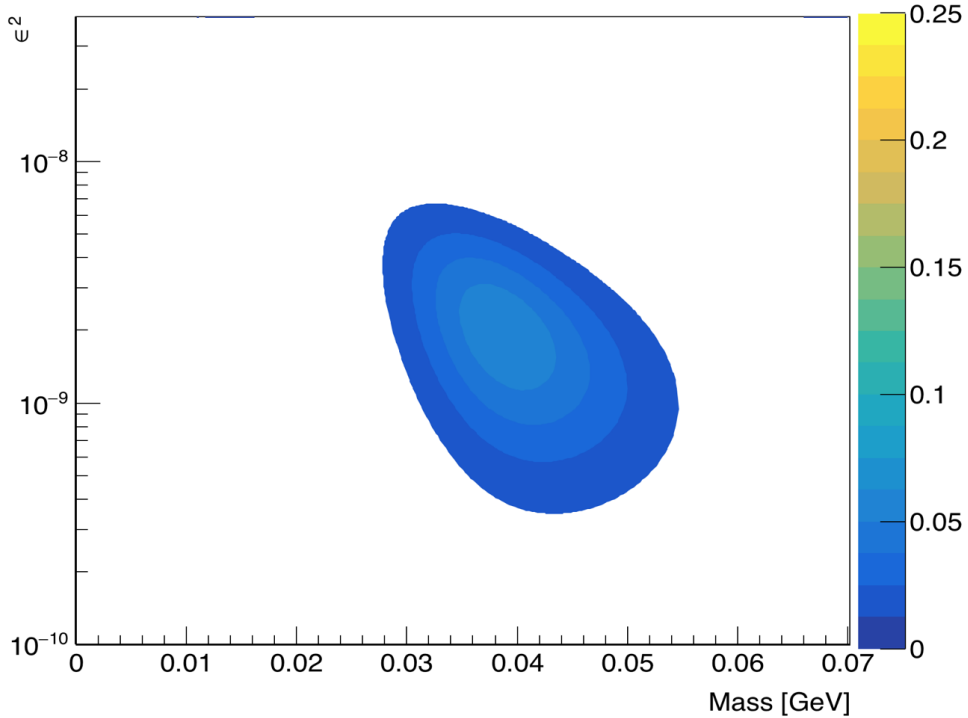


FIG. 6.2.38: The expected signal yield for the full 0.5 mm 100% dataset with L1L2 type events. This uses the zCut projection shown in Figure 6.3.37.

The reach distribution for the L1L2 dataset appears to favor weakly coupled larger masses.

6.2.3 L2L2

The L2L2 dataset consists of vertices produced when tracks do not pass through Layer 1 and their projections back to Layer 1 are within 1.5 mm of the beam (outside the active silicon region). This dataset will most likely require the most work to remove the background events, and preliminary studies with the small number of statistics have been unsuccessful.

Cuts

The general cuts applied to the L2L2 dataset, after first requiring that track projections do not extend to the active region of Layer 1, are listed in Table 8.

TABLE 8: Cuts applied to the L2L2 datasets.

Cut type	Cut	Cut Value	%killed	%killed core	%killed tails
track	Fit quality	track $\chi^2 < 30$	44	66	44
track	Max track momentum	$P_{trk} < 75\%E_{beam}$	15	14	15
track	Isolation		22	34	22
vertex	beamspot constraint	$bsc\chi^2 < 10$	47	36	47
vertex	beamspot - unconstrained	$bsc\chi^2 - unc\chi^2 < 5$	18	0	19
vertex	maximum P_{sum}	$< 115\%E_{beam}$	1	6	1
ecal	Ecal SVT matching	$\chi^2 < 10$	30	73	29
ecal	track Ecal timing	$< 4\text{ns}$	7	0	8
ecal	2 cluster time diff	$< 2\text{ns}$	8	0	8
physics	momentum asymmetry	< 0.4	4	0	4
physics	e+ track d0	$< 1.5\text{mm}$	21	33	21
event	max shared hits amongst tracks	< 4 shared hits	21	50	21

The geometric acceptance of the cuts in the L2L2 dataset leave a core fraction of background events well beyond the target at approximately 30 mm downstream. The only modifications to previously applied cuts are that both tracks use a modified isolation cut by looking at the isolation at Layer 2 and the tracks do not share 4 hits with any other track in the event. The kink cuts appeared to not remove events from this dataset, but other options will need to be explored after unblinding.

Vertex reconstruction efficiency, ϵ_{vtx}

The L2L2 dataset is most efficient for long-lived heavy photons with detached vertices farther downstream than any of the other datasets. The efficiency in terms of mass and z vertex position is fit using the Crystal Ball function as described in Equation (6.3.4). The parameters of fit as a function of mass are shown in Equation (6.3.5).

$$\begin{aligned}
 N &= -0.3623 + 30.88m - 374.7m^2 \\
 z_{mean} &= -71.7603 + 7733.51m - 131569m^2 + 827080m^3 \\
 \sigma &= -4.058 - 813m - 8947m^2
 \end{aligned}$$

If the backgrounds can be removed from the L2L2 dataset, then the zCut for this dataset can essentially cover the entire range of z values to the first layer. If some background events at lower z values cannot be removed, then it may still be possible to recover most of the efficiency of this dataset by optimizing the zCut based on the L2L2 vertex reconstruction efficiency. The efficiency for these events turns on downstream. One can propose potential zCuts where the turn on of the efficiency passes various efficiency thresholds. The corresponding possible zCut values as the efficiency surpasses 2 %, 5 %, and 10 % are shown in Figure 6.3.39.

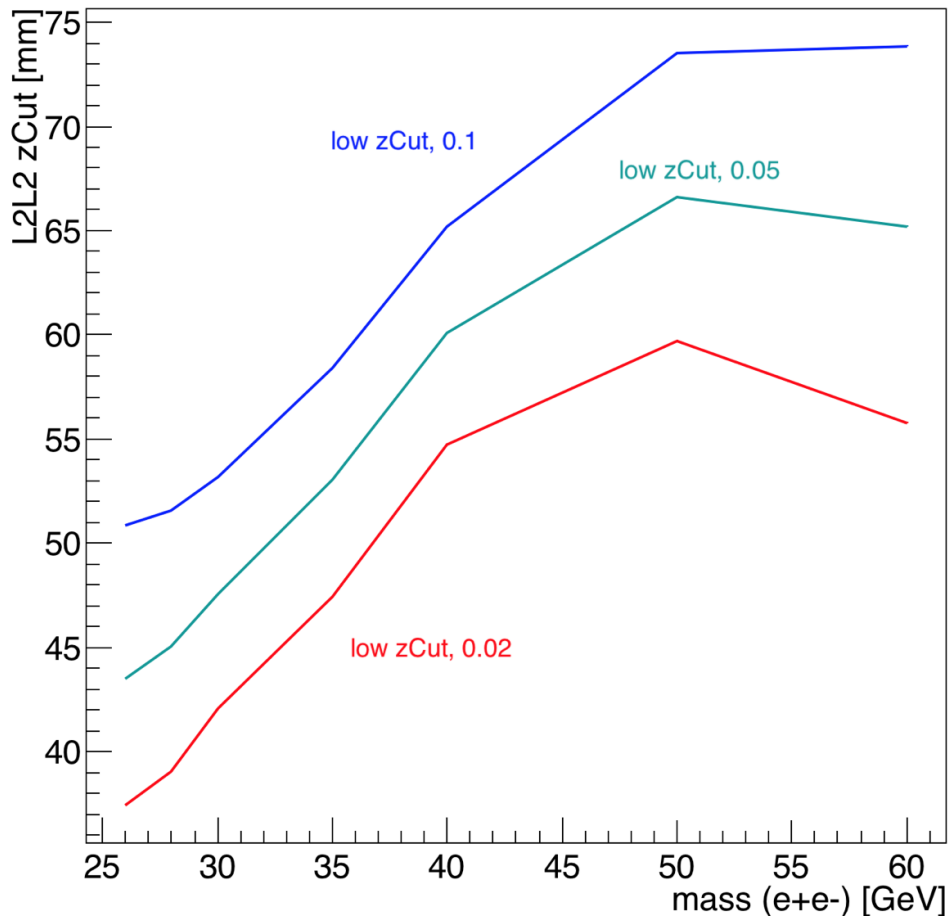


FIG. 6.2.39: This is the proposed zCut for the L2L2 dataset based on the efficiency curves. The three lines represent the turn on efficiency for the L2L2 dataset for the efficiency values corresponding to 2%, 5%, and 10%.

In order to fully realize the contribution of the L2L2 dataset to the overall reach, the high z background must be removed.

Mass resolution

As we fit the residual heavy photon reconstructed masses for the L1L1 and L1L2 datasets, we apply the same methodology to the L2L2 dataset. Reconstructed masses are shown in the Figure 6.3.40.

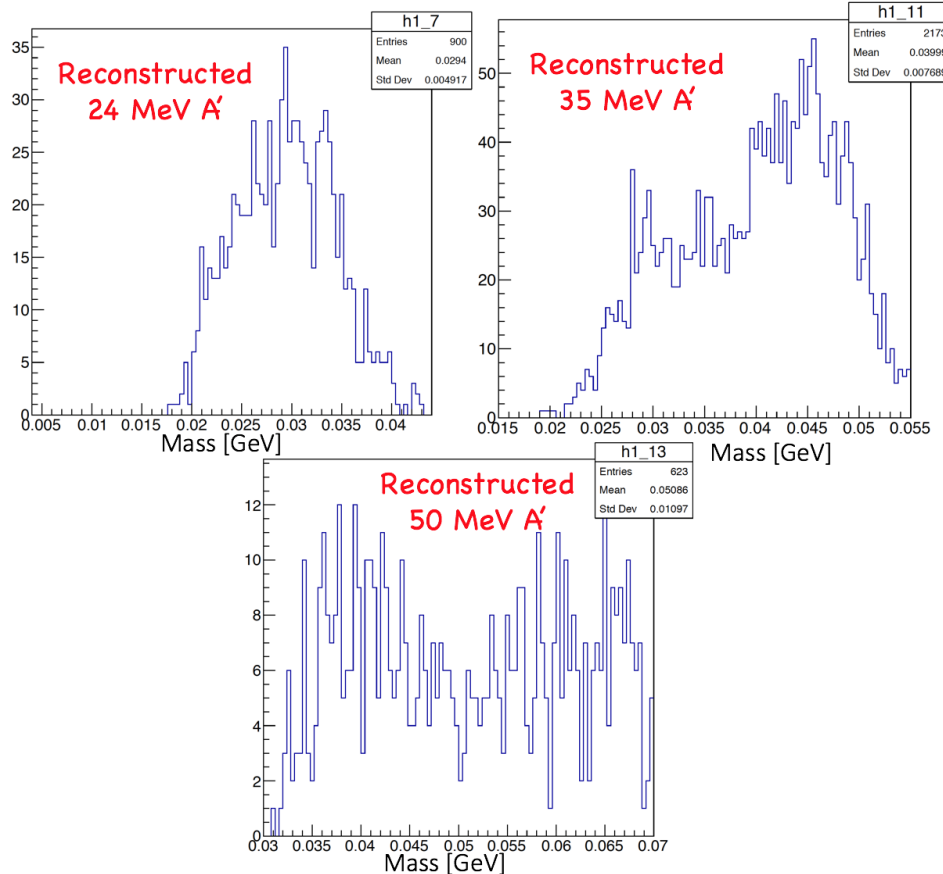


FIG. 6.2.40: The reconstructed heavy photon masses from Monte Carlo for the L2L2 dataset. Not only do the masses appear to reconstruct the wrong place, but the width of distributions indicates that we may not have the resolution to see a signal at all.

As shown in Figure 6.3.40, in order to use the L2L2 dataset, we must improve our mass resolution. Not only are we unable to reconstruct the masses in the correct location, but we appear to lack the resolution to resolve a mass without Layer 1 at all. If we can understand and address this problem then it may be possible to recover some use of the L2L2 dataset, but without this improvement, we will not be able to reliably reconstruct any heavy photons in the event sample. For further reach calculations, the mass resolution will take the optimistic scenario and utilize the L1L2 mass resolution (in the scenario that we can solve the problem

with the L2L2 mass resolution).

Accidentals

When looking at accidentals, the same strategy was applied as previously mentioned to choose out of time events. In total, 10 events across the six beam buckets remain. This could indicate that in the dataset as selected, we may expect 3.3 ± 1 event. This rate is higher than other accidental rates, but this may also change when the L2L2 selection criteria for general vertex events is improved.

Projected reach

The reconstructed z vertex versus the mass for the L2L2 dataset is shown in its current state in Figure 6.3.41.

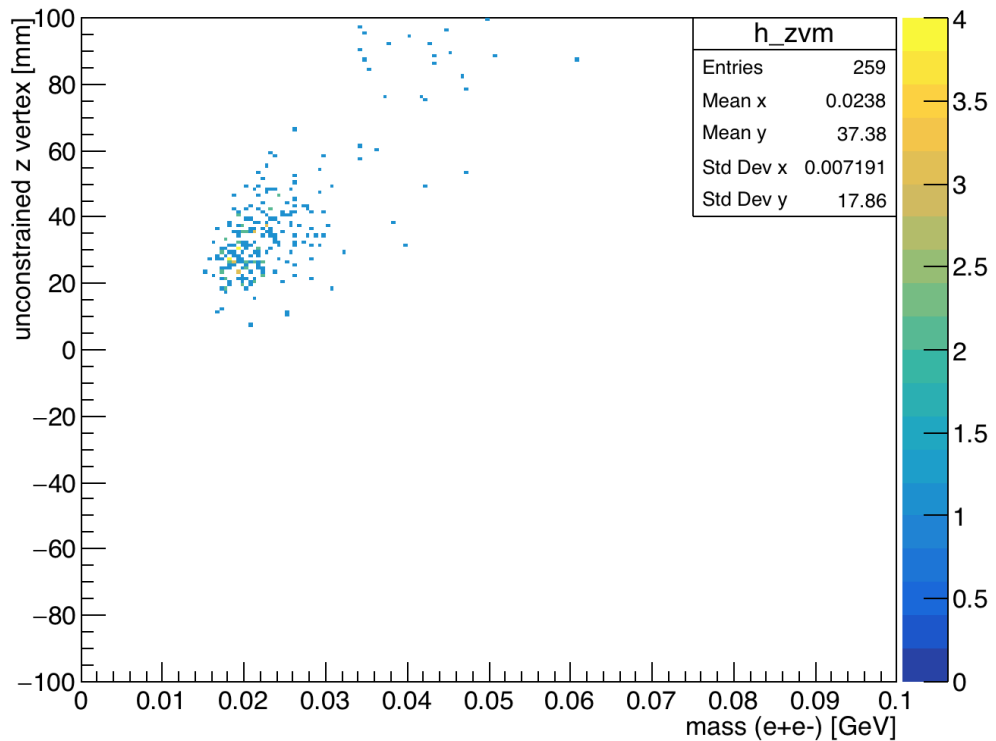


FIG. 6.2.41: Reconstructed z vertex as a function of mass for the L2L2 dataset with the first layer of the SVT at 0.5 mm from the beam.

The events reconstructed in the current L2L2 dataset are a background that must be fully characterized when unblinding. Assuming that we can remove the high z background

and integrating from the target position to Layer 1, we could anticipate the upper limit improvement by adding the L2L2 dataset.

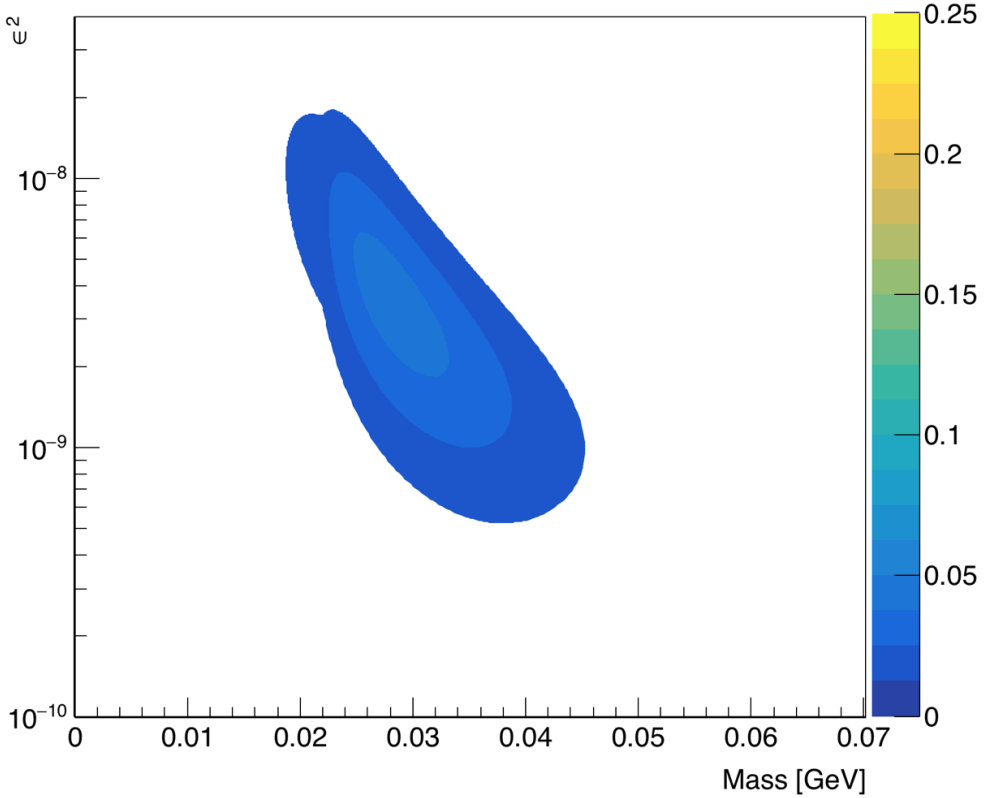


FIG. 6.2.42: The expected signal yield for the L2L2 0.5 mm 100% dataset. This is an upper limit estimate that assumes we can remove the background in the L2L2 dataset.

The L2L2 dataset improves the reach somewhat in the region of 20-40 MeV masses. While the efficiency of the L2L2 dataset improves at larger z vertices, the heavy photon production begins to suppress in this region.

6.3 SVT AT 1.5 MM FROM THE BEAM

The 1.5 mm datasets consist of the data that was taken over approximately 0.5 beam days with the first layer of the SVT at 1.5 mm from the beam. Because this run was the engineering run, the beam position and stability had to be fully understood before moving the SVT in to its nominal position at 0.5 mm from the beam.

6.3.1 L1L1

The L1L1 dataset in the 1.5 mm data includes vertices reconstructed from pairs of tracks

that have hits in Layer 1 of the SVT. Due to the SVT opening being larger, the acceptance favors larger heavy photon masses. The SVT has also lower rates in Layer 1 when compared to the 0.5 mm dataset.

Cuts

The cuts applied to the L1L1 dataset are shown in Table 9.

TABLE 9: Cuts applied to the L1L1 datasets with the SVT at 1.5mm.

Cut type	Cut	Cut Value	%killed	%killed core	%killed tails
track	Fit quality	track $\chi^2 < 30$	37	22	87
track	Max track momentum	$P_{trk} < 75\%E_{beam}$	6	6	19
track	Isolation		2	1	15
vertex	beamspot constraint	$bsc\chi^2 < 10$	23	21	81
vertex	beamspot - unconstrained	$bsc\chi^2 - unc\chi^2 < 5$	12	12	27
vertex	maximum P_{sum}	$< 115\%E_{beam}$	0	0	2
ecal	Ecal SVT matching	$\chi^2 < 10$	3	3	58
ecal	track Ecal timing	$< 4\text{ns}$	5	5	7
ecal	2 cluster time diff	$< 2\text{ns}$	4	4	13
physics	momentum asymmetry	< 0.4	12	12	48
physics	e+ track d0	$< 1.5\text{mm}$	0	0	4
event	max shared hits amongst tracks	< 5 shared hits	12	12	20

The cuts are the same as those applied to the 0.5 mm dataset with similar effect.

Vertex reconstruction efficiency, ϵ_{vtx}

The efficiency of the 1.5 mm data was obtained using the same methodology as the 0.5 mm data. Using heavy photon simulation at fixed masses, one can compare the reconstructed heavy photons as a function of vertex position for all datasets. The reconstructed vertex efficiency at the target for the L1L1 dataset is scaled to 1, and the L1L2 and L2L2 datasets are scaled, accordingly. The resulting efficiency effect can be seen in Figure 6.4.1.

1.5mm, A' mass = 35 MeV

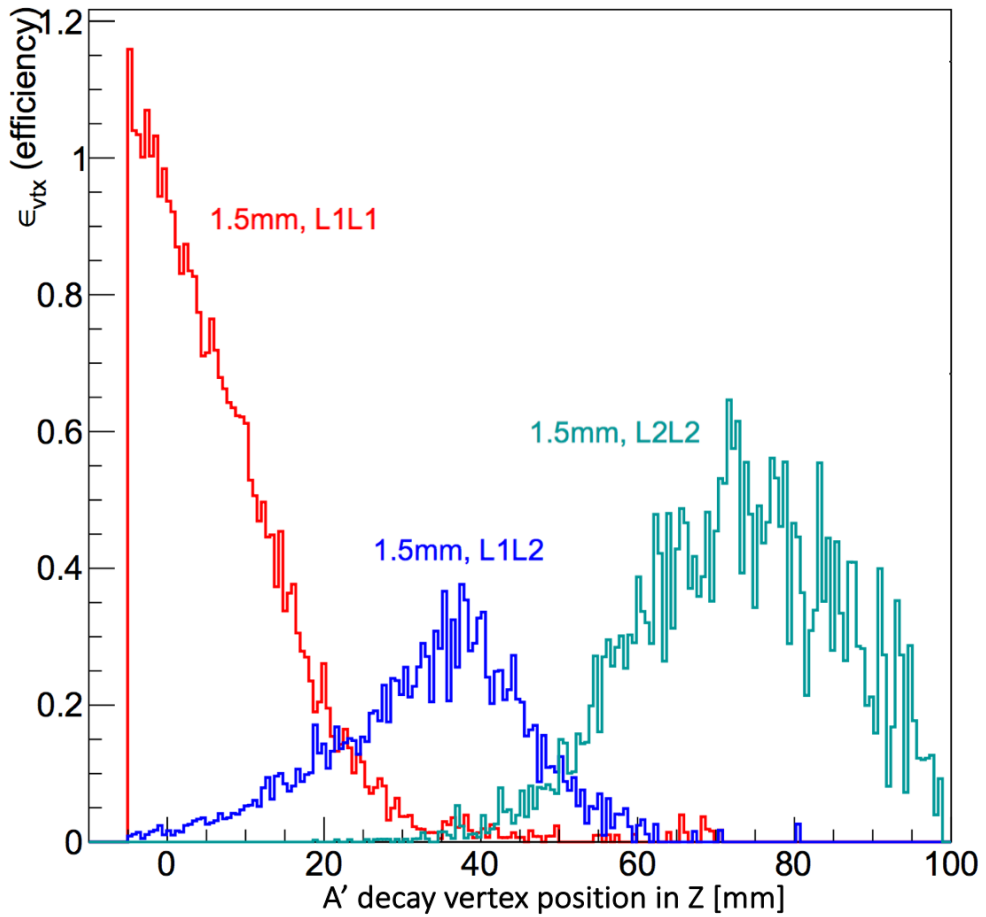


FIG. 6.3.1: 35 MeV reconstruction efficiency versus the vertex position.

The L1L1 efficiency for each mass was fit using Equation (6.4.1).

$$\epsilon_{vtx} = \exp(p_0 z^3 + p_1 z^2 + p_2 z + p_3) \quad (6.3.1)$$

The parameters of Equation (6.4.1) are then studied as a function of mass as shown in Equation (6.4.1).

$$\begin{aligned}
p_0 &= 1.034E - 5 - 1.2E - 7m \\
p_1 &= -0.00324 + 0.00016m \\
p_2 &= 0.0412 - 0.0037m + 4.11E - 5m^2 \\
p_3 &= -0.1348 + 0.000784m
\end{aligned}$$

The vertex reconstruction efficiency can then be applied to the integral in Equation (??). The value of the integral yields the fraction of measured heavy photon signal events. For the L1L1 dataset, the zMax value is 100 mm, and the integral values for various zCuts is shown in Figure 6.4.2.

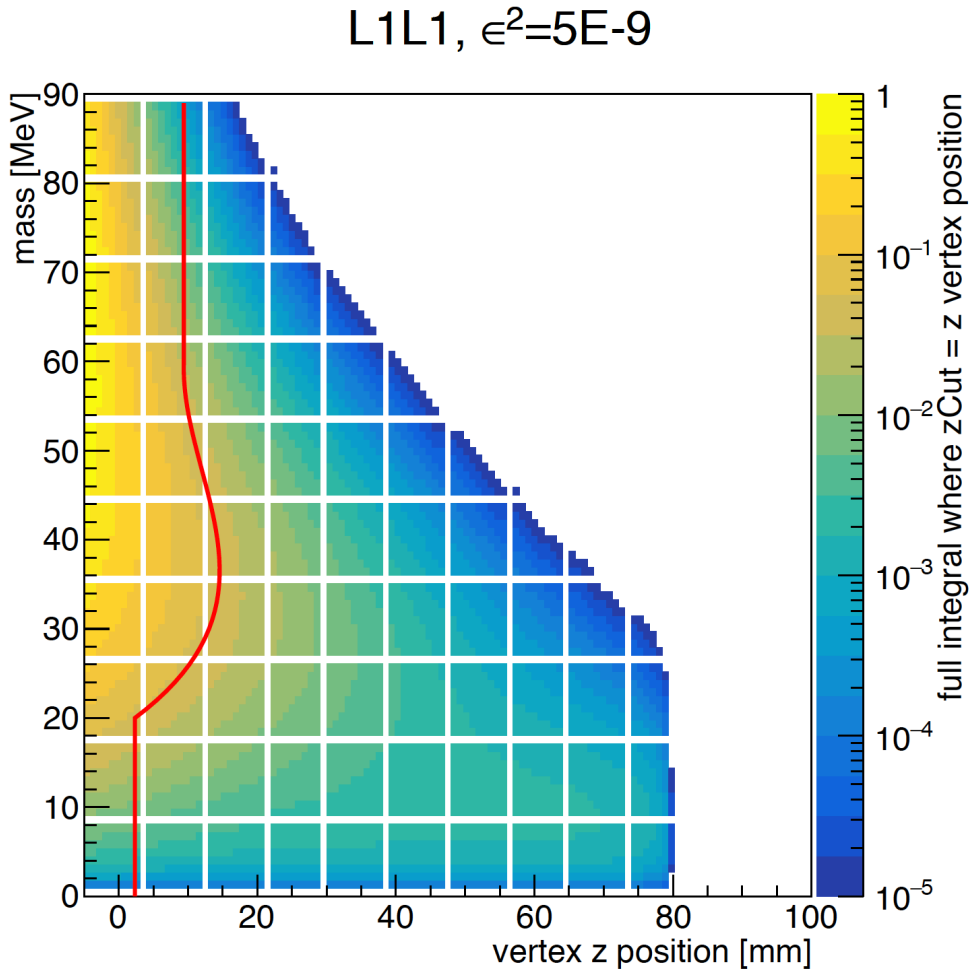


FIG. 6.3.2: The colored value is the value of the full integral from Equation ?? for the L1L1 1.5 mm dataset using the zCut value on the x-axis. The red line indicates the zCut value derived in data for 0.5 background events. The zCut shown is for the 10% unblinded data.

We can see the full integral value for various couplings across a range of masses in the dataset in Figure 6.4.3.

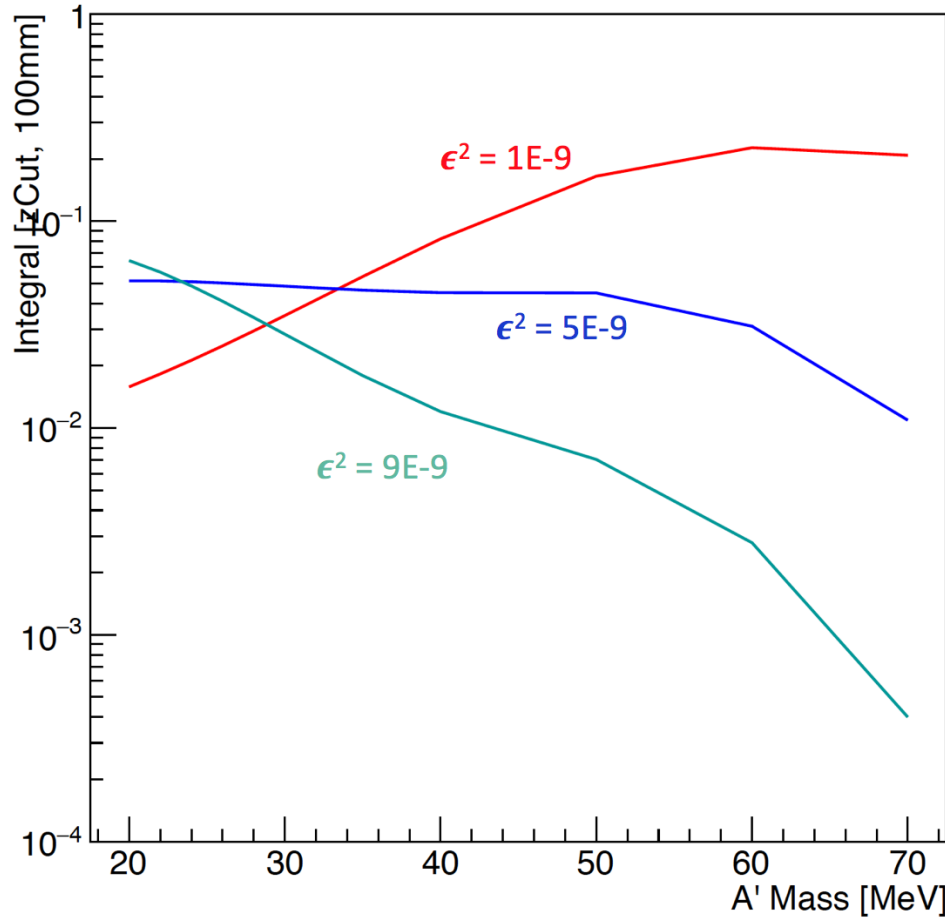


FIG. 6.3.3: For the measured zCut value in the 10% of the data, the corresponding integral value for various couplings across a range of masses is shown.

The mass resolution has been shown previously to be nearly the same between 0.5 mm and 1.5 mm datasets.

Accidentals

When counting the reconstructed vertices having cluster time differences between 3 and 9 ns apart, no high z events were produced. It's possible that the statistics are too low to say with any certainty that we will not see any when unblinding, but this does seem to indicate that we should see no accidental events in the 10% unblinded sample currently studied.

Projected reach

The resultant vertex distribution as a function of mass is shown in Figure 6.4.4.

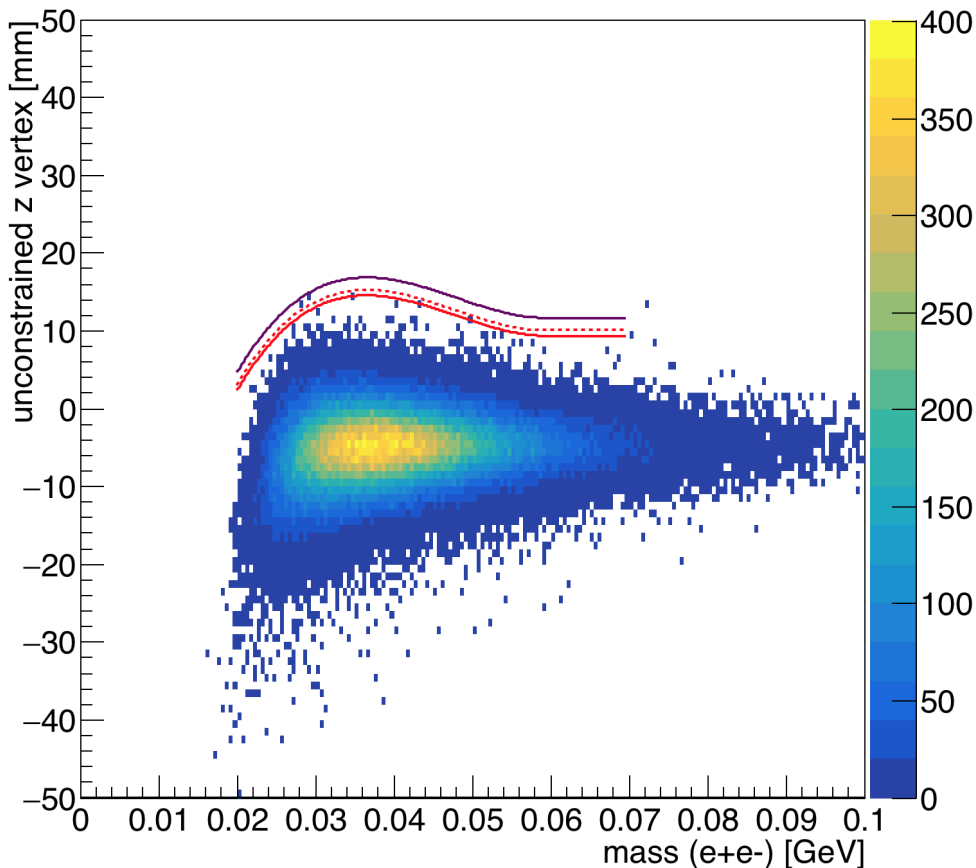


FIG. 6.3.4: Reconstructed z vertex as a function of mass for the L1L1 dataset with the first layer of the SVT at 1.5 mm from the beam. The solid red line indicates the zCut found for 10% of the data (unblinded), and the dashed red line indicates the limit at which events have a quantile greater than 0.5 with respect to the predicted background model. The purple line shows where the projected zCut will be for the full dataset after unblinding.

The reach projections for the 1.5 mm dataset include the statistics of the 0.5 mm dataset in the value of N_{bin} as described by Equation ???. The reach projection for the L1L1 1.5 mm dataset is shown in Figure 6.4.5.

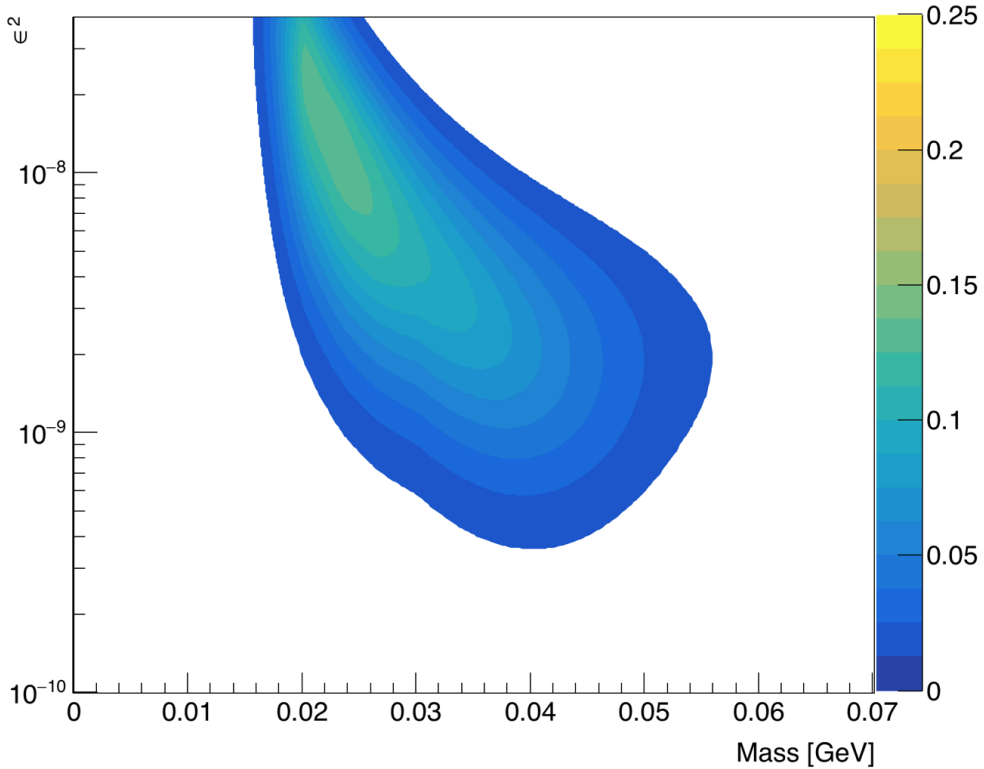


FIG. 6.3.5: The expected signal yield for the full 100% dataset with L1L1 1.5 mm data.

Here we see that the reach is most sensitive to largely coupled, smaller mass decays due to the larger opening of the SVT.

6.3.2 L1L2

The following section describes the data set where one track misses Layer 1 of the SVT and its track projection back to Layer 1 is within 2.5 mm of the beam such that the track does not extrapolate to the active region of the silicon.

Cuts

The cuts applied to the L1L2 dataset with the first layer of the SVT at 1.5 mm is shown in Table 10.

TABLE 10: Cuts applied to the L1L2 datasets with the SVT at 1.5 mm.

Cut type	Cut	Cut Value	%killed	%killed core	%killed tails
track	Fit quality	track $\chi^2 < 30$	23	11	47
track	Max track momentum	$P_{trk} < 75\%E_{beam}$	8	7	12
track	Isolation		4	2	10
vertex	beamspot constraint	$bsc\chi^2 < 10$	29	20	62
vertex	beamspot - unconstrained	$bsc\chi^2 - unc\chi^2 < 5$	12	11	22
vertex	maximum P_{sum}	$< 115\%E_{beam}$	0	0	0
ecal	Ecal SVT matching	$\chi^2 < 10$	5	5	7
ecal	track Ecal timing	$< 4\text{ns}$	5	5	5
ecal	2 cluster time diff	$< 2\text{ns}$	6	5	9
physics	momentum asymmetry	< 0.4	14	13	16
physics	e+ track d0	$< 1.5\text{mm}$	6	5	16
event	max shared hits amongst tracks	< 5 shared hits	6	6	6
track	cuts on kink tails	ϕ and λ kink tails	22	8	74

The cuts applied to the L1L2 dataset may require a similar optimization to eliminate backgrounds as that required of the dataset for the 0.5 mm. Namely, that, it may be necessary to separate the dataset for events where the positron versus the electron is the first to leave a hit in Layer 1. For the moment, the same cuts are used as the 1.5 mm dataset has generally lower backgrounds than that seen in the 0.5 mm dataset.

Vertex reconstruction efficiency, ϵ_{vtx}

The vertex reconstruction efficiency is fit for each simulated heavy photon mass using a Crystal Ball function as described in Equation (6.3.4). The parameters of the fit can be described as a function of mass as shown in Equation (6.4.2).

$$\begin{aligned} z_{mean} &= -64.13 + 3.97m - 0.033m^2 \\ \sigma &= 8.166 + 0.062m \\ N &= 0.12 + 0.0153m - 0.00023m^2 \end{aligned}$$

Having fully characterized the vertex reconstruction efficiency in terms of mass and z

position for the L1L2 dataset, one can observe the integral value from Equation (??) as a function $zCut$ and mass as shown in Figure 6.4.6 where $zMax$ is 80 mm due to acceptance.

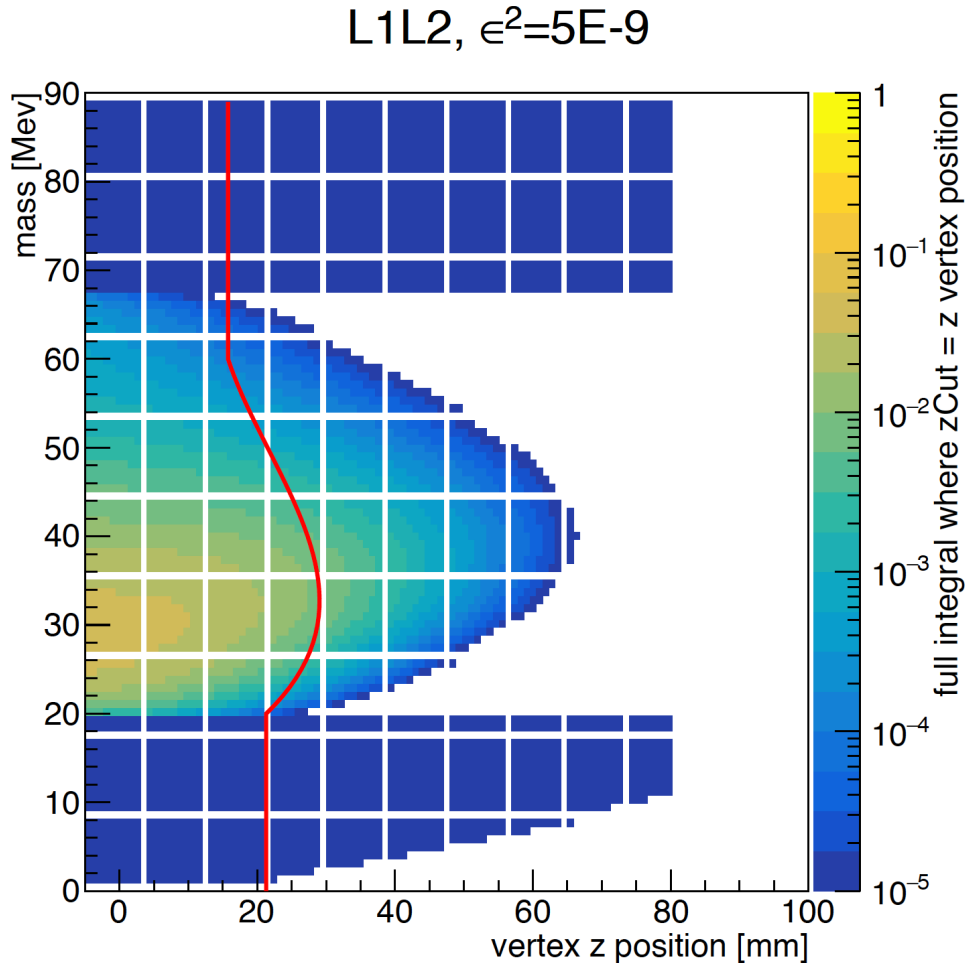


FIG. 6.3.6: This plot, for fixed coupling ϵ^2 , shows the fraction of signal events that will be measured as a function of the integral using the vertex position along the x-axis as the $zCut$. The red line indicates the position of the $zCut$ as found for the 10% sample.

The red line shown in Figure 6.4.6 shows where the $zCut$ value lies that was obtained for the L1L2 dataset. The fraction of events is significantly less by an approximate order of magnitude when compared to the L1L1 dataset, but the $zCut$ seems well optimized to maintain reach.

Accidentals

No accidental high z background events were identified when selecting the out of time events using the methods discussed previously.

Projected reach

The final vertex distribution as a function of mass is shown in Figure 6.4.7.

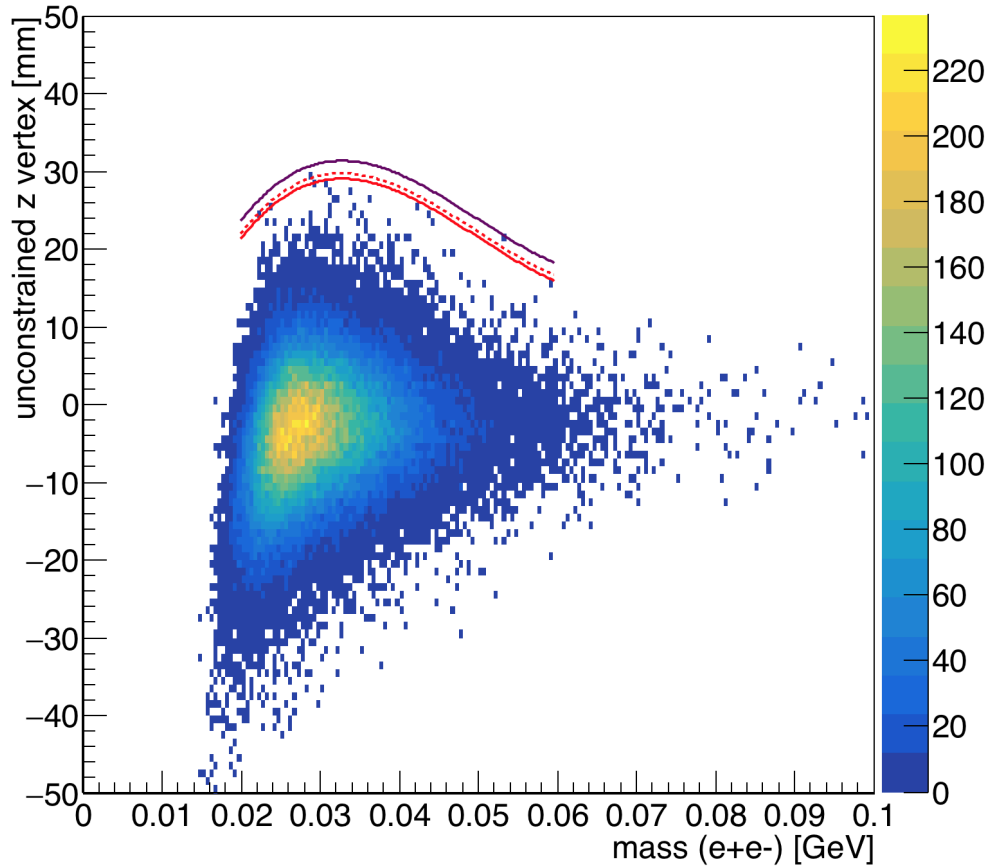


FIG. 6.3.7: Reconstructed z vertex as a function of mass for the L1L2 dataset with the first layer of the SVT at 1.5 mm from the beam. The solid red line indicates the zCut found for 10% of the data (unblinded), and the dashed red line indicates the limit at which events have a quantile greater than 0.5 with respect to the predicted background model. The purple line shows where the projected zCut will be for the full dataset after unblinding.

Using the zCut shown in Figure 6.4.7, we can calculate the expected signal reach for the L1L2 dataset. The reach is shown in Figure 6.4.8.

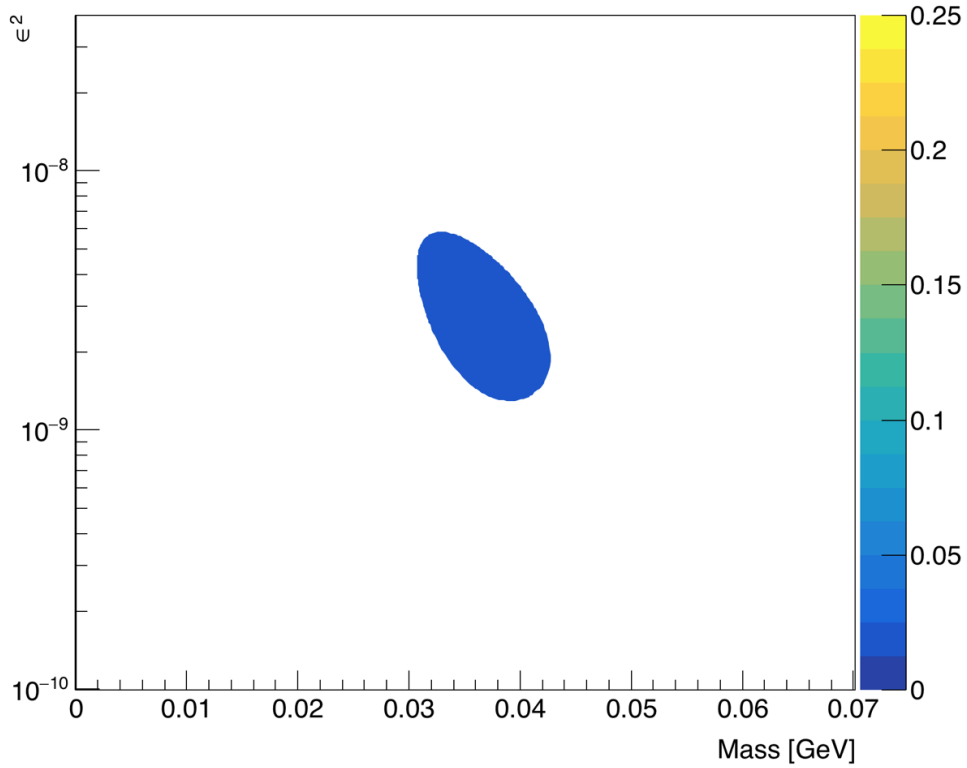


FIG. 6.3.8: The expected signal yield for the full 100% dataset with the L1L2 1.5 mm data.

The L1L2 dataset favors higher masses than the L1L1 dataset and has the highest yield in the relatively central region of the coupling reach for the 2015 run.

6.3.3 L2L2

The following section discusses the events having no hit in Layer 1 of the 1.5 mm dataset. An additional requirement was made that the tracks must not project back to the active region of the Layer 1 silicon in order to avoid contamination by events with the Layer 1 inefficiency.

Cuts

The cuts applied to the L2L2 dataset are shown in Table 11.

TABLE 11: Cuts applied to the L2L2 datasets with the SVT at 1.5 mm.

Cut type	Cut	Cut Value	%killed	%killed core	%killed tails
track	Fit quality	track $\chi^2 < 30$	29	11	39
track	Max track momentum	$P_{trk} < 75\%E_{beam}$	10	8	12
track	Isolation		5	2	8
vertex	beamspot constraint	$bsc\chi^2 < 10$	26	16	35
vertex	beamspot - unconstrained	$bsc\chi^2 - unc\chi^2 < 5$	10	8	14
vertex	maximum P_{sum}	$< 115\%E_{beam}$	1	1	1
ecal	Ecal SVT matching	$\chi^2 < 10$	11	8	14
ecal	track Ecal timing	$< 4\text{ns}$	6	6	6
ecal	2 cluster time diff	$< 2\text{ns}$	7	6	7
physics	momentum asymmetry	< 0.4	3	2	4
physics	e+ track d0	$< 1.5\text{mm}$	9	7	12
event	max shared hits amongst tracks	< 4 shared hits	20	20	20

The cuts are the same as those applied to the data in the 0.5 mm L2L2 dataset. This dataset has significantly more statistics that needs to be studied and may complement the analysis on the 0.5 mm high z background data.

Vertex reconstruction efficiency, ϵ_{vtx}

The vertex reconstruction efficiency for the L2L2 dataset was fit at each simulated heavy photon mass using the Crystal Ball function in Equation (6.3.4). The parameters are characterized as a function of mass in Equation (6.4.2).

$$\begin{aligned} z_{mean} &= -45.49 + 5.25m - 0.052m^2 \\ \sigma &= 7 + 0.104m \\ N &= -0.89 + 0.074m - 0.000995m^2 \end{aligned}$$

The zMax for this dataset is 100 mm as the events can be reasonably reconstructed near Layer 1.

Accidentals

The out of time events as discussed previously were selected in order to understand the accidental rate. No accidental events were clearly identified, although some work is still necessary to understand the high z background when unblinding the dataset and optimizing the zCut.

Projected reach

The L2L2 dataset is unique from other datasets in that it is most efficient at large z . Because of this geometric effect, we can identify and consider how the zCut changes at the low end of the efficiency as we move to large z by proposing cuts at the 2%, 5%, and 10% efficiency values. The corresponding zCut with this possibility is shown in Figure 6.4.9.

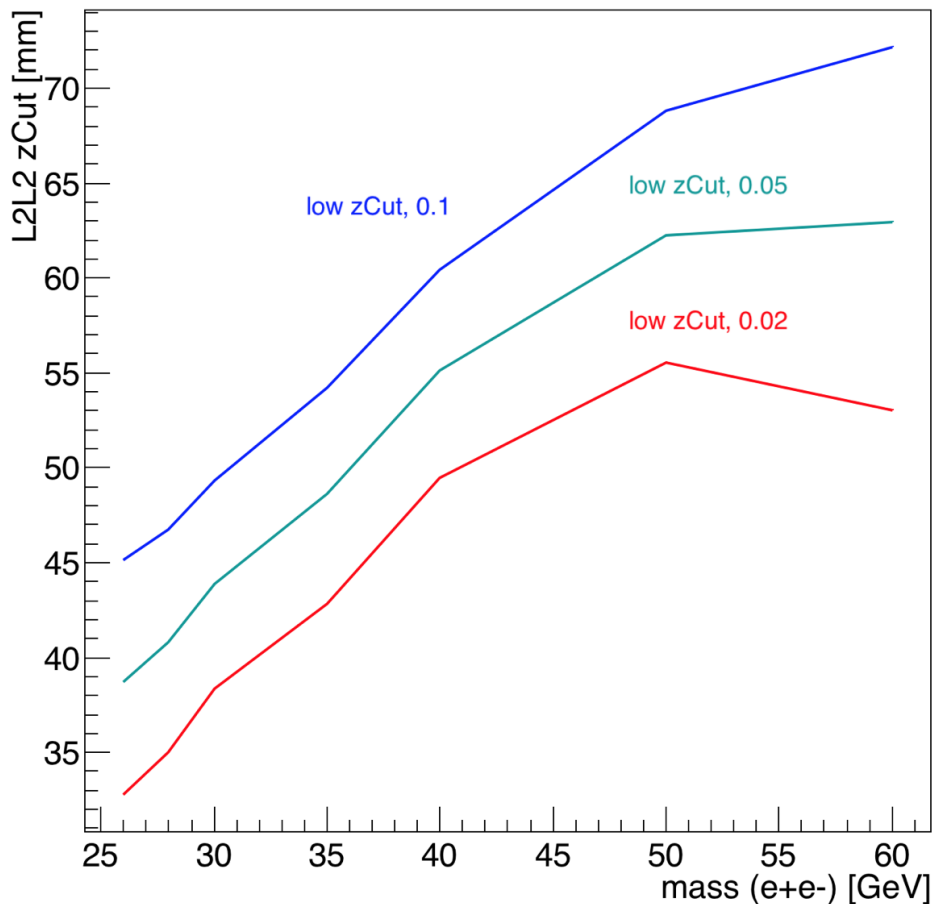


FIG. 6.3.9: .

After all cuts are applied, the resultant z vertex distribution as a function of mass is shown in Figure 6.4.10.

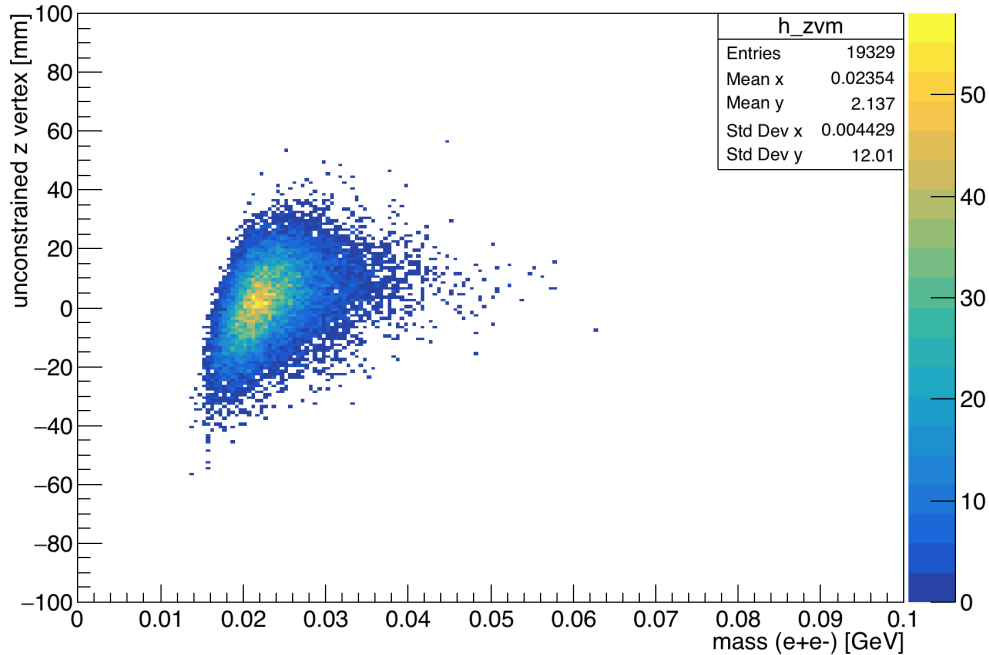


FIG. 6.3.10: Reconstructed z vertex as a function of mass for the L1L1 dataset with the first layer of the SVT at 1.5 mm from the beam. The solid red line indicates the zCut found for 10% of the data (unblinded), and the dashed red line indicates the limit at which events have a quantile greater than 0.5 with respect to the predicted background model. The purple line shows where the projected zCut will be for the full dataset after unblinding.

Assuming that we can remove some of the higher z background events and obtain a reasonable zCut that may optimize the signal yield, we can estimate the upper limit contribution of the L2L2 1.5 mm dataset as shown in the following Figure 6.4.11.

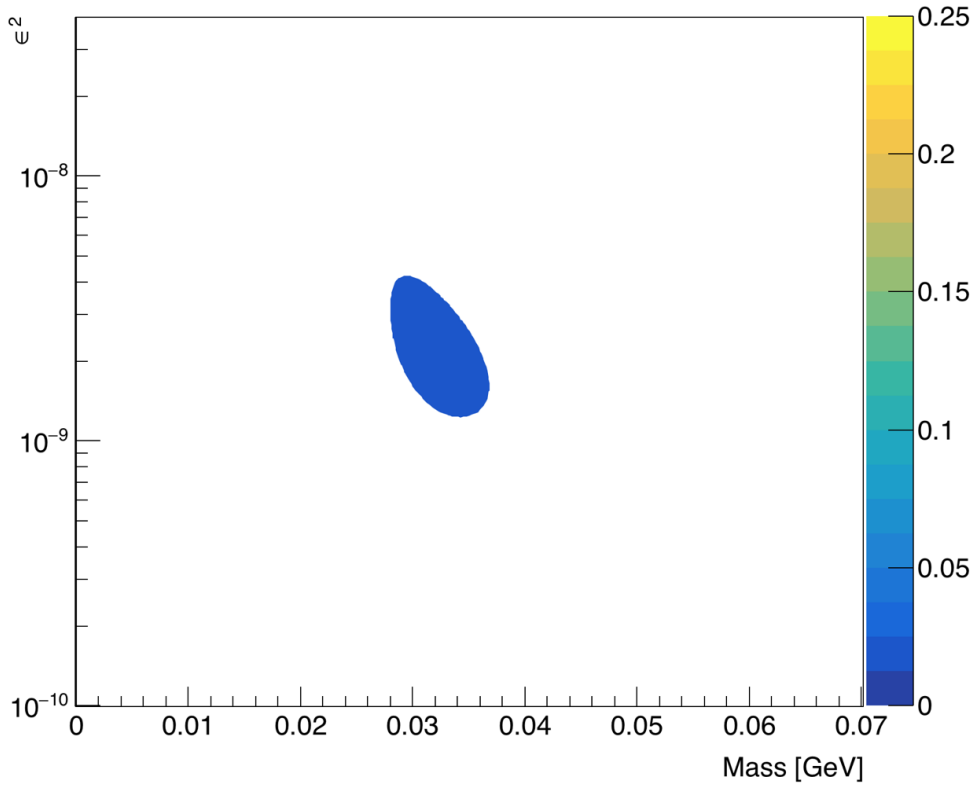


FIG. 6.3.11: The expected signal yield for the full 100% dataset with the L2L2 1.5 mm data.

This upper limit assumes that we can obtain the mass resolution as found in the L1L2 dataset. If we are able to fully characterize the backgrounds of this dataset, optimize the zCut, and improve the mass resolution, then we can probe smaller couplings of the HPS reach parameter space.

6.4 COMBINED REACH PROJECTIONS

The total reach of all 0.5 mm data only is shown in Figure 6.5.1.

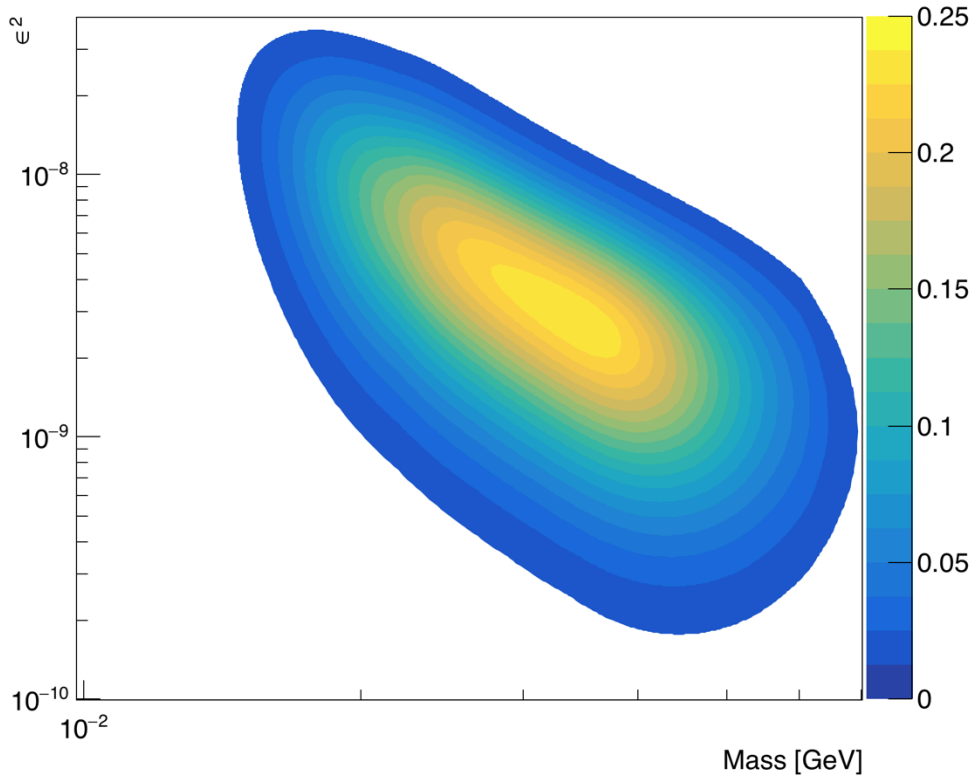


FIG. 6.4.1: The expected signal yield for the full 100% dataset with all 0.5 mm data.

The reach as shown in Figure 6.5.1 uses the projected zCut for 100% of the data and assumes that we can optimize and use the L2L2 dataset. Using the same assumptions, we can obtain the reach for the 1.5 mm dataset alone in Figure 6.5.2.

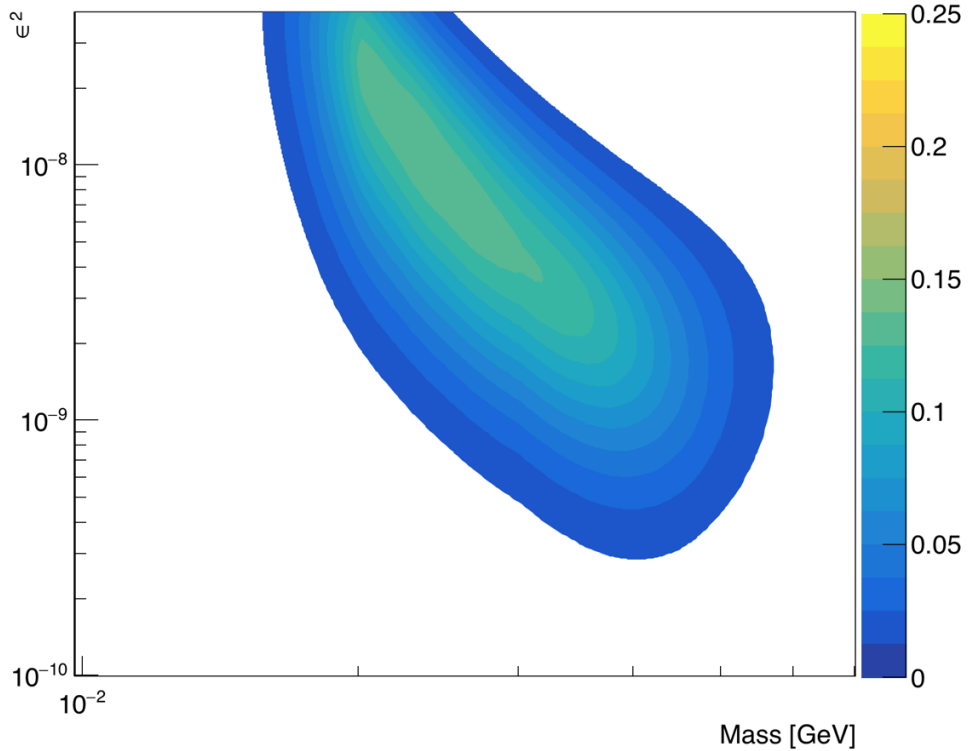


FIG. 6.4.2: The expected signal yield for the full 100% dataset with all 1.5 mm data.

By combining the reach of the 0.5 mm and 1.5 mm datasets, we obtain the full upper limit of the reach we can expect when we unblind the full 2015 data as shown in Figure 6.5.3.

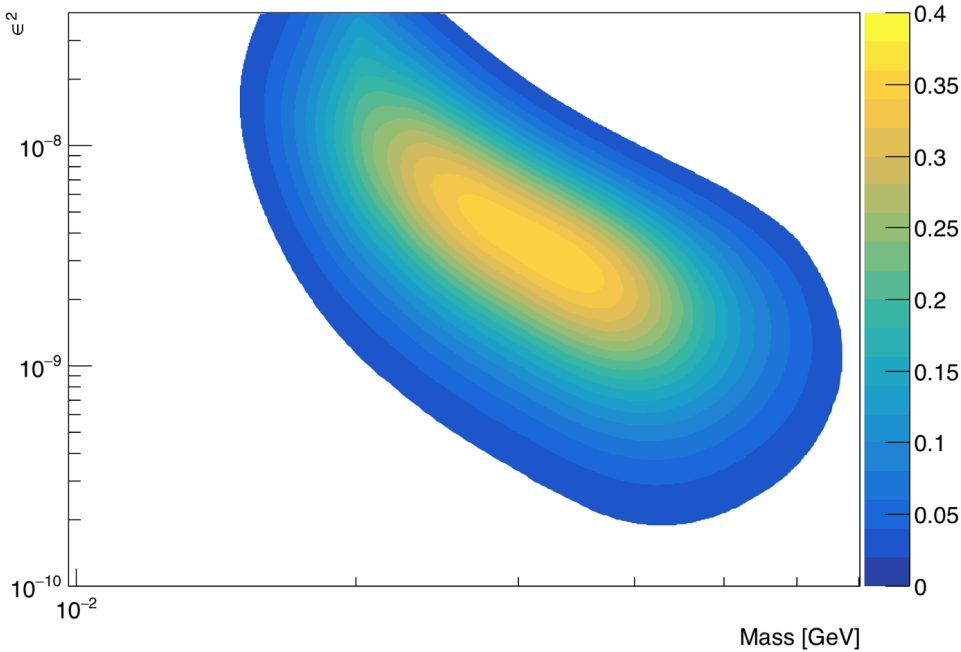


FIG. 6.4.3: The expected signal yield for the full 100% dataset with 0.5 mm and 1.5 mm data combined.

While the statistics of the 0.5 mm dataset drive the reach, the various settings of the SVT and different layer requirements can contribute to the reach by probing the parameter space in different regions of mass and coupling. The maximum signal in Figure 6.5.3 is 0.39 events. In order to have obtained any reach with the data, it would have been necessary to run an additional six times longer than what we did. The contributions from the L2L2 datasets are upper limit estimates that require improved mass resolution and removal of high z backgrounds.

CHAPTER 7

VERTEX SEARCH RESULTS

CHAPTER 8

CONCLUSION

BIBLIOGRAPHY

- [1] G. E. Brown and A. D. Jackson, *The Nucleon–Nucleon Interaction* (North–Holland, Amsterdam, 1976).
- [2] H. Szumila-Vance and M. Garcon, *HPS/ECal simulations: energy and position reconstruction for electrons, positrons and photons*, HPS-Note 2014-001.
- [3] R. Kazimi, *Simultaneous Four-Hall Operation for 12 GeV CEBAF* In Proceedings, 4th International Particle Accelerator Conference (IPAC 2013), page WEPFI085,2013.
- [4] V.A. Batarin et al., *Correlation of beam electron and LED signal losses under irradiation and long-term recovery of lead tungstate crystals* Nucl. Instrum. Meth. A 550 (2005) 543-550.
- [5] A. Celentano et al., *Design and realization of a facility for the characterization of Silicon Avalanche PhotoDiodes*, JINST 9 (2014) T09002, arXiv:1504.01589.
- [6] CLAS12 Collaboration, *CLAS12 Forward Tagger (FT) Technical Design Report*, CLAS12, (2012), <https://www.ge.infn.it/batta/jlab/ft-tdr.2.0.pdf>
- [7] K.A.Olive et al.[Particle Data Group Collaboration], Chin. Phys. C 38, 090001 (2014).
- [8] A. Celentano and G. Charles, HPS-NOTE 2014-002.
- [9] N. Baltzell ECal Pulse Fitting, HPS-NOTE 2015-010.
- [10] PANDA EMC-TDR, October 2008.

APPENDIX A

VITA

Holly Szumila-Vance
Department of Physics
Old Dominion University
Norfolk, VA 23529

The text of the Vita goes here.